A Detailed View of the Circumstellar Environment and Disk
of the Forming O-star AFGL 4176

Katharine G. Johnston,[1] Melvin G. Hoare,[1] Henrik Beuther,[2] Hendrik Linz,[2] Paul Boley,[3,4] Rolf Kuiper,[5] Nathaniel Dylan Kee,[6] and Thomas P. Robitaille[7]

[1]School of Physics & Astronomy, E.C. Stoner Building, The University of Leeds, Leeds, LS2 9JT, UK
[2]Max Planck Institute for Astronomy, Königstuhl 17, D-69117 Heidelberg, Germany
[3]Moscow Institute of Physics and Technology, 9 Institutskiy per., Dolgoprudny 141701, Russia
[4]Ural Federal University, 19 Mira St., Ekaterinburg 620075, Russia
[5]Institute of Astronomy and Astrophysics, Eberhard Karls University Tübingen, Auf der Morgenstelle 10, D-72076 Tübingen, Germany
[6]Institute of Astronomy, KU Leuven, Celestijnenlaan 200D, B-3001 Leuven, Belgium
[7]Aperio Software, Headingley Enterprise and Arts Centre, Bennett Road, Headingley, Leeds, LS6 3HN, UK

ABSTRACT

We present a detailed analysis of the disk and circumstellar environment of the forming O-type star AFGL 4176 mm1, placing results from the Atacama Large Millimeter/submillimeter Array (ALMA) into context with multiwavelength data. With ALMA, we detect seventeen 1.2 mm continuum sources within 5″ (21,000 au) of AFGL 4176 mm1. We find that mm1 has a spectral index of 3.4±0.2 across the ALMA band, with >87% of its 1.2 mm continuum emission from dust. The source mm2, projected 4200 au from mm1, may be a companion or a blueshifted knot in a jet. We also explore the morphological differences between the molecular lines detected with ALMA, finding 203 lines from 25 molecules, which we categorize into several morphological types. Our results show that AFGL 4176 mm1 provides an example of a forming O-star with a large and chemically complex disk, which is mainly traced by nitrogen-bearing molecules. Lines that show strong emission on the blueshifted side of the disk are predominantly oxygen-bearing, which we suggest are tracing a disk accretion shock. The molecules $C^{34}S$, H_2CS and CH_3CCN trace a slow wide-angle wind or dense structures in the outflow cavity walls. With the Australia Telescope Compact Array (ATCA), we detect a compact continuum source (<2000 × 760 au) at 1.2 cm, associated with mm1, of which >96% is from ionized gas. The ATCA NH_3(1,1) and (2,2) emission traces a large-scale (r~0.5 pc) rotating toroid with the disk source mm1 in the blueshifted part of this structure offset to the northwest.

1. INTRODUCTION

Long before they were directly observed, disks were predicted to exist around forming stars of all masses, based simply on the fact that a collapsing cloud of gas will flatten perpendicular to the cloud's axis of rotation due to conservation of angular momentum. However, it was not until the 1980s that disks around young low-mass ($<2\,M_\odot$) stars began to be observed (e.g. Beck-with et al. 1984; Sargent & Beckwith 1987). Led by advances made by the Hubble Space Telescope, which revealed protoplanetary disks in silhouette or scattered light at optical and near-infrared wavelengths (e.g. Mc-Caughrean & O'Dell 1996), many disks around low-mass stars have been observed to-date, and a host of statistical studies of the disk populations in various nearby regions have now been published (e.g. Ansdell et al. 2016, 2018; Tripathi et al. 2017; Andrews et al. 2018). The disks in these surveys, which are typically around unembedded Class II sources, have masses in the range ~0.0001-0.1 $M_\odot$ and radii from 10s to 100s of au.

Corresponding author: Katharine G. Johnston
k.g.johnston@leeds.ac.uk

In comparison, the existence of disks around the young but much more massive B-type stars (equivalent to 8-16 $M_\odot$ zero-age main-sequence stars) was not confirmed until much later (e.g. Cesaroni et al. 2005; Patel et al. 2005). This was caused by observational difficulties due to their relative rarity and thus larger distances, and the fact that massive forming stars are often observed in highly clustered environments, which, combined with a lack of sufficient angular resolution, made the study of these objects challenging. This was followed recently by the first discoveries of disks around O-type stars (Kraus et al. 2010; Jiménez-Serra et al. 2012; Wang et al. 2012; Johnston et al. 2015; Ilee et al. 2016; Cesaroni et al. 2017; Zapata et al. 2019; Sanna et al. 2019). As disks provide a conduit for accretion that has a small solid angle as viewed from the star, they are a particularly essential ingredient in the theory of massive star formation, as they are needed to overcome the large amount of radiation pressure that, in the case of spherical accretion, would impede the accretion of material onto massive stars, and thus halt their formation (e.g. Larson & Starrfield 1971; Kahn 1974; Nakano 1989). Therefore, the recent detection of disks around embedded massive stars confirmed observationally that this was a viable solution to this problem.

Given that there seem to be no unembedded disks around high-mass stars (Williams & Cieza 2011), low-mass embedded Class 0 and I sources are the more likely analogs of observed forming high-mass stars, and are therefore the objects to which we should compare high-mass disk properties. In the case of low-mass Class 0 and I sources, the number of studied objects is also comparatively small, with many studies only observing one object (e.g. Jørgensen et al. 2009, 2016; Enoch et al. 2011; Tobin et al. 2012; Murillo et al. 2013, 2018; Aso et al. 2015; Tobin et al. 2015; Yen et al. 2015; Segura-Cox et al. 2016; Lee et al. 2017; Tobin et al. 2019). These disks are found to have a large range of masses ($\sim$0.001-1 $M_\odot$, e.g. Looney et al. 2003; Enoch et al. 2011; Harsono et al. 2014; Segura-Cox et al. 2016) and disk radii ($<$10 au to 100s of au, e.g. Choi et al. 2010; Murillo et al. 2013; Aso et al. 2015; Yen et al. 2015; Lee et al. 2016). Recent observations of disks around forming high-mass stars have also uncovered a large range of disk properties, including large ($\sim$1000 au, Johnston et al. 2015; Ilee et al. 2016), small (Csengeri et al. 2018; Ginsburg et al. 2018; Girart et al. 2018; Maud et al. 2019) and non-existent disks (Ginsburg et al. 2017; Silva et al. 2017; Beuther et al. 2019).

One explanation for the large range of observed disk properties may lie in the highly clustered environments in which young stars form (Lada & Lada 2003). Interac-

tions between protostars, sometimes in binary or multiple systems, should truncate and shape disks (e.g. Bonnell et al. 2003; Bate 2018). These effects will be more prominent for high-mass stars, which are more likely to form in binary systems (e.g. Sana et al. 2014; Kraus et al. 2017; Koumpia et al. 2019; Zhang et al. 2019a).

Although the study of chemistry in disks around low-mass stars has begun in earnest (e.g. Henning & Semenov 2013; Dutrey et al. 2014), current knowledge about chemistry in disks around massive stars is far more limited, as little has been done on the theory and modeling of their chemistry and only a handful of forming massive stars have resolved observations of several molecules within their disks (e.g., Jiménez-Serra et al. 2012; Ilee et al. 2016, and see Section 6.2 and references within). However, the high densities and temperatures reached in the circumstellar environments of embedded massive stars have led to the detection of many complex molecules toward these objects (i.e. hot core chemistry, Kurtz et al. 2000; van der Tak et al. 2000). It could be that each of the large numbers of complex ($>$6 atoms) but easily detected molecules observed in these sources traces a different part of the circumstellar environment and/or disk, which would prove an extremely useful toolkit in understanding the processes of disk accretion around massive stars. However, we have only begun to scratch the surface in our understanding of this field.

In this work, we present observations of AFGL 4176 (also known as G308.918+0.123 or IRAS 13395-6153), a massive young stellar object (MYSO) with a high luminosity ($\sim 10^5\,L_\odot$, Boley et al. 2012), situated at a distance of 4.2$\pm$0.9 kpc (Green & McClure-Griffiths 2011). Although Bailer-Jones et al. (2018) have recently determined a distance of $3.7^{+2.6}_{-1.6}$ kpc for a star in close projection to AFGL 4176, we note that the previous determination has a smaller error and is consistent within errors with the Bailer-Jones et al. (2018) measurement. Therefore, to be consistent with our previous work, we assume a distance of 4.2 kpc.

The infrared source associated with AFGL 4176 lies at the northern edge of a compact H ii region (Caswell et al. 1992; Ellingsen et al. 2005; Shabala et al. 2006) and is associated with a group of 6.7 GHz Class II methanol masers (Phillips et al. 1998). It has been previously observed at 1.2 mm with the Swedish-ESO Submillimetre Telescope (SEST) by Beltrán et al. (2006), who found a dense core of 0.8 pc and 890 $M_\odot$ at a distance of 4.2 kpc. In addition, we presented initial results from ATCA NH$_3$ observations that indicated AFGL 4176 may be embedded in a large-scale rotating toroid with a radius of $\sim$0.7 pc (Johnston et al. 2014). De Buizer

et al. (2009) detected shocked H_2 emission surrounding AFGL 4176, possibly from knots in an outflow, and Ilee et al. (2013) observed $2.3\mu m$ CO bandhead emission toward AFGL 4176 that could be tracing the inner ~ 10 au of a Keplerian disk. Modeling of the spectral energy distribution (SED) and mid-IR interferometric observations was carried out by Boley et al. (2012, 2013), who found that a combination of a disk-like structure with a radius of 660 au (inclination of 60°, PA=112°), as well as a spherically symmetric Gaussian halo with an FWHM of ~ 600 au, was able to explain the observations.

In a previous study (Johnston et al. 2015, hereafter J15), we presented initial results and modeling of 1.2 mm continuum and line ALMA observations of AFGL 4176. Although there were many lines detected at 1.2 mm, J15 presented only the results for the CH_3CN J=13-12 K transitions, uncovering a near-Keplerian disk with a mass of $12\,M_\odot$ and a radius of 2000 au around an O7 star. In the same paper, we also presented ^{12}CO observations that showed the presence of a large-scale outflow perpendicular to the AFGL 4176 mm1 disk. Using the same ALMA data, Bøgelund et al. (2019) published an analysis of the chemistry in AFGL 4176, with a particular focus on measuring the temperatures, column densities, and abundances of various species, deriving excitation temperatures between 120 - 320 K for the molecules they detected. They found that the column density with respect to methanol is three times higher for O-bearing species than N-bearing species, indicating that AFGL 4176 is likely a young source, with little evidence for significant processing by the central star. They also compared the chemistry of AFGL 4176 mm1 to several other well-studied sources such as Orion KL and Sgr B2, concluding that it was most similar to the low-mass protostar IRAS 16293-2422B, and thus there has not been significant processing of the circumstellar gas by the radiation of the central star.

In this paper, we present a detailed analysis of the circumstellar environment and disk of AFGL 4176, combining continuum and line data from ALMA with complementary ATCA and APEX observations at 1.2-1.5 cm and 1.2 mm, respectively. We have made these data available online[1]. In Section 2, we present the details pertaining to the observations. In Section 3, we present the results from the ALMA data, including details of the millimeter continuum source properties and the characterization and analysis of all of the spectral lines detected in the ALMA data. In Section 4, we present the results from the ATCA observations, including 1.2 cm

[1] http://doi.org/10.5281/zenodo.3369188

continuum and transitions of ammonia. In Section 5 we present results that utilize observations from more than one telescope: APEX and ALMA in the case of $C^{34}S$ J=5-4, and ATCA and ALMA in the case of the hydrogen recombination lines H29α, H64α, H65α H67α and H68α. In Section 6 we discuss our results, including a comparison to other detected disks around O-type young stars, and a short review of how our findings fit within the current knowledge of chemistry in disks around MYSOs. We present our conclusions in Section 7.

2. OBSERVATIONS

2.1. ALMA Observations

The ALMA observations of AFGL 4176 were taken in August 2014 as a Cycle 1 Transfer project during ALMA Cycle 2. The observations are described in J15. Here we mention several further properties of the observations. The cycle time of the phase calibrator was approximately 10 minutes, and the total time on-source across the observations was 1.37 hr. We number each of the four observed spectral windows (spw) by increasing frequency: spw0 to spw3. Table 1 provides further information about each of the observed ALMA spectral windows, including the frequency range covered, the imaged channel width (which is same as the observational spectral resolution), the imaged synthesized beam, and the image rms. The angular resolutions for each spw range from 0.26 to 0.30″, corresponding to 1100 to 1300 au. Each of the four observed spectral windows were imaged using Briggs weighting and a robust parameter of 0.5, and the continuum was subtracted using `imcontsub` in CASA to avoid over-subtraction. The rms noise in each spectral window (given in Table 1) was measured after removal of the line emission, which was performed by σ-clipping each cube. Except for Fig.1, all figures in this paper show primary-beam-corrected images.

When imaging H29α and $C^{34}S$, we instead used natural weighting to recover extended emission, producing beam parameters of 0.33×0.32″ PA=69.0° and 0.35×0.30″ PA=-31.1°, respectively. The H29α image had an rms noise of 1.3 mJy beam^{-1} in a channel width of 2.0 km s^{-1} (larger than the native spectral resolution of 0.33 km s^{-1}), and the $C^{34}S$ had an rms noise of 4 mJy beam^{-1} in a channel width of 1.4 km s^{-1}. The ALMA and APEX $C^{34}S$ images were combined using the CASA task `feather`.

2.2. ATCA Observations

We observed AFGL 4176 with the Australia Telescope Compact Array (ATCA) under project C2646 in the 15-mm band during 2012 on April 17, September 3,

Spw Name	Frequency Range (GHz)	Channel Width (km s^{-1})	Synthesized Beam	RMS Noise (mJy beam^{-1})
spw0	$238.8376 - 239.3064$	0.354	$0.30 \times 0.28''$ PA: $38.0°$	3.8
spw1	$239.6035 - 241.4785$	1.407	$0.29 \times 0.25''$ PA: $-30.8°$	2.0
spw2	$253.1055 - 254.9805$	1.332	$0.28 \times 0.23''$ PA: $-33.7°$	2.1
spw3	$256.1146 - 256.5834$	0.330	$0.26 \times 0.26''$ PA: $-171°$	3.4

Table 1. Summary of observed ALMA spectral windows

and December 21. The observations were designed to target transitions of NH_3 and hydrogen recombination lines. Table 2 presents a summary of the observations, including the start time, length of observation, range of baseline lengths, rms path length measured by the seeing monitor, largest angular scale (LAS), and primary beam for each of the three observing sessions. The pointing center of the observations was $13^h43^m01^s.9$ $-62°08'55.5''$ (J2000). Properties of the observed bands and lines on the three observing dates are given in Table 3. On the first two observing dates, only two continuum bands, with bandwidths of 2.112 GHz and comprising of 33×64 MHz channels, and two zoom bands, with bandwidths of 63.929 MHz and comprising of 2049 $\times$ 31.2 kHz channels, were available. This was expanded to two continuum bands and eight zoom bands on 2012 December 21; all of these zoom bands had a bandwidth of 63.929 GHz and 2049 channels, apart from the 23.709 and 24.509 GHz bands, which had bandwidths of 95.878 MHz and 3073×31.2 kHz channels.

The setup calibrator, which was used to calibrate the delays, pointing, and an initial amplitude and phase calibration, was 0537-441 in all observations, and the primary flux calibrator was 1934-638. The bandpass calibrator was 1253-055, and the phase calibrator was 1352-63, which was observed in a cycle of 1 to 3 minutes with the target source. Calibration and imaging was carried out in the 20120419 ATNF version of MIRIAD. After flagging, the remaining continuum bandwidth was 1.8 GHz for each band in the April and September 2012 datasets, and 1.6 and 1.5 GHz for the 20.905 and 24.205 GHz bands observed on December 2012. Due to poor weather on the final date of observation, we carried out self-calibration on the continuum data and applied these solutions to the line data, which improved the final images. The data were all imaged using a Briggs robust weighting parameter of 0.5. Unfortunately, none of the NH_3 lines observed in December 2012 were detected and therefore will not be discussed further.

2.3. APEX Observations

We observed AFGL 4176 with the Atacama Pathfinder Experiment (APEX)[2] 12 m antenna under program M0007_97 on 2016 April 23 and 26. The precipitable water vapor on these dates was 2.0-2.4 mm and 2.8-3.8 mm, respectively. The pointing center of the observations was $13^h43^m01^s.7$ $-62°08'51.3''$ (J2000). We used the Swedish Heterodyne Facility Instrument (SHeFI) APEX-1 receiver to observe $C^{34}S$(J=5-4) at 241.016 GHz in the lower sideband, which covered frequencies between 240 and 244 GHz with a channel width of 76.3 kHz. The corresponding beam size at this frequency is $25.9''$. On-the-fly maps of $2' \times 2'$ extent were taken in two perpendicular scan directions to reduce scanning artifacts. Pointing calibration was performed every 1 hr, the total observing time was 8.8 hr and the total time on-source was 5.3 hr. Data reduction was performed within GILDAS/CLASS[3]. The achieved rms in the final $C^{34}S$(J=5-4) cube in the central part of the map is 66 mK in a channel width of 0.28 km s^{-1} (three times the native resolution).

3. ALMA RESULTS

3.1. ALMA Millimeter Continuum

3.1.1. Millimeter Continuum Source Properties

In this section, we determine the observed properties of the 1.2 mm continuum sources detected with ALMA, as initially presented in Figure 1 of J15. In J15, only the observed properties of the brightest source mm1 were given; here we present the properties of all of the continuum sources within $5''$ of mm1. We measured the positions and flux densities of these sources using the `astrodendro` software[4]. In this process, we used the non-primary-beam-corrected image and set the peak flux required for a detection to be 5σ, as the noise across this image is constant. The measured properties for these identified sources were then extracted

---

[2] APEX is a collaboration between the Max-Planck-Institut für Radioastronomie, the European Southern Observatory, and the Onsala Space Observatory.

[3] http://www.iram.fr/IRAMFR/GILDAS

[4] http://www.dendrograms.org

Start of Observation (UTC)	Time Observed (hr)	Configuration	Baseline Lengths[a] (m)	Seeing Monitor Path Length rms (μm)	LAS (arcsec)	Primary Beam[b] (arcmin)
2012 Apr 17 08:36:14.9	8.79	1.5B	30.6 - 4301.0	20 - 270	28.1	2.4
2012 Sep 02 22:39:34.9	8.71	6A	627.6 - 5938.8	50 - 250	16.6	2.3
2012 Dec 21 14:09:34.9	11.38	1.5D	107.1 - 4438.8	100 - 950	23.7	2.3

[a] Baseline lengths stated are physical lengths before observation.

[b] Calculated from the highest frequencies and thus provides the smallest primary beam for each observation.

Table 2. Summary of ATCA observations.

Observation Date (UTC)	Central Frequency (GHz)	Continuum or Line(s)	Line Rest Frequency (GHz)	Imaged Chan. Width (km s^{-1})	Restoring Beam	rms Noise (mJy bm^{-1})	Detected?
2012 Apr 17	20.434	Continuum	⋯	⋯	$1.30 \times 1.03''$ PA: 8.9°	0.74	Y (Fig. 16)
	23.712	Continuum	⋯	⋯	$1.20 \times 0.90''$ PA: 7.1°	0.59	Y (Fig. 16)
	20.466	H68α	20.46177	5	$3.63 \times 2.58''$ PA: 12.2° [a]	1.85	Y (Figs. 18, 19, 22)
	23.712	NH$_3$(1,1)	23.69450	0.4	$12.64 \times 11.26''$ PA: 15.4° [b]	6.51	Y (Fig. 18)
	⋯	NH$_3$(2,2)	23.72263	0.4	$12.67 \times 11.19''$ PA: 16.8° [b]	6.34	Y
2012 Sep 2	24.139	Continuum	⋯	⋯	$0.51 \times 0.36''$ PA: 14.4°	0.19	Y (Fig. 17)
	24.533	Continuum	⋯	⋯	$0.51 \times 0.35''$ PA: 14.5°	0.19	Y (Fig. 17)
	24.139	NH$_3$(4,4)	24.13942	0.8	$0.54 \times 0.38''$ PA: 14.8°	1.95	Y (Fig. 20)
	24.533	NH$_3$(5,5)	24.53299	0.4	$0.53 \times 0.37''$ PA: 14.6°	2.38	Y (Fig. 20)
2012 Dec 21	20.905	Continuum	⋯	⋯	$0.96 \times 0.83''$ PA: -88.4°	0.71	Y
	24.205	Continuum	⋯	⋯	$0.87 \times 0.77''$ PA: -88.7°	0.59	Y
	20.457	H68α	20.46177	5	$2.88 \times 2.40''$ PA: -88.6° [a]	2.74	Y
	21.385	H67α	21.38478	5	$2.83 \times 2.37''$ PA: -89.5° [a]	4.42	Y
	23.405	H65α	23.40428	5	$2.84 \times 2.33''$ PA: -87.9° [a]	3.93	Y
	23.709	NH$_3$(1,1)	23.69450	0.8	$7.30 \times 6.99''$ PA: 75.4° [c]	14.25	N
	⋯	NH$_3$(2,2)	23.72263	0.8	$7.25 \times 6.99''$ PA: 74.7° [c]	14.17	N
	23.885	NH$_3$(3,3)	23.87013	0.8	$7.20 \times 7.09''$ PA: 32.7° [c]	14.55	N
	24.141	NH$_3$(4,4)	24.13942	0.8	$0.91 \times 0.84''$ PA: 86.2°	7.08	N
	24.509	NH$_3$(5,5)	24.53299	0.8	$0.90 \times 0.83''$ PA: 87.2°	6.48	N
	⋯	H64α	24.50990	5	$2.86 \times 2.32''$ PA: -87.4° [a]	3.18	Y
	25.069	NH$_3$(6,6)	25.05603	0.8	$0.88 \times 0.81''$ PA: 85.4°	6.30	N

Note—Notes in the final column indicate the figures in which images of the observed band are shown.

[a] A gaussian taper of 2″ was applied to the data during imaging

[b] A gaussian taper of 10″ was applied to the data during imaging

[c] A gaussian taper of 5″ was applied to the data during imaging

Table 3. Summary of observed ATCA Bands

from the primary-beam-corrected image. The flux limit above which flux densities are measured in the primary-beam-corrected image is 2σ in the non-primary-beam-corrected image, and the required flux difference between embedded structures to be assigned as a separate source is 1σ. Table 4 provides the properties of these sources, which include source name, peak position, peak flux S_{peak}, integrated flux S_{int}, mass M, peak column density N_{H_2}, and the geometric mean diameter D, calculated from the area covered by each dendrogram structure. Figure 1 presents the non-primary-beam-corrected ALMA 1.21 mm continuum emission from AFGL 4176 as contours; the sources are labeled with the names given in Table 4, and the area of each source shown in grayscale. We detect 17 sources in the field. The peak and integrated flux densities measured for mm1 are slightly larger than that quoted in J15, which was determined using a Gaussian fit. This is mainly because the Gaussian source lies on a background of more diffuse emission, which was not included in the Gaussian fit, but is included when the source fluxes are determined using `astrodendro`, which assigns groups of pixels to a source. The uncertainties on the flux densities given in Table 4 only give the random uncertainties, whereas an absolute flux calibration error of 10-20% is also expected.

The mass M and peak column density N_{H_2} for each source were determined using,

$$M = \frac{g S_{\mathrm{int}} d^2}{B(\nu, T)\kappa_\nu} \tag{1}$$

and

$$N_{H_2} = \frac{g S_{\mathrm{peak}}}{2.8 m_H \Omega B(\nu, T)\kappa_\nu}, \tag{2}$$

where g is the gas-to-dust ratio, d is the distance, $B(\nu, T)$ is the blackbody function (a function of frequency ν and temperature T), κ_ν is the frequency-dependent opacity, 2.8 is the mean molecular weight, m_H is the mass of a hydrogen atom, and Ω is the ALMA continuum beam area. As in J15, we assume a distance of 4.2 kpc. We assume a gas-to-dust ratio measured for the solar neighbourhood of 154 (Draine 2011) and a temperature of 100 K, except for mm1, where we use a temperature of 190 K, which was the average temperature of the disk derived from modeling CH_3CN line emission using CASSIS[5] (J15). To be consistent with J15, the dust opacity at 1.21 mm was assumed to be $0.24\,\mathrm{cm^2\,g^{-1}}$, which was determined from the Draine (2003a,b) Milky Way dust model with $R_V = 5.5$. This

is a model that fits the dust opacities for the ISM in star forming regions well, and in the rest of this paper, we use this model when referring to ISM dust. In comparison, the Ossenkopf & Henning (1994, hereafter OH94) dust opacity at 1.21 mm for dust with thin ice mantles, subject to grain growth and with densities of $n=10^6\,\mathrm{cm^{-3}}$ is $1\,\mathrm{cm^2\,g^{-1}}$, which if used instead would reduce the masses and column densities by a factor of ~4. We could not use this opacity for the radiative-transfer dust-continuum modeling presented in J15, because the OH94 dust models do not have the associated scattering properties required as input to the radiative-transfer dust code Hyperion (Robitaille 2011). If dust grain growth has occurred in AFGL 4176, then we would expect higher opacities than typical ISM values. The higher densities associated with massive star formation would lead to fast grain growth, but massive stars have short formation timescales (the lifetime of the MYSO phase is $\sim 1-3\times10^5\mathrm{yr}$, Kuiper et al. 2010, 2015, 2016; Davies et al. 2011; Kuiper & Hosokawa 2018). Boley et al. (2013) found evidence for an enhanced population of $1.5\,\mu\mathrm{m}$ grains in AFGL 4176, suggesting grain growth has started, but this would not be enough to change the millimeter opacities significantly.

The sources mm3, mm12, mm13, and mm17 are likely dominated by free-free emission (see Section 4.1); thus, their calculated masses and column densities should be viewed with caution.

We determined the spectral index of mm1 between spw1 and spw2 (between 240.541 and 254.043 GHz) by fitting the continuum data in these spectral windows. We applied the phase self-calibration (i.e. no amplitude self-calibration) derived from the continuum data to the wide spectral windows spw1 and spw2 and selected the channels without line emission to estimate the continuum. Spectral windows spw0 and spw3 were not used, as they contained only a small number of line-free channels. We then found the integrated flux in each line-free channel within a $1''$ diameter aperture around the mm1 peak, and subsequently fitted these continuum channel fluxes by a power law, shown in Fig. 2. The resulting spectral index is 3.36±0.14, where the uncertainty is determined from the scatter in the data. To estimate other sources of uncertainty in our determination of the spectral index, we compared the spectral index derived during our calibration for our phase calibrator J1308-6707 (found to be -0.60 between spw1 and spw2) to that derived from the fluxes in the ALMA Calibrator Source Catalog[6] (-0.48 between 91.5 and 343.5 GHz with both

---

[5] CASSIS is developed by IRAP-UPS/CNRS (http://cassis.irap.omp.eu)

[6] https://almascience.eso.org/sc/

Source name	Peak Position (J2000)	S_{peak} (mJy beam^{-1})	S_{int} (mJy)	Mass[a] ($M_\odot$)	Column Density[a] (cm^{-2})	Diameter (au)
mm1	13:43:01.693 -62:08:51.25	38.49 ± 0.08	61.22 ± 0.04	9.4 [b]	8.3×10^{24} [b]	3500
mm1 branch[c]	13:43:01.693 -62:08:51.25	38.49 ± 0.08	86.21 ± 0.07	13.3 [b]	8.3×10^{24} [b]	6500
mm2	13:43:01.614 -62:08:50.40	6.79 ± 0.08	11.87 ± 0.03	3.6	2.9×10^{24}	2600
mm3[d]	13:43:01.886 -62:08:55.35	2.07 ± 0.08	9.41 ± 0.05	2.8	8.7×10^{23}	4200
mm4	13:43:01.886 -62:08:52.65	2.05 ± 0.08	2.38± 0.03	0.7	8.7×10^{23}	2700
mm5	13:43:01.764 -62:08:53.80	1.54 ± 0.08	9.03 ± 0.05	2.7	6.5×10^{23}	5100
mm6	13:43:01.714 -62:08:50.20	1.30 ± 0.08	1.80 ± 0.02	0.5	5.5×10^{23}	2100
mm7	13:43:02.100 -62:08:52.65	1.21 ± 0.08	9.68 ± 0.06	2.9	5.1×10^{23}	5400
mm7a	13:43:02.100 -62:08:52.65	1.21 ± 0.08	2.76 ± 0.02	0.8	5.1×10^{23}	2200
mm7b	13:43:02.042 -62:08:53.40	1.06 ± 0.08	1.61 ± 0.02	0.5	4.5×10^{23}	1800
mm8	13:43:01.993 -62:08:52.20	0.94 ± 0.08	3.36 ± 0.04	1.0	4.0×10^{23}	3500
mm9	13:43:01.536 -62:08:50.10	0.71 ± 0.08	0.71 ± 0.08	0.2	3.0×10^{23}	1300
mm10	13:43:01.365 -62:08:50.65	0.66 ± 0.08	1.88 ± 0.03	0.6	2.8×10^{23}	2600
mm11	13:43:01.179 -62:08:50.40	0.65 ± 0.08	2.18 ± 0.03	0.7	2.7×10^{23}	2900
mm12[d]	13:43:01.721 -62:08:55.30	0.62 ± 0.08	1.13 ± 0.02	0.3	2.6×10^{23}	2300
mm13[d]	13:43:01.557 -62:08:55.15	0.60 ± 0.08	1.84 ± 0.03	0.6	2.5×10^{23}	3100
mm14	13:43:01.514 -62:08:51.00	0.60 ± 0.08	1.02 ± 0.02	0.3	2.5×10^{23}	1900
mm15	13:43:01.308 -62:08:50.40	0.57 ± 0.08	0.57 ± 0.02	0.2	2.4×10^{23}	1400
mm16	13:43:01.265 -62:08:48.50	0.53 ± 0.08	1.79 ± 0.03	0.5	2.2×10^{23}	3100
mm17[d]	13:43:01.607 -62:08:54.90	0.41 ± 0.08	0.57 ± 0.02	0.2	1.7×10^{23}	1800

[a] The masses and column densities are derived using opacities from Draine (2003a,b). To obtain masses and column densities using opacities from OH94 for dust with thin ice mantles at densities of $n=10^6$ cm^{-3}, the values should be divided by ~ 4.

[b] A temperature of 190 K was assumed, as determined in J15.

[c] mm1 branch includes sources mm1 and mm2.

[d] As discussed in Section 3.1.1, these sources are likely to be dominated by free-free emission from ionized gas.

Table 4. Measured and calculated properties of the ALMA 1.2 mm continuum sources.

frequencies observed on the same date), which provided an estimate of the uncertainty: -0.12. Thus, including the contribution from the scatter in the fit, the combined error in the spectral index is ~ 0.2. To confirm our result, we also imaged the continuum emission in the same wide spectral windows using `clean` and `nterms=2` and obtained a similar average spectral index of 3.35 over pixels within 0.15″ of the continuum peak (where the estimated error in the spectral index in these pixels was <2).

The measured spectral index of 3.4±0.2 can be explained by dust emission, with a contribution of ν^2 from the Rayleigh-Jeans tail of the Planck function (expected at 1.21 mm for dust hotter than 30 K) and the remainder from the frequency dependence of the opacity ν^β. In this case, we would infer $\beta = 1.4 \pm 0.2$. ISM dust has values of $\beta \sim 1.6$ (Draine 2003a,b), which is within 1σ of our measured spectral index. In the following section we assess the contribution to mm1 from free-free emission at 1.21 mm.

3.1.2. *Contribution of Free-free Emission to mm1*

In Section 4.1, we find centimeter continuum emission associated with mm1, which cannot be explained by dust emission alone. Therefore, the millimeter continuum emission from mm1 may also contain free-free emission. The spectral index estimated between 1.21 mm and 1.23 cm is 1.56±0.15 (Section 4.1), which might be explained by almost-optically thick free-free emission with the same spectral index. Assuming a hypercompact HII region with a size of 2000 au is producing the centimeter continuum emission (Section 4.1), and the temperature of the HII region is 10^4 K, the electron density would have to be $\gtrsim 5 \times 10^6$ cm^{-3} to ensure that the turnover frequency was above 24.328 GHz (corresponding to 1.23 cm; Mezger & Henderson 1967). Although high, this would in theory be possible, as the hydrogen
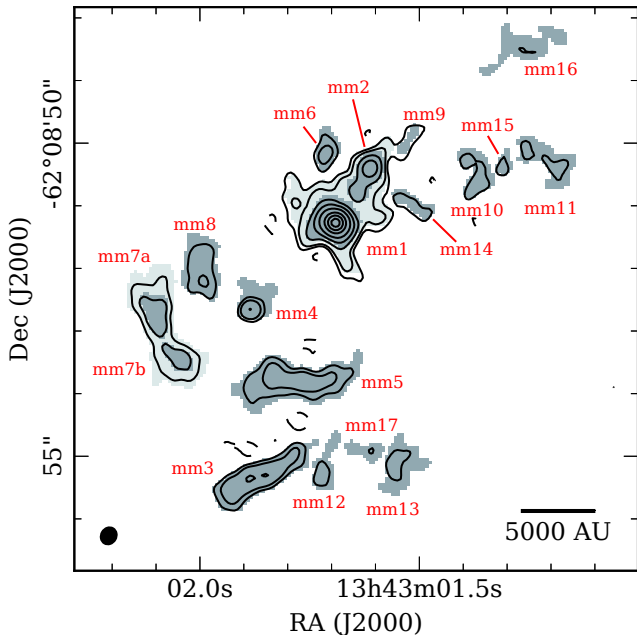
Figure 1. Continuum emission toward AFGL 4176 at 1.21 mm observed with ALMA shown in contours (non-primary-beam corrected, $\sigma = 78\mu\mathrm{Jy\,beam^{-1}} \times$ -5, 5, 10, 25, 50, 100, 200, 300, 400). The area of each detected ALMA 1.21 mm source is shown in dark gray, as well as combined sources mm1 branch (containing mm1 and mm2) and mm7 in light gray (see Section 3.1.1 for details). The 1.21 mm sources, which are listed in Table 4, are labeled in red. The synthesized beam, with size $0.28 \times 0.24''$, PA = -30.2°, is shown in the bottom left corner.

molecular number density derived from molecular line fitting is $> 8 \times 10^7 \, \mathrm{cm^{-3}}$ (J15), which is larger than this value. However, the spectral index at 1.21 mm is 3.4±0.2, indicating dust emission is present, and the morphology and extent of the emission at the two wavelengths is dissimilar, implying that the emission at each wavelength is not tracing the same material. Therefore, it is likely that both ionized gas and dust emission contribute to the continuum emission at both wavelengths, but that dust emission dominates at 1.21 mm and ionized gas at 1.23 cm.

We now derive the fraction of ALMA continuum emission due to dust. When combining the contribution from dust and ionized gas, the total flux density F_ν at a given frequency ν within the ALMA spws is given by

$$F_\nu = F_{\nu_0} \left[f\left(\frac{\nu}{\nu_0}\right)^{\alpha_d} + (1-f)\left(\frac{\nu}{\nu_0}\right)^{\alpha_{\mathrm{ff}}} \right], \quad (3)$$

where F_{ν_0} is the total flux density at ν_0, f is the fraction of ALMA continuum emission due to dust at ν_0, and α_d and α_{ff} are the spectral indices of the dust and ionized gas emission, respectively.

Starting from Equation (3), the spectral index can be expressed as

$$\alpha_{\mathrm{obs}} = \frac{d\log_{10} F_\nu}{d\log_{10}\nu} \quad (4)$$

$$= \frac{F_{\nu_0}}{F_\nu}\left[f\alpha_d\left(\frac{\nu}{\nu_0}\right)^{\alpha_d} + (1-f)\alpha_{\mathrm{ff}}\left(\frac{\nu}{\nu_0}\right)^{\alpha_{\mathrm{ff}}}\right] \quad (5)$$

As the ALMA spws cover a small range of frequencies, we assume that the observed spectral index α_{obs} across these spws is constant. Therefore, by evaluating α_{obs} at ν_0, we find

$$\alpha_{\mathrm{obs}} = f\alpha_d + (1-f)\alpha_{\mathrm{ff}}. \quad (6)$$

and thus,

$$f = \frac{\alpha_{\mathrm{obs}} - \alpha_{\mathrm{ff}}}{\alpha_d - \alpha_{\mathrm{ff}}}. \quad (7)$$

Assuming an upper limit for the spectral index of dust emission of 3.6 (derived from the dust model used in J15), an observed (i.e. combined) spectral index α_{obs} of 3.4±0.2, and an upper limit to the ionized gas spectral index at 1.21 mm of 2, we find a lower limit to the dust emission fraction f of 87±13%. Thus, dust emission dominates at 1.21 mm, even in the case of the largest possible contribution from free-free emission.

As we do not know the exact contribution to the emission from ionized gas at 1.21 mm, and because the relative astrometry is not sufficiently accurate and the lower resolution of the ATCA data precludes our knowledge of the morphology of the 1.23 cm emission, we do not attempt to remove the free-free contribution from the ALMA continuum data. However, we have determined it only contributes <13% and thus the majority of the emission arises from dust.

3.1.3. *Comparison to Maser Positions*

Figure 3 shows the positions of several maser species detected toward AFGL 4176, including four Class II methanol masers from Phillips et al. (1998), the position of ground-state OH masers at 1665 and 1667 MHz detected by Caswell (1998), and four water masers detected by Walsh et al. (2014). Although the spatially linear methanol maser group (red circles) appears to not be coincident with the continuum peak of mm1, the absolute positional uncertainty of the ALMA data (orange circle, ~0.1″ or ~1/3 × the beamwidth) would nearly allow the methanol maser group to be coincident with the peak of mm1. However, in Section 3.2.4 we show that the thermal CH₃OH emission is also offset to the east of the millimeter continuum peak of mm1, so that the maser emission is probably occurring in the areas of brightest thermal CH₃OH emission. The OH maser (cyan square) is coincident with an extension of
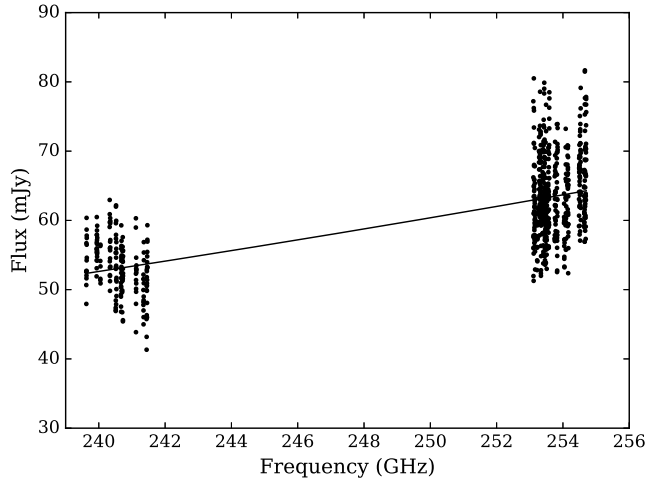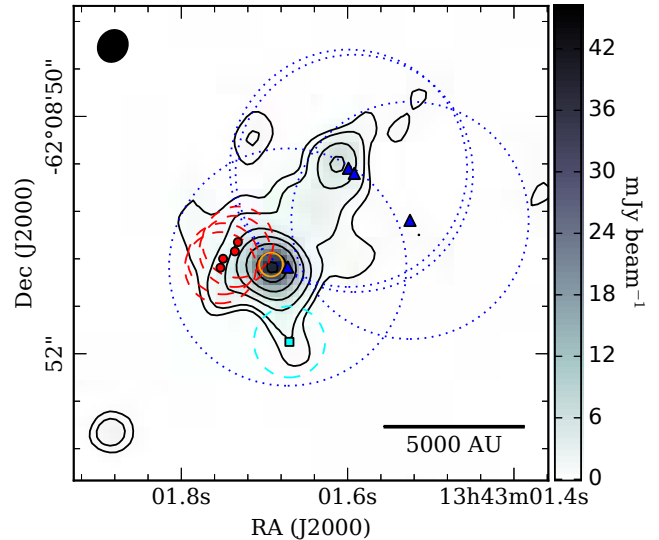
Figure 2. Spectrum of mm1 constructed from the continuum-only channels in the ALMA wide spws (spw1 and spw2). Each channel is shown as a black point. The black solid line shows the best-fitting spectral index of 3.36±0.14.

Figure 3. Continuum emission toward AFGL 4176 at 1.21 mm observed with ALMA shown in grayscale and contours (local $\sigma = 0.12 \, \mathrm{mJy \, beam^{-1}} \times$ -3, 3, 5, 10, 25, 50, 100, 200, 300, 400) with maser positions and their error circles overplotted. The red circles show Class II methanol masers from Phillips et al. (1998), the cyan square shows the position of the main line ground-state OH masers detected by Caswell (1998), and the blue triangles show the positions of water masers detected by Walsh et al. (2014). The colored dashed or dotted circles represent the absolute positional uncertainties on the maser positions. The ALMA beam is shown in the top left corner. The positional uncertainty of the ALMA data is shown as an orange circle at the continuum peak position.

5σ emission to the southwest of mm1. There are similar but less-prominent extensions to the northwest and southeast. Given the orientation of the disk as determined by J15, OH masers could potentially be tracing the outflow cavity walls, which is similar to that seen in G35.20-0.74 (De Buizer 2006). Finally, although the positions of the water masers (blue triangles) are stated to be less accurate than the other masers shown, there is one maser slightly offset to the west of mm1, and another two masers that are similarly offset from mm2. This near-coincidence and similar offset from the two brightest millimeter continuum sources in the field may indicate that the water masers are in fact coincident with these two millimeter continuum sources.

3.1.4. *Comparison to Mid-IR observations*

It is also illuminating to compare previous estimates of the source orientation via mid-IR observations. Using spectropolarimetry of the silicate absorption feature in AFGL 4176, Smith et al. (2000) found a polarization position angle (PA) of 55±1°. Interestingly, this compares well to the disk PA determined from our 1.2 mm ALMA continuum observations (59±17°, J15). In comparison, Boley et al. (2012, 2013) determined the PA of the mid-IR emission using MIDI observations at 10.6 μm, finding a value of 112°. However, as discussed in J15, this difference may be because the MIDI observations trace the heated dust in the outflow cavity instead of the disk emission itself (e.g., for W33A, de Wit et al. 2010).

3.2. *ALMA Line Emission*

In this Section, we present the spectra and detected lines toward AFGL 4176, and we investigate the various categories of spectral and spatial morphology seen across the detected species.

3.2.1. *Spectra and Detected Lines*

In this Section, our aim is to provide a complete census of the lines present in the spectra from AFGL 4176 mm1. We do not aim to determine the physical properties associated with each species from fitting all lines with a global physical and chemical model, but instead concentrate on using this as a method to identify the lines detected in the spectra. As our aim is to obtain a census of the lines present across the entire area in which AFGL 4176 mm1 is emitting, and not only at one point in the maps, we produced mean spectra averaged over a circular aperture of $0.5''$ in radius centered at the peak position of the continuum emission: $13^h43^m01^s.693 \; -62°08'51.25''$ (FK5 J2000). Figures 4 and 5 display the spectra for the narrow and wide spec-

Group Designation	Molecules
O-bearing	$HCOOH$, CH_2CO, CH_3OH, CH_3CHO, CH_3OCHO, $HCOCH_2OH$, C_2H_5OH
	CH_3OCH_3, CH_3COCH_3, aGg'-$(CH_2OH)_2$ [a]
N-bearing	HC_3N, H_2CCN, NH_2CN, CH_3CN, C_2H_3CN, C_2H_5CN, NS, HNCO, $HC(O)NH_2$
S-bearing	$C^{34}S$, H_2CS, SO, SO_2, OCS
Other	CH_3CCH

[a] aGg' conformer of ethylene glycol

Table 5. List of Molecules Detected Toward AFGL 4176 mm1 with ALMA

tral windows, respectively. The 0.5″ aperture also allows us to determine the bulk properties of the gas associated with AFGL 4176 mm1 averaged over all of its emission, which we will analyze in Section 3.2.2.

The line identification was carried out as follows. The noise was measured in an empty section of each spectrum and was found to be 0.968, 0.307, 0.410, and 0.703 mJy beam^{-1}, respectively, for spw0-3. All lines that have a peak flux larger than 5σ were identified in the spectra.

Using the spectral analysis package CASSIS,[7] we first fit an LTE model to the CH_3OH and $^{13}CH_3OH$ lines in spw2 to determine an approximate set of physical parameters that we could expect for each detected line. To do this, we started from the parameters at the position of the peak continuum emission found from the CH_3CN CASSIS line fitting in J15 (N_{H_2} = 2.8×10^{24} cm^{-2}, v_{LSR}=-53 km s^{-1}, Δv_{FWHM}=8.4 km s^{-1}, T=290 K, and a size of 0.5″), and interactively adjusted the parameters to obtain a good fit by eye. CH_3OH was used because it had a large number of lines that were clearly detected in the spectra; other lines and molecules were not usable until they were correctly identified. We note that the fitted parameter values were not required to be exact for fitting other lines, as they were only used as initial estimates that were then varied for each molecule.

The values that provided a reasonable fit to the data were N_{H_2} = 4×10^{25} cm^{-2}, v_{LSR}=-52 km s^{-1}, Δv_{FWHM}=5 km s^{-1}, T=160 K, and a size of 0.5″. We assumed an abundance relative to hydrogen of 10^{-8} for CH_3OH (found for Hot Molecular Cores, Gerner et al. 2014) and find that an isotopic ratio of ∼20 is required to simultaneously fit the $^{13}CH_3OH$ lines. We note that the column density of $N_{H_2} = 4\times10^{25}$ cm^{-2} is slightly higher than that found for mm1 in Table 4 (8.3×10^{24} cm^{-2}), but given the uncertainty in abundance, this value is in reasonable agreement. In addition, we find later in the paper (Section 3.2.7) that several of the CH_3OH lines are optically thick, which would indicate that the iso-

topic ratio is higher and therefore the overall density of CH_3OH is also higher.

For each detected line, we used the Cologne Database for Molecular Spectroscopy (CDMS,[8] Müller et al. 2005) and Jet Propulsion Laboratory (JPL,[9] Pickett et al. 1998) line databases to determine a list of transitions that could explain the line. We then manually interactively adjusted the abundance (keeping the column density of molecular hydrogen fixed), excitation temperature, velocity, and linewidth for each possible species, using the fitted parameters for CH_3OH as initial estimates, to gauge whether a given species was responsible for emitting a specific spectral line. If the spectrum predicted by CASSIS produced bright lines that were not in the spectrum, we discarded this identification. If the species in question produced other lines present in the spectrum with the correct relative brightnesses, this increased the likelihood that this was the correct identification. CASSIS produced a spectrum that included the effects of blending; thus, as line identifications were added, the resultant combined spectrum could be checked for agreement with the observed one.

Once the line identification was complete, all line properties were determined via a simultaneous spectral fit with Gaussians to all of the detected lines using `astropy.modeling` with the Sequential Least Squares Programming (SLSQP) fitter, leaving flux density, velocity, and linewidth as free parameters. As input to this algorithm, an estimate for the central frequency of each line was first determined from a separate fit by hand to each line in CASSIS (i.e., specifying the frequency range in which to conduct an automated Gaussian fit for the line), which was fed to the SLSQL fitter, along with the measured flux at this frequency as an estimate for the line amplitude, and twice the channel width as an estimate for the linewidth. The peak flux was allowed to vary within 0.7-1.5 times the estimated peak flux; the central frequency was allowed to range between

---

[7] CASSIS is developed by IRAP-UPS/CNRS (http://cassis.irap.omp.eu)

[8] https://cdms.astro.uni-koeln.de/classic/entries/]

[9] https://spec.jpl.nasa.gov/ftp/pub/catalog/catdir.html

±4 and ±1 times the channel width for the narrow and wide spws, respectively; and the linewidth was allowed to vary within $3 - 10$ and $1 - 4$ times the channel width for the narrow and wide spws, respectively. In busy portions of the wide spectral windows (spws 1 and 2), we fit the lines by hand with a set of Gaussians in CASSIS and included their fixed properties in the global fit. This was necessary because the automated fitting did not work well in these portions of the spectra. As we conducted a simultaneous fit of the observed lines, the properties of any blended lines were appropriately determined. The combined fit of all the best-fitting Gaussians for each line is shown overplotted on the observed spectra in Figs A.1 and A.2. A list of identified lines and their measured properties, including their fitted fluxes, velocities, and linewidths, is given in the Appendix in Tables A.1-A.4. The line databases used for each species are given in Table A.5. The molecular tags given in Table A.5 provide, for each species, the unique identifier used to identify it within each database.

Not including isotopologues, we detect a total of 25 different molecules, which are listed in Table 5, from a total of 203 lines, summarized in Table A.5. The line identifications are generally in good agreement with Bøgelund et al. (2019), who find 23 molecules in their spectra from a total of 354 lines. In addition to the 23 molecules detected by Bøgelund et al. (2019), we also find lines of H_2CCN and NH_2CN, bringing our total to 25, which is likely due to the larger aperture used to obtain our spectra. We did not find sufficient evidence to confirm the detection of gGg' ethylene glycol. We detect seven lines that we cannot identify (marked with a ? in Tables A.1-A.4), which are also not identified in Bøgelund et al. (2019). We suspect that the fact Bøgelund et al. (2019) detect 354 lines in their spectra whereas we only detect 203 is mainly due to their lower detection threshold (3σ). For instance, 228 lines are labeled in their Figs. 2, C.1, C.2, and C.3 (likely to be the brightest unblended ones in their Figures), similar to the number we detect. There are two other potential explanations for the discrepancy in the number of detected lines. The first is that we define a line as a detected peak in the observed spectra, and thus in the case of blending associate several possible identifications with one detected line. However, in Bøgelund et al. (2019), each contribution to the blended observed line constitutes one line, thus resulting in more lines detected. Second, there may be some lines that have morphologically compact emission. In this case, obtaining an average spectrum within a $0.5''$ radius aperture would wash these out, thus removing them from our measured average spectra in comparison to the Bøgelund et al. (2019) spectra, which were measured at the continuum peak position.

3.2.2. *Line morphological categories*

By inspecting the channel maps for each line, we found that the lines could be grouped into several morphological types, which will be reviewed in detail in the following sections. These types are as follows: disk-tracing, blue-dominant, red-dominant, and outflow-tracing lines. There is also a fifth category labeled as "unknown", which covers lines that did not clearly fit into one of the above categories, often because the emission from these lines did not have a high signal-to-noise. Tables A.1-A.4 list the morphological group for each detected line; Table A.5 summarizes the number of identified lines for each morphological type for each species.

In Figure 6 we compare the emission from the 10 brightest lines (eight for the red-dominant lines) that had a unique identification and had no other detected line within $10\,\mathrm{MHz}$ ($\sim 12\,\mathrm{km\,s^{-1}}$) for the three morphologies with compact emission: blue-dominant, disk-tracing, and red-dominant. Figure 6 visually shows the difference between these morphology groupings. The blue-dominant lines show a prominent bar of emission to the east of the peak of mm1 in the blueshifted and sometimes central channels. They also have fainter emission in the redshifted channel. The disk-tracing lines are more kinematically symmetric, showing a velocity gradient progressing from east to west. We will show in Section 3.2.3 that these are morphologically and kinematically similar to the upper K-ladder transitions of CH_3CN and therefore trace the disk. The red-dominant lines are more similar to the disk-tracing lines, but are generally more extended in the redshifted channel, with most possessing an arc of emission reaching up to the northwest.

To quantitatively determine the similarity and differences within and between the compact morphology groups, we calculated average reduced χ^2 values between the different lines. For each pair of lines, we calculated a χ^2 value using three channels at -2, 0, and $+2\,\mathrm{km\,s^{-1}}$ from the v_{LSR} ($-52\,\mathrm{km\,s^{-1}}$), considering pixels in a $2 \times 2''$ field of view centered on the peak continuum position of mm1, as shown in Fig. 6. To make the comparison uniform, we added noise to each of the three channels, so that all channels had a peak signal-to-noise of 15. We also only considered lines with a peak signal-to-noise that was above 15 in all three channels before adding noise. The reduced χ^2 was calculated by comparing these three channel maps separately to the channel maps of another line at the same velocities, and
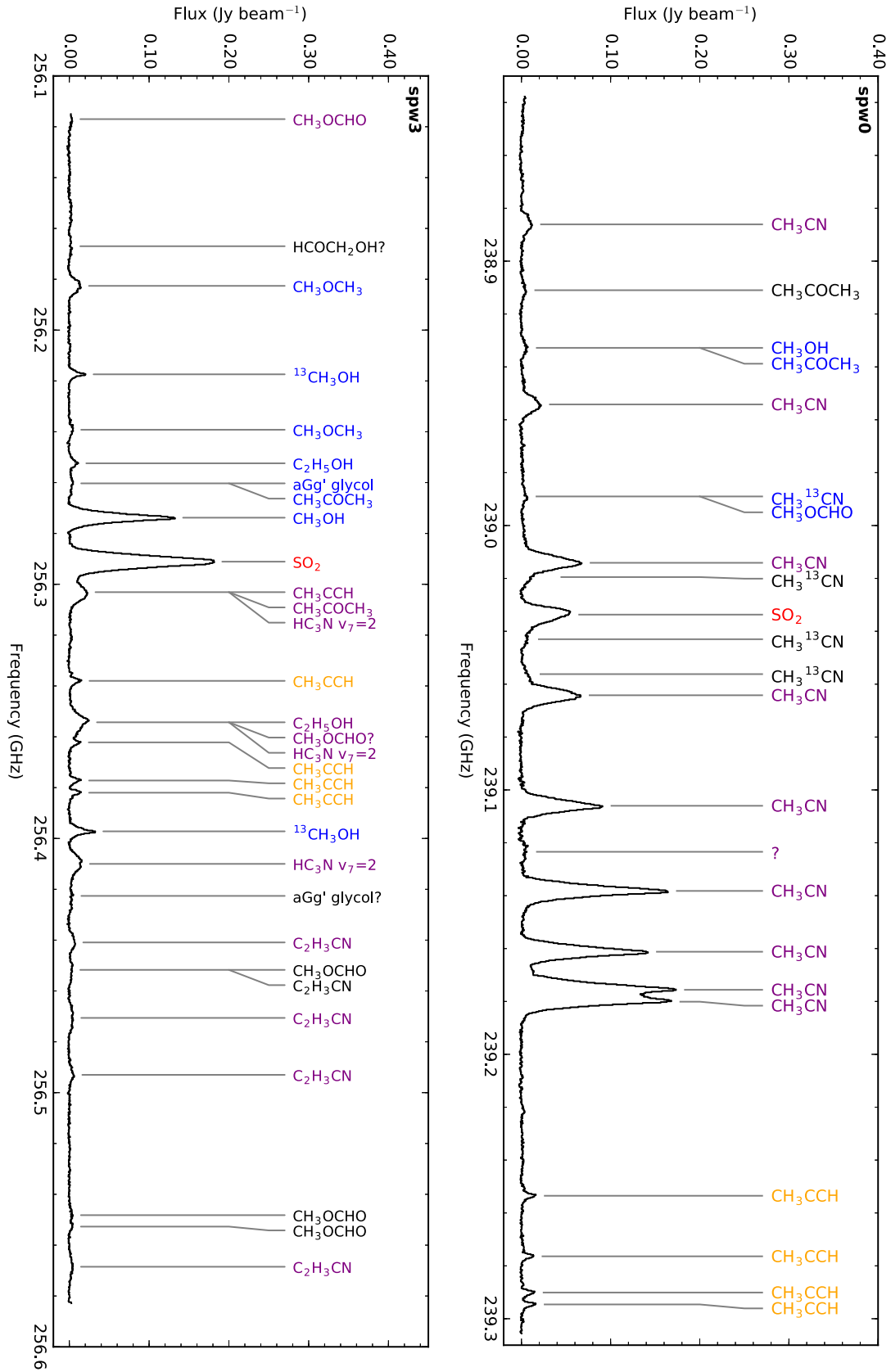
Figure 4. Spectrum of the two ALMA narrow spectral windows covering 238.8376 – 239.3064 and 256.1146 – 256.5834 GHz. The different line label colors denote different types of line morphology: purple is disk-tracing, blue is blue-dominant, red is red-dominant, and orange is outflow-tracing. Line labels are black when no classification was possible.
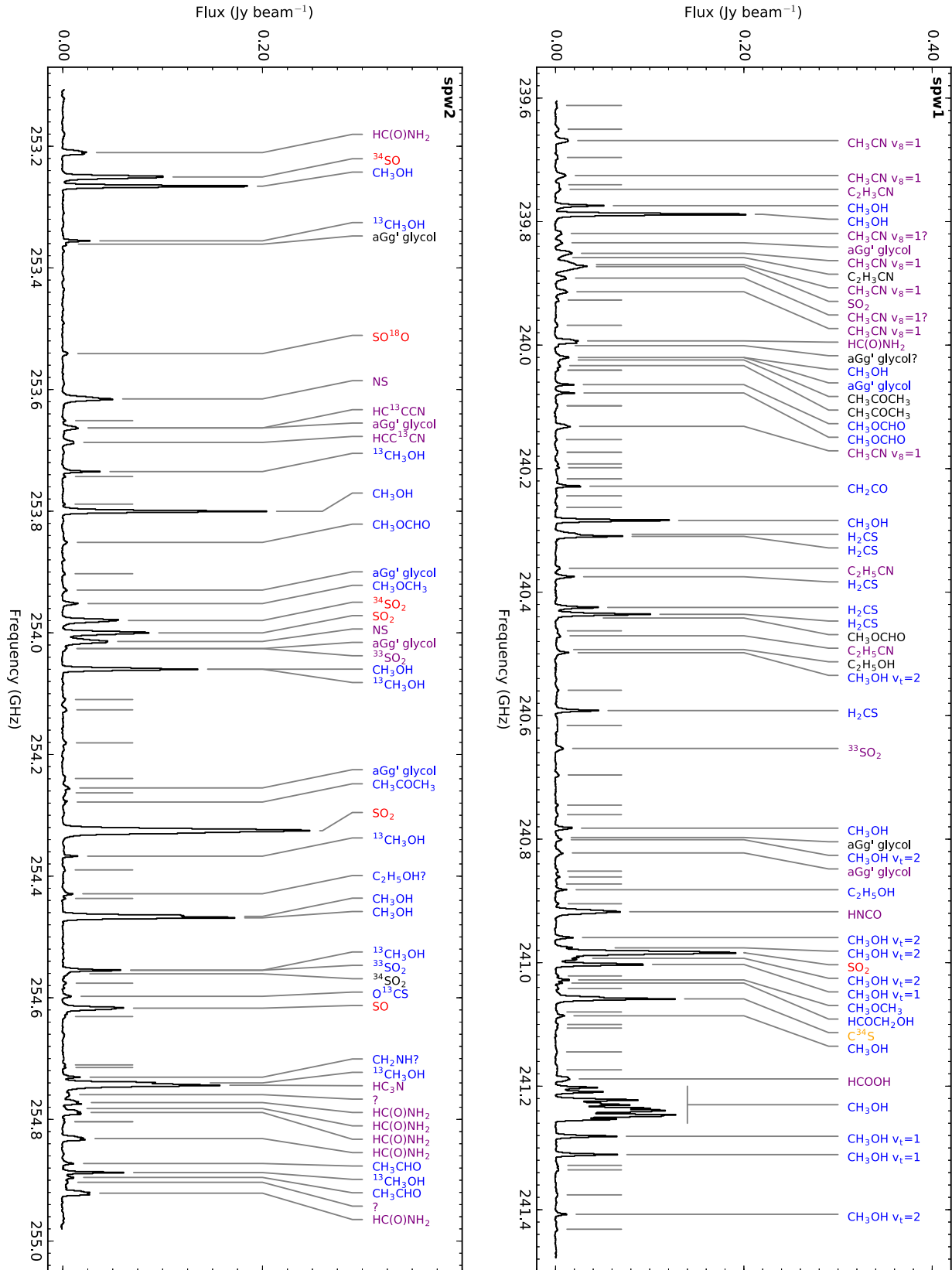
Figure 5. Spectrum of the two ALMA wide spectral windows covering 239.6035 – 241.4785 and 253.1055 – 254.9805 GHz. The different line label colors denote different types of line morphology: purple is disk-tracing, blue is blue-dominant, red is red-dominant, and orange is outflow-tracing. Line labels are black when no classification was possible.

Blue-dominant lines   Disk-tracing lines   Red-dominant lines
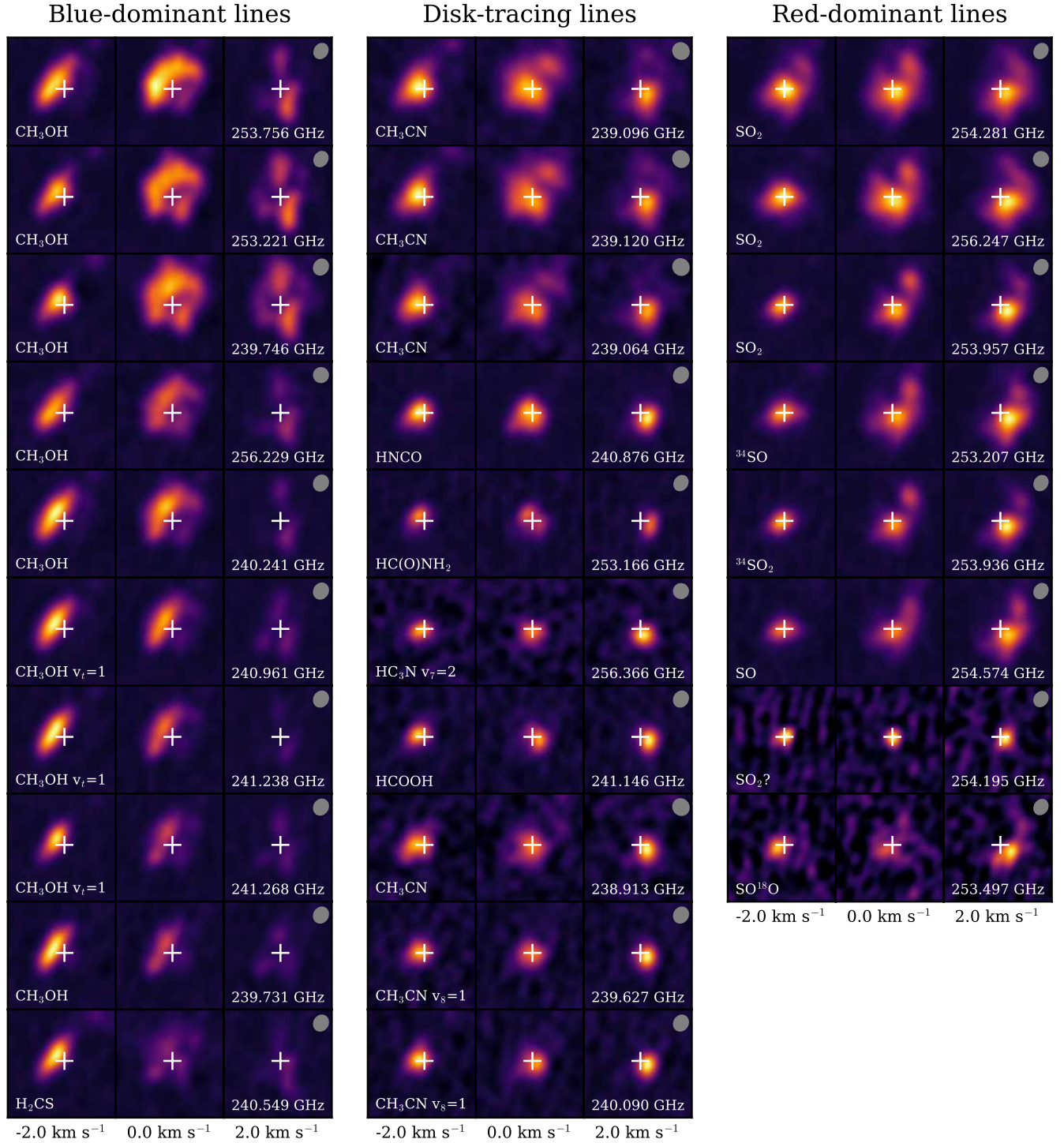
Figure 6. Comparison of the channel maps at -2, 0, and $2\,\mathrm{km\,s^{-1}}$ of the line center, $\mathrm{v}_{LSR} = -52\,\mathrm{km\,s^{-1}}$, for the 10 brightest blue-dominant, disk-tracing, and red-dominant lines (eight for red-dominant). Each panel is a $2''$ ($8400\,\mathrm{au}$ at $4.2\,\mathrm{kpc}$) square centered on $13^h43^m01^s\!.71\ -62°08'51.35''$ (J2000). The peak position of the 1.2 mm continuum (mm1) is shown as a white plus sign in each panel. The molecule and rest frequency for each line are shown in the bottom corners of the left and right panels, respectively. The beam is shown in the top right of the right panel for each line. The emission for each line has been normalized to the line map peak flux density.

	B	D	R
B	1.78±0.05	3.33±0.08	3.55±0.07
D	3.33±0.08	1.63±0.05	2.14±0.05
R	3.55±0.07	2.14±0.05	1.35±0.05

Table 6. Average reduced χ^2 values for comparison between the three compact morphological types. B stands for blue-dominant, D for disk-tracing, and R for red-dominant.

an average χ^2 for a pair of lines was then determined by combining the χ^2 over these three velocity channels.

With a reduced χ^2 for each pair of lines in hand, we computed an overall average reduced χ^2 (with associated error in the mean) between morphological types, including comparing each line morphological type with itself. The results presented in Table 6 show that the reduced χ^2 values when comparing the line morphologies with themselves are close to one, indicating similarity, as expected (if the images were identical, modulo noise, this would produce a reduced χ^2 of $\sim$1), but that the average reduced χ^2 is statistically significantly higher when the χ^2 is calculated from comparison between line types, thus showing that the morphology groups are quantitatively different from one another.

As the emission from the outflow-tracing lines is more extended and clearly different to the first three morphological types, we show these in Figure 7, which has a larger field of view of $4''$. The outflow-tracing lines are similar in that they all have secondary extended emission near the position of mm2, not seen in the other lines, which is most prominent in the $-2\,\mathrm{km\,s^{-1}}$ channel. This emission extends away from mm1 in a direction perpendicular to the disk midplane in mm1.

In terms of chemistry, the 10 O-bearing molecules we detect have a mixture of morphologies, but for the most part have predominantly blue-dominant morphologies. In addition, we detect nine N-bearing molecules, all of which morphologically trace the disk (i.e. are disk-tracing lines), except H_2CCN, whose lines are too faint to determine a morphology. Lastly, there are five S-bearing molecules and one further molecule (CH_3CCH) detected, which have a mixture of morphologies.

Figure 8 displays the variation of the fitted peak velocity of the detected molecules as a function of the upper transitional level energy (left panel) and linewidth (middle panel), as well as their fitted upper transitional level energy as a function of linewidth (right panel). All molecules with a detection $>20\,\sigma$ are shown. The different line morphological types (disk-tracing, blue-dominant, red-dominant, and outflow-tracing) are shown as points of different colors with error bars. Since the fitting algorithm used for the simultaneous fit with

Outflow-tracing lines
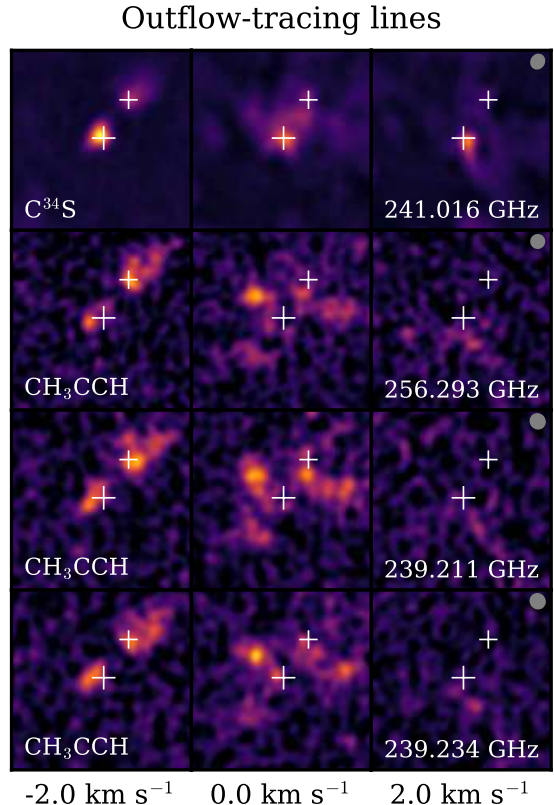
Figure 7. Comparison of the channel maps at -2, 0, and $2\,\mathrm{km\,s^{-1}}$ of the line center, $v_{LSR} = -52\,\mathrm{km\,s^{-1}}$, for the brightest outflow-tracing lines with unambiguous identifications and without any lines detected within 10 MHz ($\sim$12 km s^{-1}). Each panel is $4''$ (16800 au at 4.2 kpc) square and centered on $13^h43^m01^s.71\ -62°08'51.35''$ (J2000). The peak positions of the 1.2 mm continuum for mm1 and mm2 are shown as white plus signs. The molecule and rest frequency for each line is shown in the bottom corner of the left and right panels, respectively. The beam is shown in the top right of the right panel for each line. The emission for each line has been normalized to the line map peak flux density.

hundreds of free parameters did not provide errors for the fitted parameters, the errors were instead estimated by testing the fitting algorithm used with Monte Carlo simulations of synthetic data to determine the relationship between the error in the velocity and linewidth of each line to the signal-to-noise and linewidth of that line. The error bars are for the most part smaller than the data points.

Each line type displays velocities or linewidths scattered around different values. A dashed line showing the mean velocity and linewidth for each line type is shown in each panel (ambiguously identified or possibly blended lines are shown as empty points). The mean velocities for the solid points for each

line type are -51.64±0.21, -52.44±0.15, -52.88±0.11, and -53.27±0.10 km s^{-1} for red-dominant, disk-tracing, outflow-tracing, and blue-dominant lines, respectively. The left and right panels of Fig. 8 show no trend in the line velocities or linewidths with E_{up}, indicating that the velocities and linewidths are dominated by kinematics. The middle panel of Fig. 8 shows that the line morphologies also cluster by linewidth, with the blue-dominant lines clustering around a mean linewidth of 4.27±0.11 km s^{-1}, whereas the red-dominant lines cluster around a mean of 6.90±0.34 km s^{-1}. The disk-tracing lines have the largest linewidths, with values clustering around a mean of 8.00±0.22 km s^{-1}, which is not unexpected if they trace fast-rotating gas close to the (proto)star. The fact that the linewidths of the blue- and red-dominant lines are less than those of the disk-tracing lines could be explained if these lines are predominantly tracing the emission on the blue- and redshifted side of the circumstellar structure, respectively.

Figure 9 shows the peak positions within integrated zeroth-order moment maps that were made for all lines with detections >20 σ. The zeroth-moment maps were made by integrating a spectral slab centered on -52 km s^{-1} with a width of 20 km s^{-1}. The peaks of the zeroth-moment maps are distributed differently for each line type. In the case of the disk-tracing lines, the peaks line up close to the disk midplane, slightly shifted to the blueshifted, northeast side of the disk. Most of the blue-dominant lines peak far into the blueshifted side of the disk, $\sim$0.22″ or $\sim$920 au from the continuum peak to the northeast along the disk midplane at PA$\sim$60° (J15). At this angular separation from the continuum peak along the disk midplane, these points also appear to show a bar-like distribution that has a PA perpendicular to that of the disk midplane. The peaks of the unblended and unambiguous lines in the zero moment maps for the red-dominant lines (Fig. 9) lie in a tight cluster slightly southwest of the continuum peak (on the redshifted side of the disk).

3.2.3. Disk-tracing Lines

In J15, we presented the observed CH$_3$CN J=13-12 K ladder emission from AFGL 4176, which was well-modeled by a disk in Keplerian rotation. However, including CH$_3$CN, we find a total of 55 lines detected within the same observation that have a similar symmetric velocity gradient and therefore are also likely to be tracing the disk. These molecules include eight of the nine (excluding H$_2$CCN, which is too faint) N-bearing molecules listed in Table 5, and HCOOH (formic acid). Therefore, given that all of the molecules that include nitrogen that are bright enough to determine their mor-

phology are disk-tracing, the presence of nitrogen in the molecules of these observations appears to indicate that it is a good disk tracer.

To quantify the similarity between the CH$_3$CN J=13-12 K ladder lines, which we previously determined traced the disk via radiative-transfer modeling in J15, and the remaining lines that we refer to as disk-tracing, we calculated a similar combined χ^2 to that produced in Section 3.2.2. In this case, we compared the CH$_3$CN J=13-12 K=7 line that traces the inner disk to the non-CH$_3$CN lines (which included the vibrationally excited CH$_3$CN lines not analyzed in J15). The resulting average reduced χ^2 value is 1.31±0.06, demonstrating the similarity of the non-CH$_3$CN lines (as well as vibrationally excited CH$_3$CN) to the CH$_3$CN lines known to trace the disk. If the CH$_3$CN K=7 line is compared to all of the non-CH$_3$CN lines (excluding the vibrationally excited CH$_3$CN lines), the average reduced χ^2 value is 1.32±0.10, confirming that excluding the vibrationally excited CH$_3$CN lines does not significantly change the result.

Comparing with the results of Bøgelund et al. (2019), we note that they find the velocity gradients seen in four of our eight disk-tracing lines: NH$_2$CHO or HC(O)NH$_2$, CH$_3$CN, C$_2$H$_3$CN, and C$_2$H$_5$CN, as well as in CH$_3$OCHO. We categorize several CH$_3$OCHO lines as disk-tracing, and several others as blue-dominant; therefore, we find that some of these lines trace the disk.

Figure 10 presents zeroth- and first-moment maps of representative lines for each of the nine disk-tracing molecules listed above, as well as the brightest unblended line for CH$_3$CN v$_8$=1. The first-moment maps were created using a 5σ cut, except for the faint NH$_2$CN line, for which we used 3σ. The example lines shown in Fig. 10 are shown in bold in Tables A.1-A.4.

Similar to that found for CH$_3$CN, all the lines shown in Fig. 10 display a velocity gradient across the source with blueshifted emission in the northeast and redshifted emission in the southwest. In Figure 11, we present the PV diagrams of the lines shown in Fig. 10, which also shows their similarity to the CH$_3$CN line, providing further evidence that this group of lines is indeed tracing the disk. For instance, each PV diagram in Fig. 11 shows a velocity gradient from blue- to red-shifted from east to west, and resembles one of the simulated model PV diagrams for a Keplerian disk shown in J15. A few lines, such as HC$_3$N and NS, also clearly show a curve tending to higher velocities at smaller radii in the lowest contours in the top left and bottom right quadrants of the PV diagram, as expected in the case of Keplerian rotation.

Both J15 and Bøgelund et al. (2019) found that more excited lines, which trace hotter gas close to the central
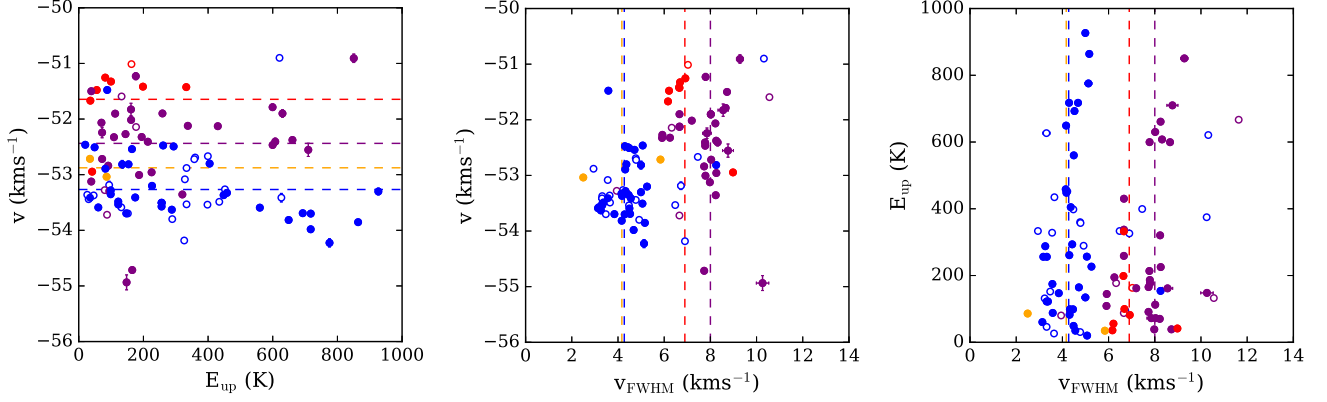
Figure 8. Fitted peak velocity of lines with detections $>20\,\sigma$ plotted against the energy of the upper level (left panel) and linewidth (middle panel). The right panel shows the energy of the upper level against the linewidth. The red, purple, blue, and orange dots represent red-dominant, disk-tracing, blue-dominant, and outflow-tracing transitions, respectively. The empty points show lines that have ambiguous identifications or have another line within $10\,\mathrm{MHz}$ ($\sim 12\,\mathrm{km\,s^{-1}}$) and therefore may be blended. Dashed horizontal lines show the mean peak velocity. The dashed vertical lines show the mean linewidth, for each line morphology type.
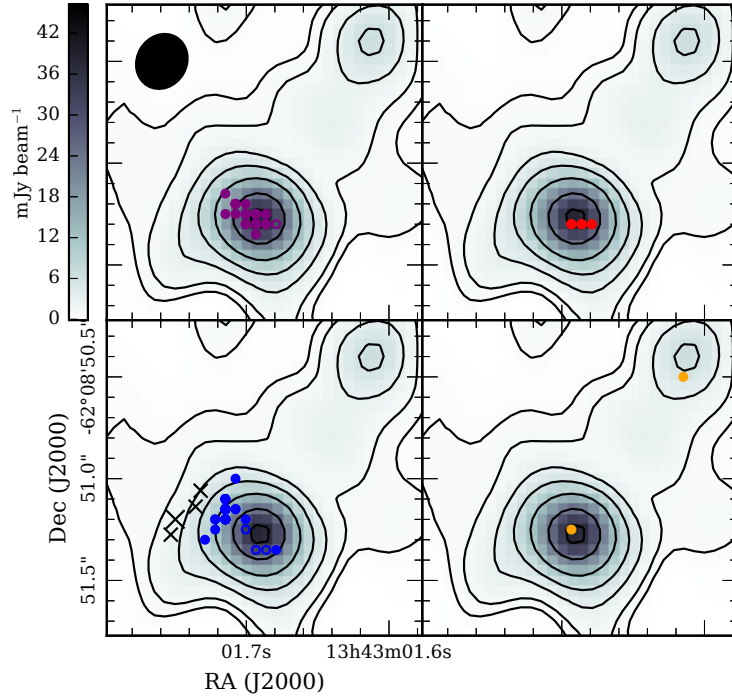
Figure 9. Peak position in integrated zeroth-moment maps for lines with detections $>20\,\sigma$. Each sub-panel shows the positions for a given line morphological type: Purple, red, blue, and orange dots represent the peak positions of the disk-tracing, red-dominant, blue-dominant, and outflow-tracing transitions, respectively. The empty points show lines that have ambiguous identifications or have another line within $10\,\mathrm{MHz}$ ($\sim 12\,\mathrm{km\,s^{-1}}$) and therefore may be blended. The error in these positions is on the order of the pixel size. The beam is shown in the top left panel. Grayscale and contours show the $1.2\,\mathrm{mm}$ continuum emission, with contours at 5, 10, 25, 50, 100, 200, 300, 400 $\times 0.12\,\mathrm{mJy\,beam^{-1}}$. Black crosses in the bottom left panel show Class II methanol masers from Phillips et al. (1998).

source, have smaller extents and steeper velocity gradients. Therefore, it is likely that the spatially compact lines trace the disk while the extended lines (e.g. low K transitions of CH_3CN and HC_3N) may also trace part of the envelope. This is supported by Figure 12, where we plot the area of all pixels brighter than half the peak flux density in the zeroth-moment map for the disk-tracing lines against their linewidth, showing a trend of more compact emission for lines with larger linewidths.

Due to the fact that it traces extended emission and is blended with a CH_3OH line on the redshifted side, HC_3N is the least clear-cut of the disk tracers. However, HC_3N evaporates off dust grains at a similar temperature to CH_3CN (Collings et al. 2004; Jaber Al-Edhari et al. 2017), the HC_3N J=28 – 27 transition we detect has a similar critical density to that of CH_3CN J =13-12 K=3 ($>1\times10^6$ and 1.5×10^6 cm^{-3} at 100 K, respectively), and the energies of the upper levels of the transition are similar (177.26 and 144.63 K). Therefore, assuming similar abundances, it is not surprising that the extent of the HC_3N emission shown in Fig. 10 is similar to that of CH_3CN.

Several of the disk-tracing lines trace only the inner several hundred to thousand astronomical units of the source, namely NH_2CN, CH_3CN v_8=1, C_2H_3CN and C_2H_5CN. These lines have reasonably high excitation temperatures (205.25, 607.71, 278.02, and 169.27 K), although lower abundances of these molecules also probably play a role in their smaller extent.

Formamide or $HC(O)NH_2$ is particularly interesting, in that the lines show double-peaked line structures (see spw2 in Fig. 5 and Fig. 13), which may indicate a lack of lower-velocity envelope emission from these lines, which would "fill in" the line profile close to the line center. In Section 3.2.7 we discuss how the majority of lines (including those for $HC(O)NH_2$) are likely to be optically thin, so optical-depth effects will not be important. However, missing flux issues due to interferometric filtering of emission at larger scales may complicate this interpretation. Nevertheless, the moment maps shown in Fig. 10 show that, along with vibrationally exited CH_3CN and $HCOOH$, the $HC(O)NH_2$ emission displays a clear velocity gradient, is confined to the inner region of the disk, and is thus a good disk tracer.

3.2.4. *Blue-dominant Lines*

We find a total of 85 lines that are categorized as blue-dominant, and that molecules categorized as blue-dominant are predominantly oxygen-bearing. There are five molecules that only have lines with a blue-dominant morphology in Tables A.1-A.4, which are CH_2CO, CH_3OH, $HCOCH_2OH$, CH_3OCH_3, and H_2CS. There

are four molecules that have lines that are designated mostly blue-dominant but with a few categorized as disk-tracing: CH_3OCHO, C_2H_5OH, CH_3COCH_3, and aGg'-$(CH_2OH)_2$. The only oxygen-bearing molecule that does not have lines that are categorized as blue-dominant is $HCOOH$. Conversely, H_2CS is the only line that is not oxygen-bearing that is categorized as blue-dominant.

Figure 14 provides an example of the morphology of a blue-dominant line, showing the CH_3OH 17(3,15) $\rightarrow$ 17(2,16) A^{+-} line with a rest frequency of 256.228714 GHz. As introduced in Section 3.2.2, this example methanol line, as well as the other blue-dominant lines, shows a blue-shifted bar-like morphology that is perpendicular to the disk plane. In this example, this is especially noticeable in the -53.78 km s^{-1} channel. At higher, redshifted velocities, the emission reaches around the peak continuum position toward the southwest, suggesting a possible ring or shell-type structure.

Notably, the distribution of the brightest emission bears resemblance to the distribution of the four known Class II methanol masers in the region (Phillips et al. 1998), which are shown as crosses in Fig. 14 and in the bottom left panel of Fig. 9. The brightest maser component, component C in Phillips et al. (1998), shown as a slightly larger cross in Fig. 14, has a velocity of -54.5 km s^{-1}, which is blueshifted compared to the systemic velocity ($\sim$-52 km s^{-1}), and is slightly blueshifted compared to the mean velocity of the blue-dominant lines (-53.3 km s^{-1}). As seen in figure 4(a) of Phillips et al. (1998), the four maser points are all blueshifted, with velocities between -56 and -52 km s^{-1}. Given the spatial and velocity coincidence of the masers and thermal emission, it is likely that these are tracing the same physical structure.

Due to the low inclination of the system ($i \sim 30°$ between the rotation axis of the disk and the line of sight, J15), it is unlikely that inclination and thus optical-depth effects would be causing the asymmetry of emission (see also Section 3.2.7). Instead, there may be something in the disk or circumstellar environment that is desorbing the oxygen-rich blue-dominant molecules from the dust grains at this position to increase their local abundance, such as a shock.

Previously, Bøgelund et al. (2019) found that some of the O-bearing species they detect toward AFGL 4176 peaked 0.2″ offset from the continuum peak; however, they also state there are no large differences in the spatial distribution of N- and O-bearing species. In contrast, as discussed above, we find that the blue-dominant lines, which show an asymmetric morphology often peaking in the blue-shifted side of the disk and
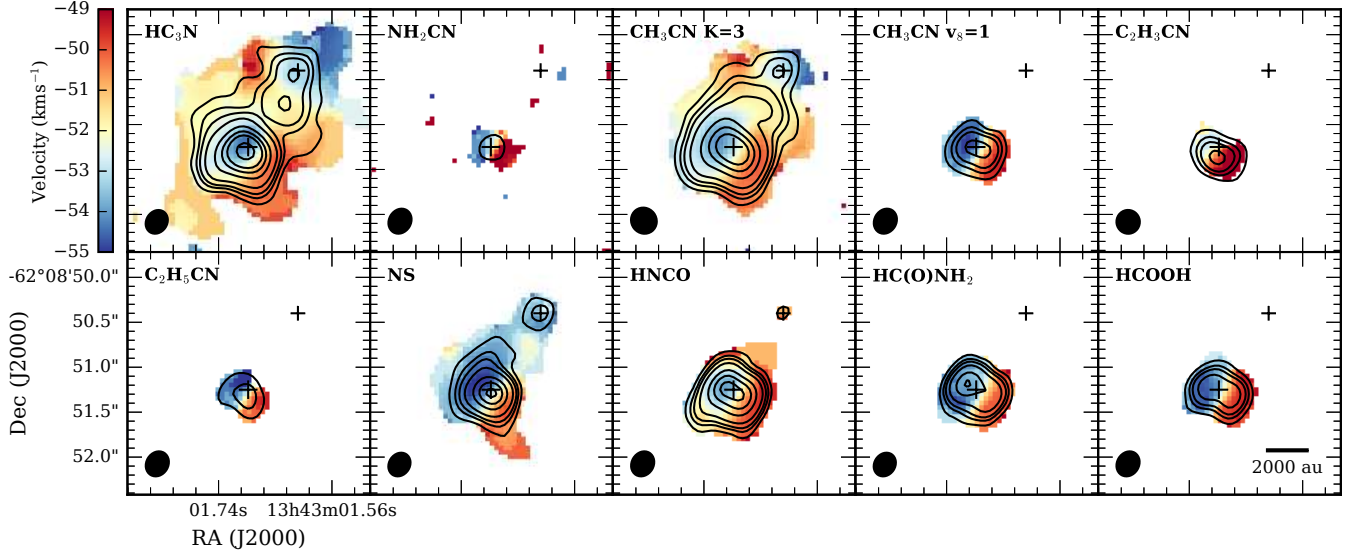
Figure 10. Zeroth- (contours) and first-order (colorscale) moment maps for the nine disk-tracing molecules observed in the ALMA data, which are shown in bold in Tables A.1-A.4. Except for CH$_3$CN K=3, the brightest, unblended line was chosen if possible. The velocity ranges were chosen to cover the full range of the line emission for each line. The contours are shown at 5, 10, 15, 25, 50, 75, 100, and 150 × the local rms noise, which is 0.021, 0.016, 0.017, 0.016, 0.008, 0.012, 0.019, 0.018, 0.014, and 0.013 Jy beam^{-1} km s^{-1} for each panel, respectively, read from left to right, then top to bottom. The only available HC$_3$N line is blended with a CH$_3$OH line and was therefore only integrated between -60 and -49 km s^{-1}. The positions of mm1 and mm2 are shown as large and small plus signs, respectively.
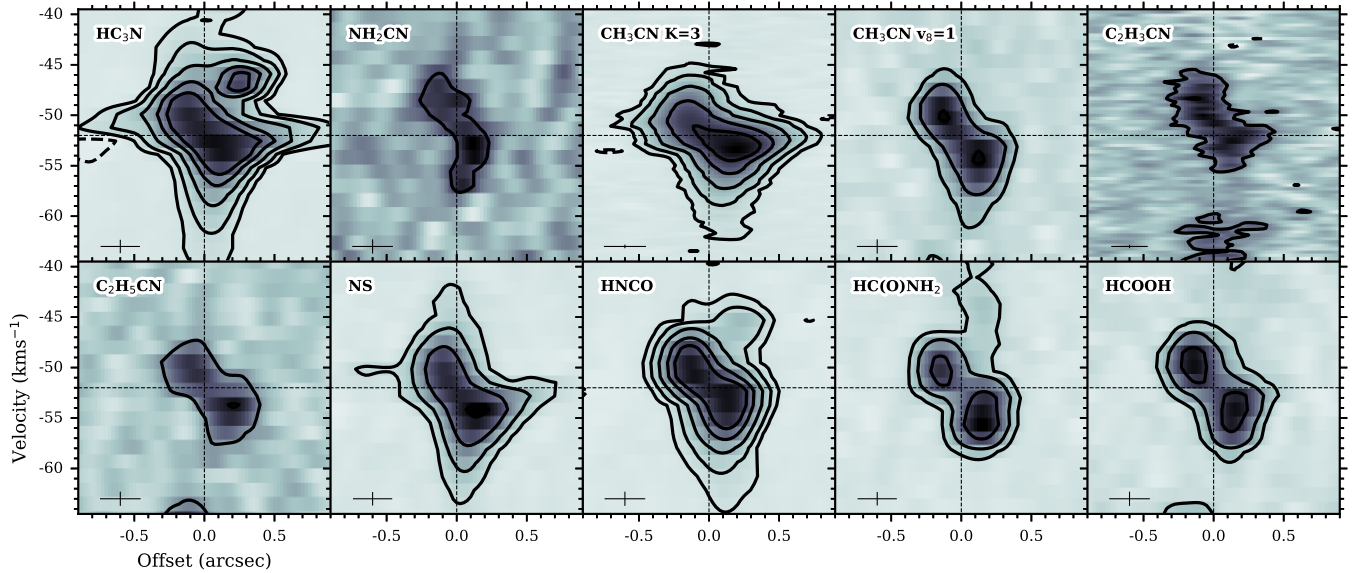
Figure 11. Position-velocity diagrams of the disk-tracing lines shown in Fig. 10, averaged along a cut centered on the mm1 continuum peak position, with PA = 61.5° and width = 1″. The horizontal and vertical dashed lines mark the position of the continuum peak and a velocity of −52 km s^{-1}. The crosses in the bottom left of each panel show the observational spatial and spectral resolution. Contour levels are -3, 3, 10, 25, 50, and 75 × σ, which is 2.3, 1.0, 1.7, and 1.4 mJy beam^{-1} for spws 0-3, respectively.
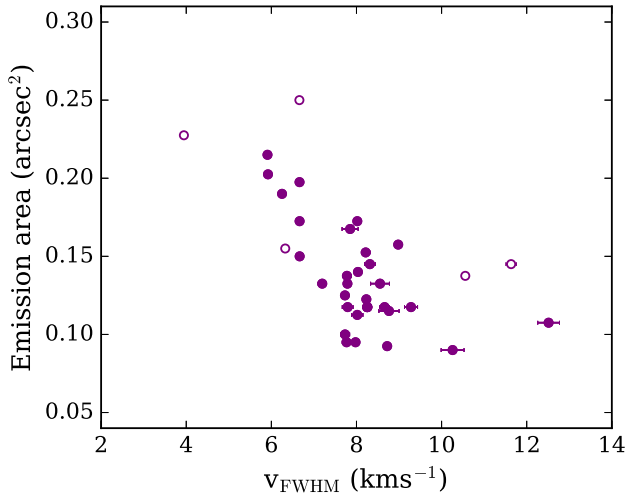
Figure 12. The area of all pixels above half the peak flux density in their zeroth-moment map against linewidth for all disk-tracing lines. The empty points show lines that have ambiguous identifications or have another line within 10 MHz ($\sim$12 km s^{-1}) and therefore may be blended.
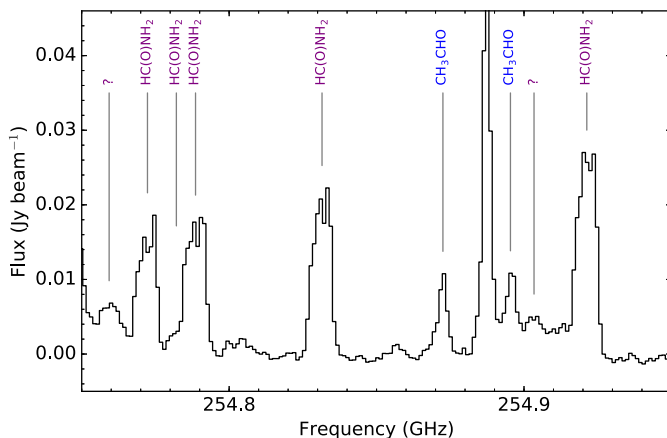
Figure 13. Spectrum showing several example formamide lines in the upper portion of spw2. The different line label colors denote different types of line morphology: purple is disk-tracing and blue is blue-dominant.

are mostly O-bearing, have a very different morphology to that of the disk-tracing or N-bearing species. Further, the association of the blue-dominant line emission with the methanol masers also indicates that different physical processes are involved with the production of the emission from disk-tracing and blue-dominant lines, and thus N- and O-bearing lines. The difference in our findings could be attributed to the fact that Bøgelund et al. (2019) fit Gaussians to the zeroth-moment maps of each line and determine the peak position from these

fits, whereas we inspected the channel maps for each line (e.g., Fig. 14) to determine its morphological type. We also note that Bøgelund et al. (2019) find a different velocity gradient in the first-moment maps of CH_3OH, C_2H_5OH, CH_3OCH_3, and H_2CS compared to the molecules they found trace the disk rotation. However, the channel maps of the blue-dominant lines (e.g., Fig. 14) show that these molecules do show a similar velocity gradient to that of the disk-tracing lines, but the emission is often brighter and more extended on the blue-shifted side of the disk.

3.2.5. *Red-dominant Lines*

A subset of the detected lines exhibits a red-dominant morphology; these are the lines SO and SO_2 and their isotopologues. A channel map of an example line, ^{34}SO $^3\Sigma$ N,J = 6,6 $\rightarrow$ 5,5 is shown in Fig. 15. This figure shows that ^{34}SO, like other lines of this type, is extended in the redshifted channels and has bright redshifted emission on the southwest side of the disk. Further, both mm1 and mm2 are traced by the ^{34}SO emission.

Similarly to the blueshifted lines, it is difficult to explain the asymmetry of the emission in these lines by optical-depth effects, and thus there may be something present or occurring in the disk or surroundings that has liberated SO and SO_2 from the dust grains. One explanation would be a shock, similar to that seen in SO at the centrifugal barrier toward low-mass protostars (e.g. Sakai et al. 2017); however, it is not clear what would differentiate it from the shocks that may be producing the emission on the blueshifted side of the disk in the blue-dominant lines.

3.2.6. *Outflow-tracing Lines*

The molecules whose lines trace extended emission on scales of $\sim$2-10$''$ (e.g., Fig. 7), which we have interpreted as emission from the outflow or outflow cavity walls (see Section 5.1), are the sulfur-bearing molecules $C^{34}S$, H_2CS, as well as CH_3CCH. We note that while H_2CS exhibits blue-dominant morphology on the scale of the disk ($\sim$1$''$), there is also larger-scale H_2CS emission, which we interpret as from the outflow. As $C^{34}S$ is the best example of this morphology type, but we have complementary APEX data, we postpone a discussion of the combined ALMA+APEX $C^{34}S$ emission to Section 5. We note that Bøgelund et al. (2019) also find that the emission from CH_3CCH is morphologically double-peaked.

3.2.7. *Effect of optical depth on line morphologies*

To estimate whether some of the line emission was optically thick, we took the spectral cubes in brightness
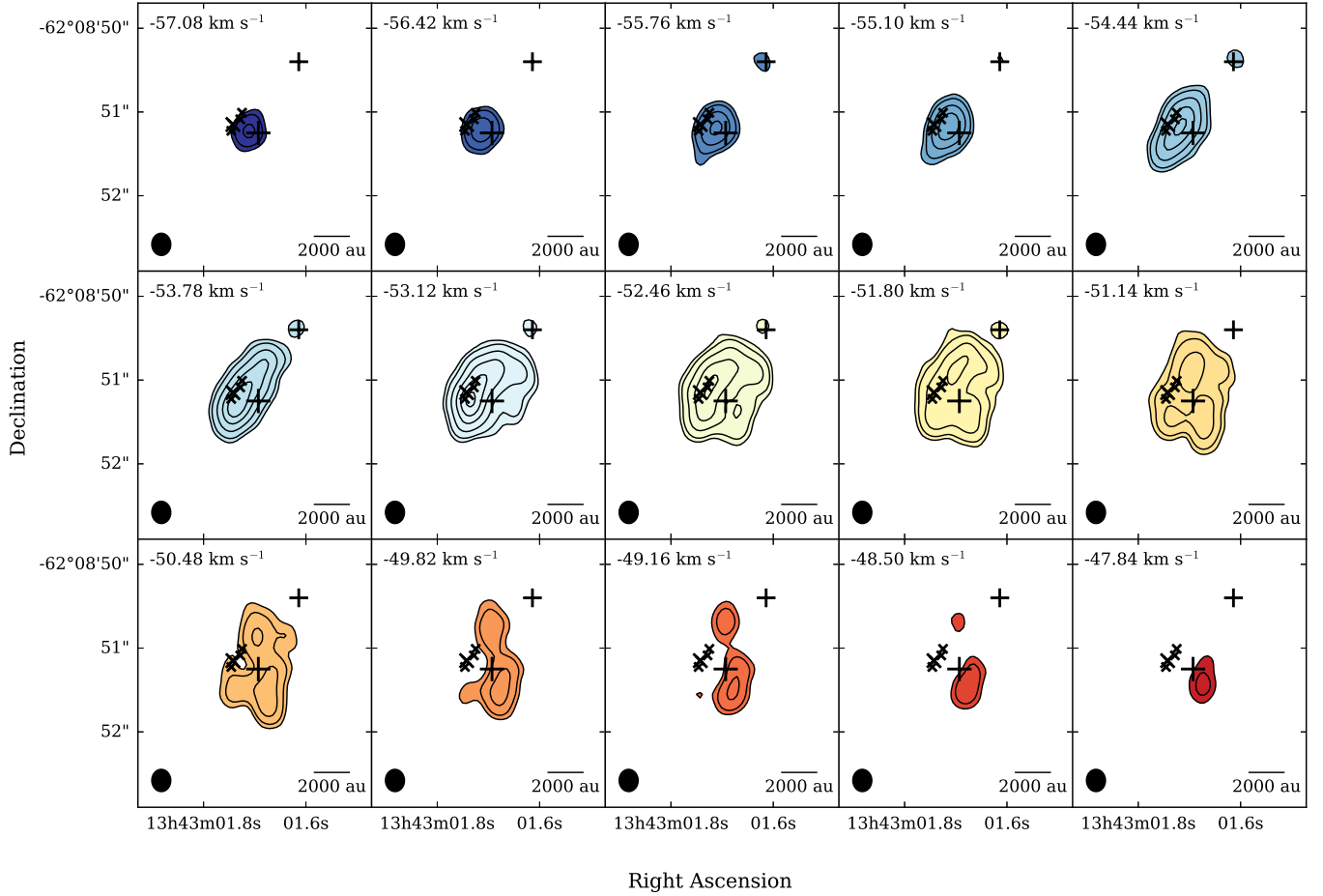
Figure 14. Channel map of the CH$_3$OH 17(3,15) $\rightarrow$ 17(2,16) A^{+-} line imaged at 0.66 km s^{-1} spectral resolution between -57.08 and -47.84 km s^{-1}. The contours show 5, 10, 25, 50, 75, and 100 $\times$ 3.4 mJy beam^{-1} (the local rms noise), and the contours are filled with a colorscale to represent the channel velocity. The positions of mm1 and mm2 are shown as large and small plus signs, respectively, and the crosses represent the Class II methanol maser components found by Phillips et al. (1998).

temperature for each spectral window and compared it to the map of excitation temperature T_{ex} derived from CH$_3$CN by J15. We found that the maximum optical depths across the image cube for each line were <1 for all but the brightest lines: the brightest line of methanol in spw1, and the four brightest methanol and the brightest SO$_2$ lines in spw2. We note that the lines shown in Figs. 14 and 15 are both optically thin.

Although some of the brightest lines may be optically thick, the same asymmetry and blue/red-shifted morphology is seen in the line emission in their corresponding optically thin isotopologue lines (e.g., ^{13}CH$_3$OH and ^{34}SO$_2$, the latter of which is shown in Fig. 6), indicating that the observed morphologies are not due to optical-depth effects. This is further seen in Fig. 8, where there is no trend in velocity seen with E$_{up}$. For any pair of lines of the same species with different E$_{up}$, the higher E$_{up}$ lines trace hotter and denser gas closer to the source compared to the lower E$_{up}$ lines. In the case where both

lines are optically thin, they will trace all of the material/molecule along the line of slight that is hot enough to produce emission in that transition. Thus, in the optically thin case the columns are symmetrical around the source along the line of sight, and therefore the two lines will be centered at the same velocity. In the case where the column is high enough to make the lines optically thick, they will only trace material up to an optical depth of ~1, thus missing different amounts of material from the back side of the circumstellar structure. Therefore, given we expect that the envelope is infalling, this difference in the material traced by both lines will lead to a difference in the average velocity of the two lines. As this velocity difference is not seen between different E$_{up}$ lines in Fig. 8 we can deduce that optical-depth effects are not important.
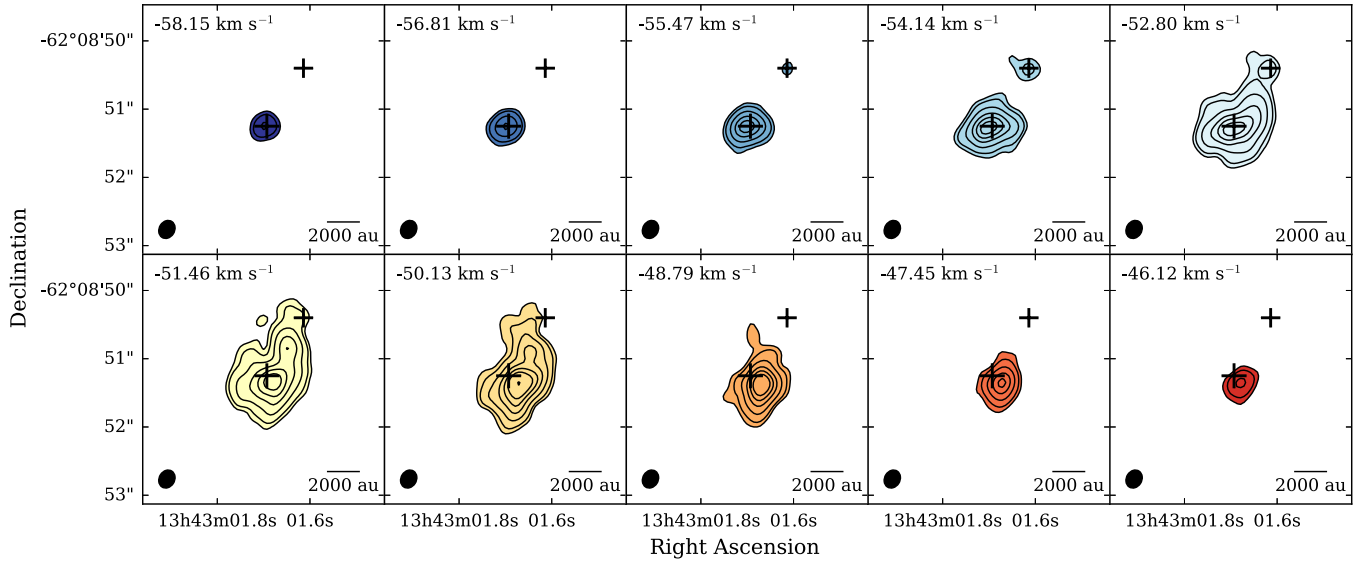
Figure 15. Channel map of the ^{34}SO $^3\Sigma$ N,J = 6,6 → 5,5 line imaged at 1.33 km s^{-1} spectral resolution between -58.15 and -46.12 km s^{-1}. Contours show 5, 10, 25, 50, 75, 100, 150 × 2.1 mJy beam^{-1}, and the contours are filled with a colorscale to represent the channel velocity. The positions of mm1 and mm2 are shown as large and small plus signs, respectively.

3.2.8. *The Nature of mm2*

With a total mass inferred from its dust emission of 3.6 M$_\odot$, mm2 is the second most massive core in the field. The column density of mm2 derived from the dust emission in Section 3.1 is 2.9×10^{24} cm^{-2}. In comparison, the column density of CH$_3$CN molecules derived in J15 also peaks toward mm2 but is 1.6×10^{15}cm^{-2}, which assuming a CH$_3$CN abundance of 10^{-8} corresponds to an H$_2$ column density of 1.6×10^{23}cm^{-2}. Given the discrepancy of an order of magnitude, this probably indicates that the CH$_3$CN abundance in mm2 is much lower than 10^{-8}.

Figure A.3 provides average spectra in the four spectral windows centered on the position of mm2 in a circular aperture of 0.5″ in radius. The most obvious difference between the spectra of mm2 and mm1 is that lines of CH$_3$CCH and C^{34}S are comparatively brighter in the mm2 spectra. There is also a lack of emission from more complex molecules. Methanol and H$_2$CS are present, as well as many sulfur-bearing lines such as SO, SO$_2$, and O^{13}CS. Several lines categorized as disk-tracing lines, such as NS, HC$_3$N, HNCO, and CH$_3$CN, are also present, although they do not appear to trace a disk at the position of mm2 (see Fig. 10). This is likely because these lines, in addition to tracing the disk of mm1, also trace part of the circumstellar envelope or outflow around mm1.

The presence of bright CH$_3$CCH and C^{34}S emission at the position of mm2, which appears to form part of the emission from the outflow or outflow cavity walls,

suggests that mm2 is possibly a knot in the blueshifted side of the jet or outflow from mm1. This is supported by the fact mm2 is blueshifted in comparison to mm1 (figure 3 in J15) and by the location of mm2, which lies along the axis of the mm1 disk. Further, the presence of jet shocks would increase the density, temperature, and linewidth at the position of the shock, supported by the elevated temperature and linewidth found at the position of mm2, with values of ∼-53 km s^{-1}, ∼200 K and ∼5 km s^{-1} respectively (J15). Thus, although we cannot rule out that mm2 is another protostar, which would make this system a binary with a separation of 1″ or 4200 au, there is reasonable evidence that mm2 is associated with shocks in the outflow or jet from mm1.

4. ATCA RESULTS

The section below details the most important results derived from the ATCA observations. Given the large number of observed ATCA bands and thus resultant images (see Table 3), we do not present all of these here, although the images can be obtained in the accompanying online data.[10] We list the ATCA bands with accompanying figures in the final column of Table 3.

4.1. *Centimeter Continuum*

In Fig. 16 we present the ∼1″ resolution ATCA 22 GHz or 1.36 cm continuum emission observed in April 2012. The emission shows a large HII region extending

---

[10] http://doi.org/10.5281/zenodo.3369188
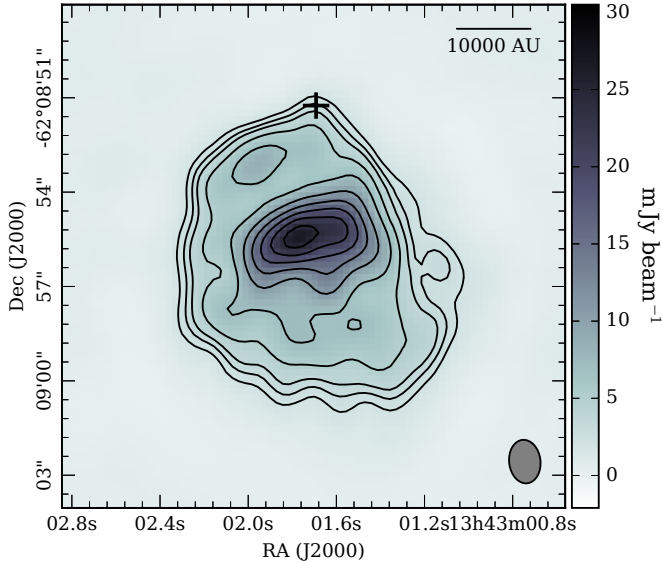
Figure 16. ATCA continuum emission toward AFGL 4176 at an effective frequency of 22.004 GHz or 1.36 cm (combined image from the two 20.434 and 23.712 GHz bands observed in April 2012) shown in grayscale and black contours (local $\sigma = 0.7\,\mathrm{mJy\,beam}^{-1} \times$ -3, 3, 4, 5, 7, 10, 15, 20, 25, 30, 35). The position of mm1 is shown as a plus sign. The ATCA synthesized beam is $1.39 \times 1.00''$, PA $= 6.53°$, and is shown in the bottom right corner.

$\sim 10''$ to the south of mm1, and is very similar in morphology to that presented by Ellingsen et al. (2005) at 8.59 GHz with ATCA in the 6A array. The source mm1 itself is coincident with the northwest part of this extended emission, but there is no specific peak at this position. Ellingsen et al. (2005) measured an integrated flux density of 363 mJy at 8.59 GHz for the extended HII region with the 6A array. The corresponding flux density of the emission we measure at 23.712 GHz with the 1.5B array, the image with the lowest noise, is 300 ± 30 mJy (assuming a 10% absolute flux calibration error). Given these observations have similar beam sizes, this would indicate a spectral index α of -0.19 ± 0.14, which is consistent with an optically thin extended HII region.

The higher-resolution 24.328 GHz or 1.23 cm continuum image taken with the 6A array in September 2012 is shown in Fig. 17, along with the ALMA 1.21 mm continuum as orange contours. There is a bright bar of 1.23 cm emission in the south of the image, which is coincident with the millimeter sources mm3, mm12, mm13, and mm17. Therefore, these millimeter sources likely form part of the extended free-free emission from the aforementioned bar seen at longer wavelengths, and the masses and column densities given in Table 4 for these
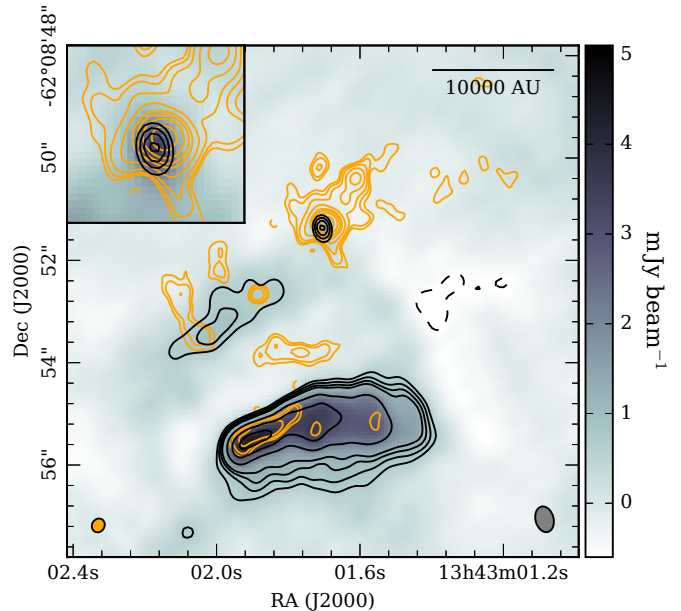
Figure 17. ATCA continuum emission toward AFGL 4176 at an effective frequency of 24.328 GHz or 1.23 cm (combined image from the two 24.139 and 24.533 GHz bands observed in September 2012) shown in grayscale and black contours (local $\sigma = 0.2\,\mathrm{mJy\,beam}^{-1} \times$ -3, 3, 4, 5, 6, 10, 25). Orange contours show the ALMA 1.21 mm continuum emission (local $\sigma = 0.12\,\mathrm{mJy\,beam}^{-1} \times$ -4, 4, 6, 10, 20, 40, 60, 100, 200, 400). The ATCA and ALMA beams are shown in the bottom right and left corners, respectively. The ATCA synthesized beam is $0.51 \times 0.35''$, PA $= 14.45°$. The inset panel shows a zoom-in of the area surrounding mm1 (stretch: -0.6 to $2\,\mathrm{mJy\,beam}^{-1}$).

sources should be viewed with caution as they may be contaminated or wholly explained by ionized gas emission.

There is a second bar of 1.23 cm continuum emission to the north, associated with mm4 and mm7 and pointing radially away from mm1, which forms the brightest emission in a faint arc seen at $<3\sigma$. The source mm1 lies on the edge of this arc, suggesting the centimeter emission could be tracing the ionized edges of a cavity formed by the feedback from mm1. An alternative interpretation would be that the radially positioned bar forms part of a jet from mm1, in which mm4 is a knot.

Finally, there is an unresolved 1.23 cm continuum source associated with mm1, which is shown in further detail in the inset panel of Fig. 17. A gaussian fit to the source gives peak and integrated flux densities of $1.25\pm0.24\,\mathrm{mJy\,beam}^{-1}$ and 1.33 ± 0.44 mJy, respectively. Given the source is unresolved, its dimensions are $< 0.48'' \times 0.18''$ (PA$\sim14.45°$), corresponding to a physical size of $< 2000\,\mathrm{au} \times 760\,\mathrm{au}$. The integrated

flux density from a gaussian fit to the ALMA emission at 1.21 mm is 50 ±4 mJy (J15). The spectral index between 1.23 cm and 1.21 mm is therefore 1.56±0.15. As the smallest spectral index for the emission that can be produced by dust emission is α=2 in the case of extreme grain growth (for which β would tend to 0), this confirms that the emission seen at 1.23 cm cannot be explained by dust emission alone and that some of the emission is due to ionized gas.

We now determine the minimum contribution of ionized gas to the 1.23 cm continuum, assuming that the spectral index of the dust does not change with wavelength. As found in Section 3.1.2, the spectral index observed at 1.21 mm is 3.4±0.2. Since the free-free spectral index cannot be larger than 2, corresponding to optically thick emission, we know that the dust spectral index therefore has to be $> 3.4 \pm 0.2$. Assuming a dust spectral index of 3.4±0.2 as a lower limit, and that all of the 1.21 mm emission is from dust (as an upper limit), we obtain a contribution of $< 0.019^{+0.011}_{-0.007}$mJy from dust at 1.23 cm, meaning that the dust contributes $< 1.4^{+0.8}_{-0.5}$% to the total flux at this wavelength. Therefore, the 3σ upper limit to the contribution from dust is 3.8%.

In Section 3.1.2, we determine that the ionized gas emission contributes <13% of the total flux at 1.21 mm, and above we have shown that the ionized gas contributes >96% of the flux at 1.23 cm. Thus, the resulting ionized gas spectral index between 1.23 cm and 1.21 mm is <0.7.

4.2. *Ammonia Emission*

Figure 18 presents the first- and zeroth-moment maps of the ATCA $NH_3(1,1)$ emission from the region surrounding AFGL4176 on parsec scales. To aid the detection of the extended emission present in the data, we imaged the $NH_3(1,1)$ line with a Gaussian taper of 10″, which was a compromise to ensure detection and reasonable resolution. As previously shown in Johnston et al. (2014), there is a clear velocity gradient across the $NH_3(1,1)$ emission, oriented from northeast to southwest, which is in the same sense as the velocity gradient seen in the molecular gas detected with ALMA on smaller scales (e.g. Fig. 10). Thus, we may be observing the large-scale rotation of the envelope or toroid in which the AFGL 4176 disk lies. Alternatively, the toroid may instead be a filament with a velocity gradient (possibly due to infall) from which the AFGL 4176 mm1 disk has inherited its sense of rotation. However, only one low-surface brightness clump (AGAL 308.944+00.121, Urquhart et al. 2014) lies close to the ATLASGAL source associated with AFGL 4176 mm1 (AGAL 308.917+00.122). Therefore, the cloud

is not clearly linked to another high-mass clump that would cause such a large-scale mass flow. At a flux level of 45 mJy km s^{-1}, the diameter of the zeroth-moment emission spans ∼50″ or ∼1 pc, giving a radius of ∼0.5 pc or 100,000 au.

Fig. 18 also shows the H68α emission in red contours (which we discuss in more detail in Section 5.2), with a white box delineating the area covered by Figure 22. The peak of the H68α emission is roughly coincident with the center of the bar of continuum emission seen at 1.23 cm (Fig. 17). Therefore, the millimeter emission observed with ALMA, including AFGL 4176 mm1, also lies at the far blueshifted end of the toroid, where the velocities are >-51 km s^{-1}, which in fact agrees with the velocities of the molecular lines detected with ALMA (see, e.g., Fig. 8). The peak position of $NH_3(1,1)$ – $13^h43^m01^s.47 -62°09'02.5''$ (J2000) – is offset 11.4″ or 48,000 au from the position of AFGL 4176 mm1. This large offset could suggest that parts of the rotating envelope may be locally unstable to fragmentation, and that fragmentation is occurring on the blueshifted side of the envelope. It could also suggest that, in addition to compact HII region and AFGL 4176 mm1, there may be other forming stars within the envelope. However, we detect no ALMA 1.21 mm continuum emission at the position of the $NH_3(1,1)$ peak (although as this lies 7.5″ from the pointing center, the sensitivity here is decreased by 20%).

We determined the temperature in the large-scale envelope by fitting the $NH_3(1,1)$ and $NH_3(2,2)$ emission. We fit Gaussians to the main component, and hyperfine components in the case of $NH_3(1,1)$, for each pixel in the $NH_3(1,1)$ and $NH_3(2,2)$ cubes and determined the rotation temperature T_{rot} via

$$T_{rot} = \frac{-T_0}{\ln\{\frac{-0.283}{\tau} \ln[1 - \frac{S_{peak}(2,2)}{S_{peak}(1,1)}(1 - e^{-\tau})]\}} \quad (8)$$

(Ho et al. 1979), where $T_0 \simeq 41.5$ K, τ is the optical depth of the main line, and $S_{peak}(1,1)$ and $S_{peak}(2,2)$ are the fitted peak fluxes associated with each line. The kinetic temperature T_k was then found by iteration using the relationship given by Walmsley & Ungerechts (1983) and updated by Swift et al. (2005),

$$T_k = T_{rot} \left(1 + \frac{T_k}{T_0} \ln\left[1 + 0.6\exp\left(\frac{-15.7}{T_k}\right)\right]\right). \quad (9)$$

Only pixels where the peak flux density in the main line was $> 7\sigma$ in both transitions were fit. When fitting for the optical depth τ, we found that the fitted values were close to zero near the center of the toroid or clump,
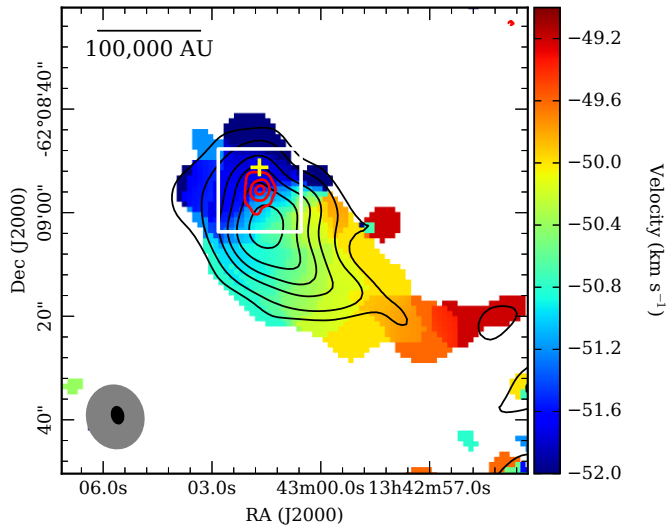
Figure 18. First-moment map of the $NH_3(1,1)$ emission observed with ATCA in colorscale. Black contours show the integrated $NH_3(1,1)$ emission (local $\sigma = 15\,mJy\,beam^{-1}\,km\,s^{-1} \times$ -3, 3, 5, 8, 10, 12, 14). Red contours show the integrated $H68\alpha$ emission (local $\sigma = 30\,mJy\,beam^{-1}\,km\,s^{-1} \times$ -5, 5, 10, 15). The $NH_3(1,1)$ and $H68\alpha$ beams are shown, respectively, in gray and black in the bottom left corner, and their properties are given in Table 3. The yellow plus sign marks the position of AFGL 4176 mm1. The white box shows the area covered by Fig 22.

while they were higher at the edges. Given that this effect is likely due to the lower signal-to-noise at the clump edges, we instead chose to hold τ at zero during the fitting, assuming therefore that the NH_3 clump is optically thin.

We also accounted for the effects of depopulation of the lower two energy levels at higher temperatures by applying a correction factor determined by comparing Equation 9 with the more exact results of Maret et al. (2009). The resulting correction can be approximated by the relation (with both temperatures in kelvin):

$$T_{k,corr} = 1.09\,T_k - 1 \quad (10)$$

The resulting temperature map is shown in Fig. 19, with the integrated $H68\alpha$ emission shown by black contours. The map shows a gradient in temperature, which increases from south to north, peaking at the northwestern edge of the clump. Although this temperature peak does not coincide with the position of mm1, it is interesting to note that it is reasonably nearby. Thus, this temperature gradient may be evidence of heating by mm1 and the compact HII region in the north of the clump.

We determined the total H_2 mass of the toroid or clump from the NH_3 emission using Equations (15) and (16) of Rosolowsky et al. (2008) in the optically thin limit and assuming an NH_3 abundance of $10^{-7.5}$ (Urquhart et al. 2015). The maps of the linewidth and the flux of the $NH_3(1,1)$ derived from the NH_3 line fitting described above were used to determine maps of the parameters σ_ν and the brightness temperature (which can replace $T_{ex}\tau$ in equation 16 of Rosolowsky et al. (2008) in the optically thin limit), respectively. Via this method, we found a map of the column density across the clump and find the total H_2 mass to be 9200 $M_\odot$.

The integrated ATLASGAL flux density at 870 μm is 17.32 Jy (Urquhart et al. 2014). Using Equation 1 and assuming a dust opacity at 870 μm of 0.43 $cm^2\,g^{-1}$ (Draine 2003a,b, with $R_V = 5.5$), a temperature of 35.7 K (the median temperature determined in the analysis above), and the remaining assumptions laid out in Section 3.1.1, we determine the mass of the associated dust and gas clump to be 5100 $M_\odot$. If we instead assume an opacity of 1.85 $cm^2\,g^{-1}$ (e.g. Urquhart et al. 2013) derived from the opacities of the $10^6\,cm^{-3}$ thin ice mantle dust model in Ossenkopf & Henning (1994), we obtain a dust-plus-gas mass of 1200 $M_\odot$. The mass of the clump determined from the Draine opacities is within a factor of two of the mass determined from NH_3, confirming that there is a large reservoir of mass available for star formation around the AFGL 4176 mm1 disk and its surrounding millimeter sources.

Figure 20 shows the first-moment map of the $NH_3(5,5)$ line observed with ATCA, overplotted with contours of the integrated emission of both $NH_3(4,4)$ and $NH_3(5,5)$, as well as 1.23 cm continuum. In contrast to $NH_3(1,1)$ and $NH_3(2,2)$, the emission from these more highly excited transitions lies close to mm1, marked by the large plus sign in Fig. 20. The $NH_3(5,5)$ emission is brighter than that of the $NH_3(4,4)$ and peaks 0.2″ (840 au) to the east of mm1, whereas the $NH_3(4,4)$ emission peaks to the southeast. Correspondingly, the velocities shown in the $NH_3(5,5)$ first-moment map are blueshifted ($\sim$ $-55\,km\,s^{-1}$) compared to most of the lines observed with ALMA (e.g., Fig. 8). The upper energy levels of these two transitions lie at 201.092 and 295.942 K for $NH_3(4,4)$ and $NH_3(5,5)$, respectively. Although no trend in velocity is seen with upper energy level for the lines detected with ALMA, it may be that the $NH_3(5,5)$ emission is tracing a patch of gas hotter than $\sim$200 K within the blueshifted part of the circumstellar material that is not detectable in $NH_3(4,4)$. It is unexpected that the hottest gas is not found at the peak position and velocity of the continuum source mm1, where heating from the young star would excite the gas. This observation may be indi-
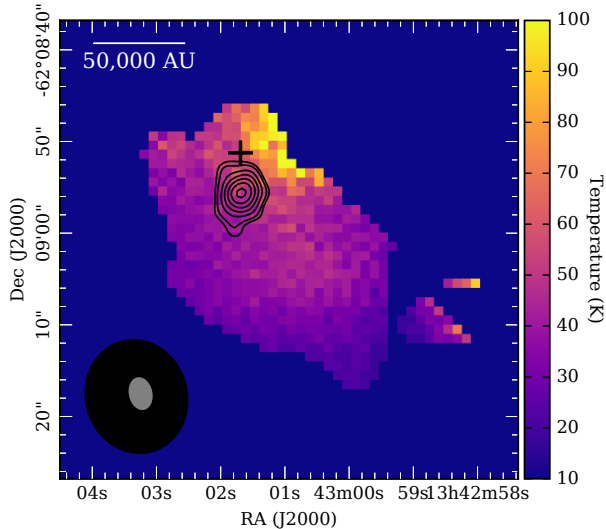
Figure 19. Temperature map ($T_{\mathrm{k,corr}}$) derived from the observed ATCA $NH_3(1,1)$ and $NH_3(2,2)$ emission. Black contours show the integrated ATCA H68α emission (local $\sigma = 30\,\mathrm{mJy\,beam^{-1}\,km\,s^{-1}} \times$ -5, 5, 6, 8, 10, 12, 14, 16). The $NH_3(1,1)$ and H68α beams are shown, respectively, in black and gray in the bottom left corner, and their properties are given in Table 3. The plus sign marks the position of AFGL 4176 mm1.

cating that some process, such as shocks, could be heating the gas in the blueshifted side of the disk. Thus, it appears that similar physical processes are exciting both the $NH_3(5,5)$ and the blue-dominant lines such as methanol that are presented in Section 3.2.4.

5. COMBINED RESULTS

### 5.1. *Outflow-associated Emission from $C^{34}S$*

While other molecules have comparatively compact emission, there are three tracers detected with ALMA that show extended emission that reaches distances > $2''$ from mm1: CH_3CCH, H_2CS, and $C^{34}S$. Figure 21 presents the combined ALMA + APEX $C^{34}S$ (5-4) channel maps, which display emission extended perpendicular to the position angle of the major axis of the disk (shown as a dashed line). There is an arc of emission to the southeast of mm1, seen most clearly in the $-51.31\,\mathrm{km\,s^{-1}}$ channel, coincident with the 1.21 mm continuum sources mm5, mm7, and mm8 (which themselves also follow the same arc, see Fig. 1). In the same channel, there is also a U-shaped arc of emission pointing to the northwest of mm1, with mm1 positioned at the base of the U. Given the small linewidth of the $C^{34}S$ (5-4) emission ($5.8\,\mathrm{km\,s^{-1}}$) compared to the velocities measured for the CO (3-2) outflow presented in J15 (13-$16\,\mathrm{km\,s^{-1}}$ from the v_{LSR}), $C^{34}S$ is unlikely to trace the
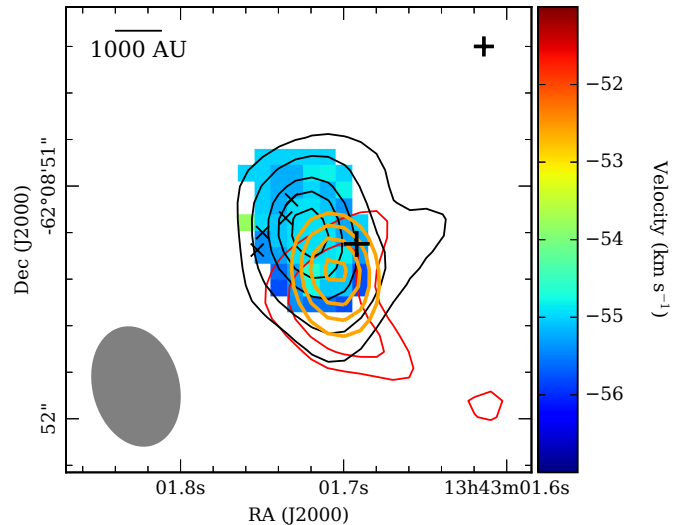
Figure 20. First-moment map of the $NH_3(5,5)$ emission observed with ATCA in colorscale. Black contours show the integrated $NH_3(5,5)$ emission (local $\sigma = 6\,\mathrm{mJy\,beam^{-1}\,km\,s^{-1}} \times$ -3, 3, 5, 8, 10, 12, 14, 16). Red contours show the integrated $NH_3(4,4)$ emission (local $\sigma = 6\,\mathrm{mJy\,beam^{-1}\,km\,s^{-1}} \times$ -3, 3, 4, 5), and orange contours show the 1.23 cm continuum as in Fig. 17. The $NH_3(5,5)$ beam is shown in gray in the bottom left corner, which has similar properties for the $NH_3(4,4)$ and continuum images (see Table 3). The positions of mm1 and mm2 are shown as large and small plus signs, respectively, and the crosses mark the position of the Class II methanol masers detected by Phillips et al. (1998).

fast part of the outflow, but instead a slower wide-angle wind, or dense material in the outflow cavity walls. Interestingly, another example of where $C^{34}S$ was found to be tracing a wide-angle outflow was the Class 0 protostar HH212 (Codella et al. 2014), a source that also has signatures of a Keplerian disk. Codella et al. (2014) find that the $C^{34}S$ emission becomes more collimated at higher velocities, which can be also be seen to the northwest of mm1 in Fig. 21 at $-52.71\,\mathrm{km\,s^{-1}}$ and again more collimated at $-54.12\,\mathrm{km\,s^{-1}}$. They suggest this demonstrates that the wide-angle outflow of HH212 has an onion-like structure, with higher-velocity material closer to the jet axis, which may also be what we are seeing hints of here for AFGL 4176.

Assuming that the $C^{34}S$ emission traces the walls or outer shell of a parabolic outflow described as $z = z_0(\varpi/\varpi_0)^{1.5}$, where z is the height from the x-y midplane, ϖ is the cylindrical radius, and z_0 and ϖ_0 are constants, we can find the half-opening angle of the structure. Taking the inclination of $30°$ found from our modeling of AFGL 4176 carried out in J15, we measured the size of the southeast outflow in the -51.31
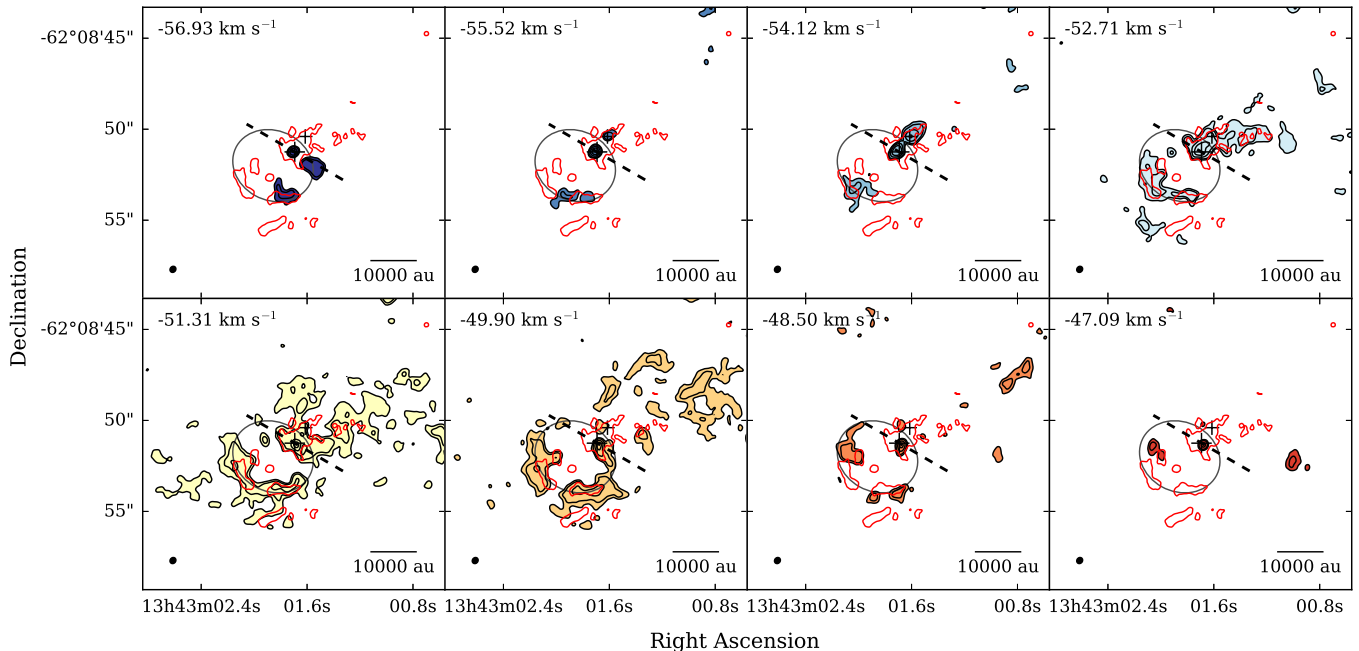
Figure 21. Channel map of the $C^{34}S$ (5-4) line, made using a combination of ALMA and APEX data, imaged at $1.41\,\mathrm{km\,s^{-1}}$ spectral resolution between -56.93 and $-47.09\,\mathrm{km\,s^{-1}}$. Contours show 5, 10, 25, and $50 \times 4\,\mathrm{mJy\,beam^{-1}}$ (the local rms noise), and the contours are filled with a colorscale to represent the channel velocity. The positions of mm1 and mm2 are shown as large and small plus signs, respectively, and the dashed line shows the position angle of the disk seen in 1.21 mm dust continuum ($59°$). The red contour shows the 5σ 1.2 mm continuum emission. The gray ellipse traces the loops seen in the SE side of the outflow (see Section 5.1).

and $-49.90\,\mathrm{km\,s^{-1}}$ channels by approximating the emission by an ellipse with a fixed aspect ratio (shown in Fig. 21). This ellipse was measured to have semi-major and -minor axes of $\sim2.2 \times 1.9''$ or $\sim9200 \times 8000\,\mathrm{au}$, respectively. The distance on the sky of mm1 to the center of the ellipse is $\sim1.4''$. Assuming an inclination of $30°$, the true distance between the center of the ellipse and mm1 is therefore $z_0 \sim2.8''$ or $12000\,\mathrm{au}$ at a cylindrical radius of $\varpi_0 =9200\,\mathrm{au}$. From this, we could determine that the half-opening angle of the outflow or cavity wall at $1.5\times10^5\,\mathrm{au}$ is $\sim19°$. This is in reasonable agreement with the half-opening angle of $10°$ at $1.5\times10^5\,\mathrm{au}$ that was assumed for our previous modeling, as this provided a good fit to the SED.

5.2. *Hydrogen Recombination Line Emission*

Hydrogen radio recombination line (RRL) emission was observed and detected with both ATCA and ALMA. The zeroth- and first-moment map of the H68α line observed with ATCA in April 2012 is shown in Fig. 22. We display this line as it was detected with the highest signal-to-noise of all the observed ATCA RRLs. The HII region traced by the H68α emission, like most of the 1.23 cm continuum, lies to the south of AFGL 4176 mm1. The first-moment map shows that there is an

NNW-SSE velocity gradient (red to blueshifted, respectively) in the ionized gas on scales of $10,000\,\mathrm{au}$. This does not agree with the velocity gradient seen in the NH$_3$ emission, which agrees more closely with that of the disk rotation seen in tracers like CH$_3$CN. It is also interesting to note that the central velocity of the H68α line ($\sim -44\,\mathrm{km\,s^{-1}}$) is different to that of the molecular tracers, which lie around -52 to $-53\,\mathrm{km\,s^{-1}}$ (e.g., Fig. 8). We fitted the mean H68α spectrum measured within a $1''$ radius circular aperture centered on $13^h43^m01^s.672$ -$62°08'55.5''$ (J2000). The resulting flux, central velocity, and linewidth are $18.0\pm1.1\,\mathrm{mJy\,beam^{-1}}$, -$44.4\pm0.8\,\mathrm{km\,s^{-1}}$, and $29.0\pm2.0\,\mathrm{km\,s^{-1}}$, respectively, with the stated uncertainties determined only from the scatter in the data. Interestingly, the emission becomes more redshifted closer to AFGL 4176 mm1. If the ionized gas is flowing from AFGL 4176 mm1, this would indicate that the redshifted side of the ionized flow has a higher redshifted velocity closer to the source compared to the systemic velocity of mm1 (v_{LSR}=52-53 km s^{-1}). This velocity structure might be explained by a turbulent jet model (Arce et al. 2007) and the fact that the gas is ionized by radiative ionization or strong shocks in the outflow. Alternatively, the velocity gradient could be

tracing dynamics driven by a separate source within this HII region, and/or by champagne flows due to varying density in the surrounding cloud. This seems the most likely explanation, as the bright bar of 1.23 cm continuum emission in the south of Fig. 17 is coincident with the peak of the integrated H68α emission seen in Fig. 22 and is centered on the velocity gradient within it, indicating that an independent source associated with this bar of continuum emission is probably producing the H68α emission.

We were only able to detect the remaining RRLs observed in December 2012 (H64α, H65α, H67α, and H68α) by finding their mean spectra over the area of sky covering the April H68α emission. We also fit these lines with Gaussians, and determine their peak flux densities to be 13.3±1.4, 12.9±1.9, 14.6±1.9, and 14.9±1.5 mJy beam^{-1}, respectively, which are consistent to within 1σ. Similarly, the velocities of the lines are −43.9±1.3, −47.4±2.4, −41.9±1.9, and −44.5±1.2 km s^{-1}, and the linewidths are 25.5±3.2, 33.7±5.7, 30.5±4.5, and 24.4±2.9 km s^{-1}, which are consistent to within 2σ. As no trends can be deduced from these, the line properties are thus consistent with a single flux, velocity, and linewidth and therefore likely trace a similar range of densities within the HII region.

We also detect H29α with ALMA. This H29α line emission is extended and faint, so that the resulting images are not useful. However, we measured a mean spectrum in an 5″(R.A.) × 3.5″(Dec.) ellipse centered on the same position as the circular aperture used for the ATCA RRLs. This resulted in a 9.3σ detection; the peak flux density, central velocity and linewidth from a gaussian fit are 0.58±0.1 mJy beam^{-1}, -47.8±2.1 km s^{-1}, and 25.7±5.0 km s^{-1}, respectively. Although, due to large uncertainties, the linewidths of the H29α and H64, 65, 67, and 68α lines are consistent within errors, we calculated the probability distribution of electron density n_e for each pair of lines (i.e. H29α paired with one of the remaining lines) using Monte Carlo statistics and the method outlined in Keto et al. (2008). We then multiplied these distributions to find the combined probability distribution for n_e and found the 99.7th percentile provided an upper limit of $n_e < 6.6 \times 10^5$ cm^{-3}, which given the size of the emission would be consistent with a compact HII region.

6. DISCUSSION

6.1. *Comparison to Other Massive YSOs*

We begin our comparison to other forming massive stars with rotating disk-like structures by presenting an updated version of the lower panel of Figure 14 shown by Beltrán & de Wit (2016) in our Figure 23. This fig-
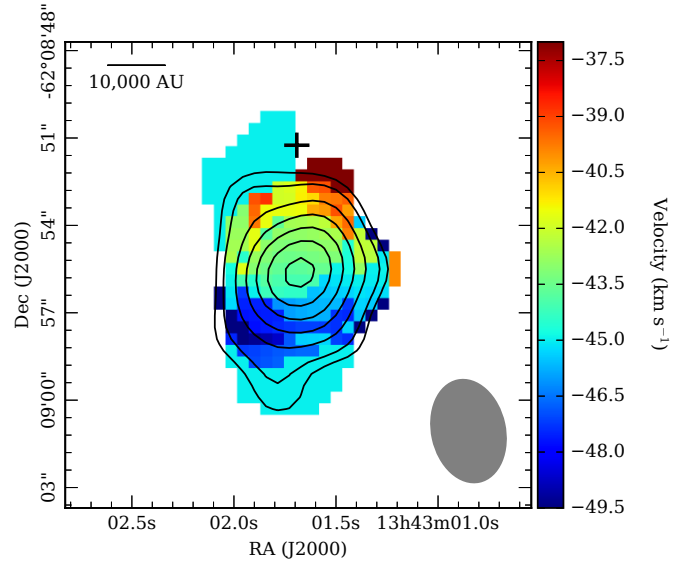
Figure 22. First-moment map of the ATCA H68α emission shown in colorscale. Black contours show integrated H68α emission (local $\sigma = 30$ mJy beam^{-1} km s^{-1}× -5, 5, 6, 8, 10, 12, 14, 16). The black plus sign marks the position of AFGL 4176 mm1. The beam is shown in the bottom right corner; its properties are given in Table 3.
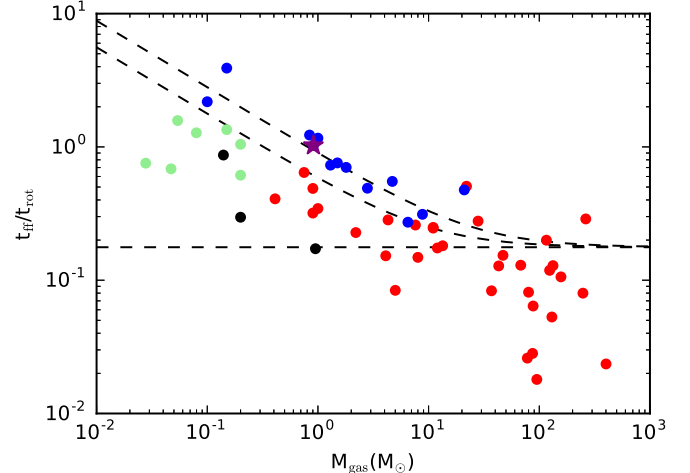
Figure 23. Ratio of the freefall to rotation timescales against M$_{gas}$ for rotating structures around forming stars. The purple star represents AFGL 4176. The red, green, and black points represent the high-mass, intermediate-mass, and Herbig Ae sources presented in Beltrán & de Wit (2016). The blue points represent new or updated sources, which are listed along with AFGL 4176 in Table 7. From bottom to top, black dashed lines indicate theoretical values of t_{ff}/t_{rot} for M$_\star$=0, 10, and 25 M$_\odot$ (see Section 6.1 for further details).

Table 7. Source properties for new and updated sources displayed in Fig. 23

Name	d	L_{bol}	M_{gas}	R_{cont}	R_{vel}	v_{rot}	$M_\star$	t_{ff}/t_{rot}	References
	(kpc)	$(L_\odot)$	$(M_\odot)$	(au)	(au)	$(km\,s^{-1})$	$(M_\odot)$		
AFGL 4176	4.2	1×10^5	0.91	870	1700	4.0	25	1.03	1
W3(H$_2$O) E	2.0	2×10^4	8.8^a	1150	1000	4.0	15	0.31	2
W3(H$_2$O) W	2.0	2×10^4	6.5^a	1150	1000	3.0	15	0.27	2
G328.2551−0.5321	2.5	1.3×10^4	0.15	250	800	9.0	13.5	3.90	3
G328.2551−0.5321 inner env.	2.5	1.3×10^4	4.7	1500	2000	4.5	13.5	0.55	3
G31.41+0.31	3.7	4.4×10^4	21^a	1200	2400	7.5	38^b	0.48	4,5
G23.01−0.41	4.6	4×10^4	1.5	2000	2000	3.5	20	0.76	6
IRAS 18162−2048 MM1	1.7	2×10^4	1.3	291	1700	3.4	14	0.73	7,8
G11.92−0.61 MM1	3.37	1×10^4	0.84	480	850	6.5	34	1.23	9
Orion Src I	0.415	1×10^5	0.1	50	80	13.0	15	2.18	10,11
IRAS 16547−4247	2.9	1×10^5	1.8	∼1000	1190	4.6^c	20	0.70	12
G17.64+0.16	2.2	1×10^5	1.0	120	120	17.9	45	1.16	13
G339.88−1.26	2.1	4×10^4	2.8	530	530	6.0	12	0.49	14

Note—References: 1: Johnston et al. (2015), 2: Ahmadi et al. (2018), 3: Csengeri et al. (2018), 4: Beltrán et al. (2018), 5: Beltrán et al. (2019), 6: **?**, 7: Girart et al. (2017) , 8: Girart et al. (2018), 9: Ilee et al. (2018), 10: Ginsburg et al. (2018), 11: Plambeck & Wright (2016), 12: Zapata et al. (2019), 13: Maud et al. (2019), 14: Zhang et al. (2019a).

^{a}These masses have not been recalculated and instead have been scaled from those given in the respective papers, as a varying temperature was used in their original calculation.

^{b}Due to the updated distance to the source, this mass is an upper limit.

^{c}This velocity was scaled to R_{vel} using the model in reference 11.

ure plots the ratio of the freefall timescale (t_{ff}) to the rotational period (t_{rot}) against the gas mass of the structure (M_{gas}). The t_{ff}/t_{rot} ratio compares the timescale for the gas to collapse under self-gravity in absence of rotation (t_{ff}) to the time for the structure to complete one rotation (t_{rot}). Thus, low values of t_{ff}/t_{rot} indicate that the structure will only complete a small number of rotations before it is accreted on to the central star, so it is unlikely to be able to reach a stable configuration within this time.

Figure 23 has previously been used to separate the two main types of rotating structures observed around forming massive stars: (1) toroids, rotating flattened envelopes, or pseudo-disks, which are massive ($>100M_\odot$) large (~ 10000 au) rotating structures that are not in centrifugal equilibrium and lie at the bottom right of the diagram, and (2) disks in Keplerian rotation that exist over many rotations and lie toward the top left.

The properties of new or updated sources are given in Table 7 and are shown as blue points in Figure 23 (apart from AFGL 4176, which is shown as a purple star). The updated values have been taken from the papers listed

in Table 7; however, some values remain as stated in Beltrán & de Wit (2016).

As assumed in Beltrán & de Wit (2016), we calculate the freefall timescale t_{ff} as

$$t_{ff} = \frac{\pi}{2}\sqrt{\frac{R_{vel}^3}{2GM_{gas}}}, \qquad (11)$$

and t_{rot} the rotation timescale as $t_{rot} = 2\pi R_{vel}/v_{rot}$. We use the radius measured from the line emission (R_{vel}) for the radius in all cases except for the case $R_{vel} < R_{cont}$ where we used the radius measured from the continuum (R_{cont}) for the calculation of t_{ff}. This was to ensure that t_{ff} was evaluated at a radius that contained all of the mass of the structure. Apart from Src I, which has optically thick continuum emission, the masses determined from the dust-continuum emission M_{gas} for all of the sources in Table 7 and Fig. 23 (including AFGL 4176 mm1) have been recalculated to be consistent with the set of assumptions stated in Beltrán & de Wit (2016), namely that the gas-to-dust ratio is 100, the opacity at 1.4 mm is $1\,cm^2\,g^{-1}$ (Ossenkopf & Henning 1994), and the dust opacity index β is 2. The temperature used to

calculate the mass for each source was taken from the papers in Table 7.

Figure 23 also shows several dashed lines, which show the value of $t_{\rm ff}/t_{\rm rot}$ for structures in Keplerian rotation around stars with masses of $M_\star = 0, 10$ and $25\,M_\odot$, taking into account both the mass of the rotating structure and the star such that

$$t_{\rm ff}/t_{\rm rot} = \sqrt{\frac{M_{\rm gas} + M_\star}{32 M_{\rm gas}}}. \qquad (12)$$

Equation 11 assumes spherical symmetry, which given the flattened nature of most of these structures, leads to an overestimate of $t_{\rm ff}/t_{\rm rot}$ (Beltrán et al. 2014). In addition, Equation 11 does not include the mass of the central star $M_\star$, which could change the value of $t_{\rm ff}$ significantly in cases where $M_{\rm gas} \lesssim M_\star$. In fact, if $M_\star$ is included in the calculation of $t_{\rm ff}$ in both of these equations, this has the effect of "flattening" Figure 23, so that the y-axis then becomes a measure of the "Keplerianness" of the structure; the dashed lines also become one horizontal line that shows the positions of structures in Keplerian rotation in the Figure. We will further discuss such theoretically motivated variants of Figure 23 in Kee et al. (submitted), but for now we show Figure 23 as presented in previous studies for a consistent comparison.

As can be seen in Figure 23, the new or updated sources (blue points) lie mostly above the previously known sources in the "disk" area of the diagram. Furthermore, several lie close to or above the upper dashed line for Keplerian structures around a $25\,M_\odot$ star, indicating that recent studies have started to push the discovery of Keplerian-like structures around massive forming stars to even higher stellar masses, into the regime of forming O-type stars. AFGL 4176 falls close to the dashed line representing Keplerian disks around a $25\,M_\odot$ star, in agreement with our previous modeling (J15).

Below, we expand on our brief discussion that was given in Section 1 on the variety of properties seen in disks around forming massive stars. While several sources typify the picture of a scaled-up version of a disk around a low-mass star (e.g. AFGL 4176, G11.92-0.61 MM1, IRAS 18162-2048 or GGD27 MM1, G023.01-00.41, and G339.88-1.26; J15, Ilee et al. 2016; Girart et al. 2018; Sanna et al. 2019; Zhang et al. 2019b), there are in fact a range of disk morphologies found toward high-mass stars. These can include multiple-disk systems (e.g. NGC 7538 IRS1, W3(H$_2$O), and W33A MM1; Beuther et al. 2017; Ahmadi et al. 2018; Izquierdo et al. 2018, in the latter case fed by a large-scale accretion streamer), small disks (e.g. G328.2551-0.5321 and G17.64+0.16; Csengeri et al. 2018; Maud

et al. 2019), and no clear evidence of disks (W51 and IRAS 18566+0408; Ginsburg et al. 2017; Silva et al. 2017).

Within the cluster surrounding the forming high-mass star GGD 27 MM1, Busquet et al. (2019) found a lack of disks close to MM1 ($<0.02\,{\rm pc}$), and that larger and more massive disks only existed at distances greater than 0.04 pc. They also found that the disks were on average smaller than more distributed environments such as Taurus. One explanation for this finding is that the rich cluster environment leads to truncation of these disks via more frequent interactions, which, along with photoevaporation, may also go toward the explanation of smaller and less massive disks in the Orion Nebula Cluster (Eisner et al. 2018). As massive stars are almost always found in clustered environments (e.g. de Wit et al. 2005), it is expected that interactions and accretion streams in clusters are important mechanisms for shaping disks (Bonnell et al. 2003; Bate 2018), whereas, despite their high EUV luminosity, disks around forming high-mass stars are found to be less affected by photoevaporation due to their high optical depth (Tanaka et al. 2017; Kuiper & Hosokawa 2018).

As further observations of forming OB stars at high resolutions are carried out, the distribution of their disk properties, for instance disk mass and radius, will act as an important discriminant between the importance of the cluster-scale environment in massive star formation. By definition, the cluster-scale environment does not play an important role for models of core accretion (McKee & Tan 2003; Krumholz & Bonnell 2009). If disk properties are found to be strongly affected by their cluster-scale environment, this suggests that a more holistic picture of star formation is required that takes into account not just the stellar core but the whole environment in which a massive star is formed.

6.2. Chemistry in massive YSO disks

High-mass star-formation regions are known for their chemical richness, especially in complex organic molecules (COMs), which are defined by astronomers as molecules with ≥ 6 carbon atoms (Herbst & van Dishoeck 2009), and this is indeed seen in our observations of AFGL 4176. Observations of regions such as Orion KL and Sgr B2 have often been at the forefront in the detection of these molecules, due respectively to their proximity and luminosity (e.g. Sutton et al. 1985; Cummins et al. 1986).

Segregation between different groups of species such as that seen in our observations has also been observed in Orion KL and many other massive star-formation regions, most notably between N- and O-bearing species

(Blake et al. 1987; Feng et al. 2015). Often, the N-bearing species are found to be more compact and closely associated with the hot cores, whereas the O-bearing species display more distributed emission (Blake et al. 1987; Öberg et al. 2013; Fayolle et al. 2015; Feng et al. 2015). There is a range of explanations put forward to account for this difference; a recent hypothesis by Suzuki et al. (2018) is that the N-bearing molecules are enhanced by reactions in the hot gas (>100 K) after the warm-up phase and evaporation of the icy dust mantles, as hydrogenation of these molecules into other species is not efficient at high temperatures. However, in contrast, Quénard et al. (2018) find that formamide, one of the disk-tracing and N-bearing species we detect, requires radical-radical grain-surface reactions as well as gas-phase reactions to reproduce the observed abundances (for further discussion, see Bøgelund et al. 2019). Thus, to-date there is no definitive explanation of the chemical segregation of N-/O-bearing species.

As presented in Section 3.2.2, the observed species in AFGL 4176 (including 12 COMs) fall into four distinct morphological groups: disk-tracing, blue-dominant, red-dominant, and outflow-tracing lines. Except for HCOOH, all disk-tracing species contain nitrogen. Conversely, all molecules that we detect that contain nitrogen trace the disk (excluding H_2CCN, which is too faint). As discussed in Section 3.2.3 and can be seen from Fig. 10, these species only trace the inner several hundred to thousand astronomical units of AFGL 4176, similar to the results of previous studies mentioned above. In this way, AFGL 4176 follows the template of N-bearing species being associated with the hottest and densest regions of hot cores.

Given previous difficulties in unambiguously identifying disks around high-mass stars, only a few studies have been carried out to-date that begin to examine their chemistry. Isokoski et al. (2013) previously studied three high-mass YSOs with rotating disk-like structures and compared their chemistry to YSOs at the time thought to not contain disks, and found no significant differences. However, several of the forming stars that were chosen as part of the comparison group that did not have disks have since been shown to contain (multiple-)disk systems (e.g., Maud et al. 2017; Ahmadi et al. 2018).

Specific high-mass YSOs with disks that have been previously studied in relation to chemistry include:

AFGL 2591 VLA3. Jiménez-Serra et al. (2012) found chemical segregation toward an MYSO known to harbor a disk, with the emission from three groups of molecules falling into three morphological types: (1) those peaking on AFGL 2591 VLA3 (H_2S and ^{13}CS), (2) those that avoided the continuum position and were double-peaked (HC_3N, OCS, SO, and SO_2), and (3) CH_3OH, which presented a ring-like morphology. Their observations only covered one N-bearing molecule (HC_3N), which fell into the double-peaked morphological group. They explained the ring-like structure in CH_3OH emission by FUV photodissociation of this molecule within the inner regions of this MYSO. Whereas molecules such as H_2S and CS that peak at the central position can be reformed by gas-phase reactions, once destroyed methanol cannot be efficiently reformed in the gas phase (Garrod et al. 2008). This picture assumes spherical symmetry, but in reality the disk will provide some degree of shielding from dissociation for CH_3OH. Therefore, it is unclear whether CH_3OH would be fully destroyed within several thousand astronomical units of the star.

NGC 6334 I(N) SMA 1b. Hunter et al. (2014) observed the emission from several different molecules toward this source, whose kinematics were found to be consistent with a rotating and infalling (sub-Keplerian) disk, including the N-bearing species HC_3N, CH_3CN, CH_3CH_2CN, and HNCO. However, in this source many of the other observed species (such as CH_3OH) also trace the disk, showing in this case that there does not appear to be any strong chemical segregation of N-bearing species. Instead, the high-temperature transitions are seen to peak toward the source position, whereas the lower-temperature transitions had a double-peaked morphology, indicating a temperature gradient. However, one molecule that did not fit with this picture was HNCO, which had a compact morphology. Hunter et al. (2014) suggested this was the result of destruction of larger parent molecules to form HNCO in the gas phase in the high-temperature inner regions of the MYSO. They also suggested that the disk morphology could provide shielding from dissociation for molecules such as HC_3N, explaining its emission at high velocities close to the source.

G11.92-0.61 MM1. Ilee et al. (2016, 2018) observed a range of species toward this MYSO, finding a Keplerian disk with an enclosed dynamical mass of $40\pm5\,M_\odot$. Species that traced the disk include CH_3CN, CH_3CH_2CN, HNCO, DCN, OCS, H_2CO, CH_3OH, and CH_3OCHO. However, although they displayed the same velocity gradient as other tracers, the emission from the observed methanol lines was offset to the southeast compared to the dust continuum. Many of the observed molecules displayed double-peaked and/or asymmetric emission, except for OCS, which was coincident with the central source. In their modeling of the CH_3CN emission, they find evidence for two temperature components, which they suggest may originate from the hot (>150 K) and dense gas near the midplane, where

CH$_3$CN has thermally desorbed from ice mantles, and from the atmosphere of the disk where gas-phase formation of CH$_3$CN is more important.

G345.4938+01.4677 / IRAS 16562-3959. Guzmán et al. (2018) analyzed emission from 22 different species toward the MYSO G345.4938+01.4677, which has previously been found to contain a compact rotating core seen in SO and SO$_2$ (Guzmán et al. 2014). They categorized their observed molecules into two groups. The first group (the "Shock group") is comprised of species whose emission was similar to SiO, and the second group (the "Continuum group"), containing a broad range of species including COMs such as CH$_3$C$_3$N, is associated with the 3 mm dust-continuum emission. However, they note that except for SO and SO$_2$, no other molecules display the previously seen velocity gradient that indicated a disk may be embedded in the rotating core.

G35.20-0.74 N. Allen et al. (2017) found that N-bearing species, specifically cyanides, were found to be more abundant in part B3 of the source G35.20-0.74 N B, which has previously been found to be a Keplerian disk by Sánchez-Monge et al. (2014). They suggested that this chemical segregation could be from fragments or different sources within a disk or rotating torus, where hot gas-phase chemistry is more active in source B3, producing the larger abundance of N-bearing species.

GGD27 MM1 (HH80-81). Girart et al. (2017) found that sulfurated molecules such as SO$_2$ and SO, as well as H$_2$CO traced a rotating disk. They attributed the production of the sulfurated molecules to shocks occurring at the radius of the centrifugal barrier, also seen toward low-mass YSOs (Sakai et al. 2014; Oya et al. 2016). Another explanation they put forward was UV photodissociation of water in the disk, which allows the reactants to form molecules such as SO$_2$. In contrast, they found that methanol departs from the emission expected for a rotating disk, and that it instead traces the outflow cavity walls. Detected isotopologues of HCN and HC$_3$N also did not show a clear velocity gradient; however, this may have been due to the fact these detections had a low signal-to-noise.

Orion SrcI. Ginsburg et al. (2018, 2019) investigated the dust continuum and molecular lines detected at three frequencies between 0.87 and 3.0 mm toward the disk and outflow in this source, which at a distance of 415 pc constitutes the nearest example of a massive star with a disk. They detected SiO, water, and a host of unidentified lines, which they went on to identify as isotopologues of NaCl, KCl, and possibly AlO. By fitting the position-velocity diagram of the H$_2$O $5_{5,0}$ - $6_{4,3}$ line, which they find is tracing the upper envelope of the disk and the lower section of the outflow, they determine a central mass of 15±2 M$_\odot$. They find that the salt lines also trace the base of the outflow or an upper layer of the disk, but one that lies closer to the disk midplane than water and non-vibrationally excited transitions of SiO. This interpretation is complicated by the fact SrcI is nearly edge-on and the dust emission is optically thick (Plambeck & Wright 2016), masking any line emission close to the midplane. Given the rarity of salt lines in the ISM, Ginsburg et al. (2019) suggest that they may be a unique tracer of disks around massive stars, yet, at least in SrcI, they do not trace the midplane but instead an upper layer in the disk or the base of the outflow.

G17.64+0.16. This MYSO was one of six sources studied by Cesaroni et al. (2017), who found it was the most evolved in their sample, but also the most chemically rich. However, their analysis found clear evidence for a disk. Later, G17 was revisited by Maud et al. (2018) and at higher resolution in Maud et al. (2019). Maud et al. (2018) found a small (∼200 au radius) rotating disk in SiO, with a similar position angle to the continuum emission. Comparable to the results for SrcI (Ginsburg et al. 2018), the presence of SiO in the disk around this source indicates the presence of possibly ionized and turbulent hot shocked gas. Indeed, the detection of compact H30α emission toward the source supports this. Both CH$_3$CN and CH$_3$OH are not found to trace the disk, but instead the cavity working surfaces at the point the wide-angle wind is interacting with the dense envelope. At a higher resolution of 20 mas, or 44 au at the distance of G17, the continuum observations of Maud et al. (2019) uncovered a ring-like structure in a 120 au radius disk. They also found Keplerian kinematics seen in highly excited vibrational lines of water, tracing the hot upper layers of the disk.

G339.88-1.26. In their observations of the MYSO G339.88-1.26, Zhang et al. (2019b) found that within the midplane CH$_3$OH and H$_2$CO trace the infalling, rotating envelope as well as the centrifugal barrier at 530 au, whereas SO$_2$ and H$_2$S trace the centrifugal barrier and outer disk. The radial difference between these two groups of molecules can be attributed to a radial temperature dependence and higher upper energy levels for the molecular transitions observed for the second group. In comparison, they found SiO traces the Keplerian disk as well as the envelope and jet. They suggest that the enhancements in emission close to the centrifugal barrier are either explained by an accretion shock or the irradiated inner edge of the envelope. Outside of the midplane, CH$_3$OH emission is also found to be coincident with methanol masers. The thermal and maser methanol emission both extend perpendicular to the disk midplane in the outflow direction, lying to the

south of the source on the blueshifted side of the disk (see their Figure 12a). Zhang et al. (2019b) explain this morphology, which is very similar to that seen for AFGL 4176, by shocks along the cavity walls of the outflow.

The blue-dominant lines in AFGL 4176, which include CH_3OH and H_2CO and have a ring-like morphology that is brighter on the blueshifted side of the disk, may be explained by similar processes to those seen in G339.88-1.26. Csengeri et al. (2018) also found that CH_3OH is tracing the centrifugal barrier in the MYSO G328.2551-0.5321. Thus, the enhancement of CH_3OH (and other blue-dominant molecules) at a specific radius from AFGL 4176 may be due to accretion shocks in the centrifugal barrier. In addition, the blueshifted asymmetry in the blue-dominant molecules may be either due to self-absorption of the redshifted emission from the centrifugal barrier by the envelope or by an actual asymmetry in the accreting material. Given that no blueshifted asymmetries are seen in our model for the lower K transitions of CH_3CN (J15), which would include the effect of self-absorption by the envelope, and that maser emission is seen coincident with the blueshifted CH_3OH emission (as noted also by Zhang et al. 2019b for G339.88-1.26), we suggest that there is an intrinsic asymmetry in the AFGL 4176 envelope and disk structure. This is also corroborated by the asymmetric NH_3(5,5) emission, which also peaks on the eastern side of the disk.

Looking back on the findings to-date for MYSOs with disks summarized above, it is clear that patterns are beginning to emerge, including the ring-like emission such as SO_2 and CH_3OH tracing shocks, possibly at the disk's centrifugal barrier and that N-bearing species often trace the disk. Nevertheless, there is still a large degree of inhomogeneity in the chemistry of these disks and their inner envelopes, and thus observations of more sources at 100-1000 au scales are necessary to determine if any patterns persist and whether others emerge.

7. CONCLUSIONS

Using observations from ALMA, ATCA, and APEX, we present a detailed view of the circumstellar environment and disk of the MYSO AFGL 4176. Our main results are as follows:

1. At millimeter wavelengths, we detect 17 continuum sources within $5''$ of AFGL 4176 mm1, which is the brightest source in the field and traces the dust emission from the disk found in J15. Their masses range from 0.2 to 13.3 $M_\odot$ and their H_2 column densities range between 2.2 and 8.7 $\times$ 10^{23} cm^{-2}. The spectral index of mm1 be-

tween the two wide spectral windows at 1.2 mm is 3.4±0.2, compatible within errors with ISM dust.

2. We detect a compact continuum source associated with mm1 at 1.2 cm with ATCA. Its deconvolved size is <2000 × 760 au. The spectral index between the two continuum bands at 1.21 mm and 1.23 cm is 1.56±0.15. The dust contributes >87% of the emission at 1.2 mm and ionized gas contributes >96% of the emission at 1.2 cm. The spectral index of the ionized gas component is therefore <0.7.

3. We present ALMA spectra of mm1 at 1.2 mm (in four spectral windows within 238.8376-256.5834 GHz) and identify lines with fluxes >5σ. We detect lines from 25 different molecules, which we can separate into four different morphological types: disk-tracing, blue-dominant, red-dominant, and outflow-tracing.

4. In addition to HCOOH, and apart from H_2CCN, which is too faint, all detected lines that contain nitrogen trace the AFGL 4176 mm1 disk. In particular, vibrationally excited CH_3CN and formamide or $HC(O)NH_2$ appear to be excellent disk tracers.

5. The line morphological types cluster in peak velocity and linewidth. Blue-dominant molecules are predominantly oxygen-bearing. The brightest emission from these lines exhibits a bar-like structure perpendicular to the disk and is associated in position and velocity with a group of Class II methanol masers. We suggest that this emission is due to shocks at the centrifugal barrier in the blueshifted part of the disk. Red-dominant molecules are comprised of SO and SO_2 and their isotopologues that are bright and extended in the redshifted side of the disk.

6. The outflow-tracing molecules are $C^{34}S$, H_2CS, and CH_3CCN, which specifically trace emission from a slow, wide-angle wind or dense structures in the outflow cavity walls. We determine that the half-opening angle of the wide-angle outflow is ~19° at 150,000 au, which being parabolic is much wider at smaller distances from the star.

7. The lack of complex molecules toward mm2, combined with the fact its spectrum is rich in S-bearing molecular lines and that it lies along the disk axis, suggest that mm2 may instead be a knot in the blueshifted part of a jet emanating from mm1, instead of another protostar.

8. The $NH_3(1,1)$ and $(2,2)$ emission from the region traces a large-scale (r$\sim$0.5 pc) rotating clump or toroid with a mass of several thousands of solar masses, which rotates in the same sense as the CH_3CN disk. AFGL 4176 mm1 lies at the NW blueshifted end of the toroid, offset from its center. We determine that the temperature in the clump derived from $NH_3(1,1)$ and $(2,2)$ peaks toward the north of the cloud, suggesting it is heated by mm1 and/or the HII region to the northeast. $NH_3(4,4)$ and $(5,5)$ are detected close to mm1, and $NH_3(5,5)$ likely traces hot gas in the blueshifted part of the disk, similar to the blue-dominant lines detected with ALMA such as methanol.

9. We detect the hydrogen recombination lines H29α, H64α, H25α, H67α, and H68α. H68α traces a north-south velocity gradient in the extended HII region associated with AFGL 4176. This velocity structure may be due to dynamics driven by a separate source.

10. In comparison to other MYSOs that have associated rotating structures, AFGL 4176 mm1 lies, along with several other newly detected disks around massive YSOs, within the "disks" area of the t_{ff}/t_{rot} against M_{gas} figure often used to separate disks from toroids (e.g. Fig. 23). These new sources lie above the previously known disk sources in this Figure, confirming that these structures are more likely to be stable and are associated with more massive MYSOs.

Recent studies have provided several results on the chemistry of disks around forming massive stars, which have begun to show patterns, such as that N-bearing species often trace the disk, specific molecules trace the centrifugal barrier, or methanol lines show unusual morphologies. However, we are still far from constructing a complete picture of the dynamical and chemical processes that govern disks around massive stars, an aim requiring a homogeneous survey of MYSOs to search for disks and study their structure and chemistry.

APPENDIX

A. SPECTRA AND PROPERTIES OF DETECTED ALMA LINES

In this Appendix, we include the spectra of the narrow and wide ALMA spws overlaid with the combined fit of all Gaussians to the detected lines in Figures A.1 and A.2, respectively. We also include the observed spectra in spws0-3 for mm2 in Figure A.3. Tables A.1 through A.4 (also available online[11]) provide the measured properties of the detected lines, and Table A.5 provides a summary of the detected species, including the line databases used for each species, their molecular tag identifiers in each catalog, and the number of lines identified for each morphological type.

---

[11] http://doi.org/10.5281/zenodo.3369188
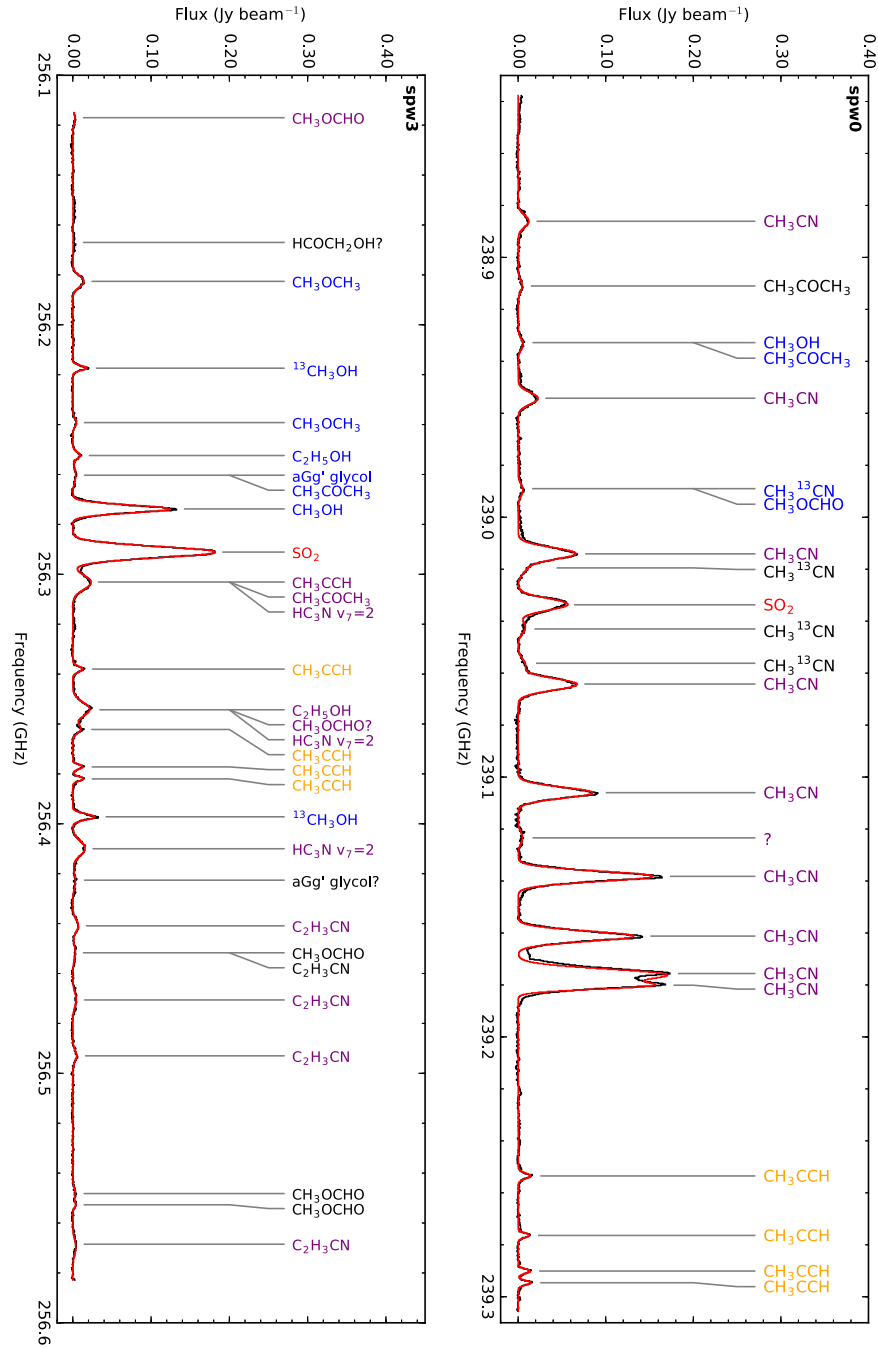
Figure A.1. Spectrum of the two ALMA narrow spectral windows covering 238.8376 – 239.3064 and 256.1146 – 256.5834 GHz as well as the combined fit of all Gaussians to the lines shown in red. The different line label colors denote different types of line morphology: purple is disk-tracing, blue is blue-dominant, red is red-dominant, and orange is outflow-tracing. Line labels are black when no classification was possible.
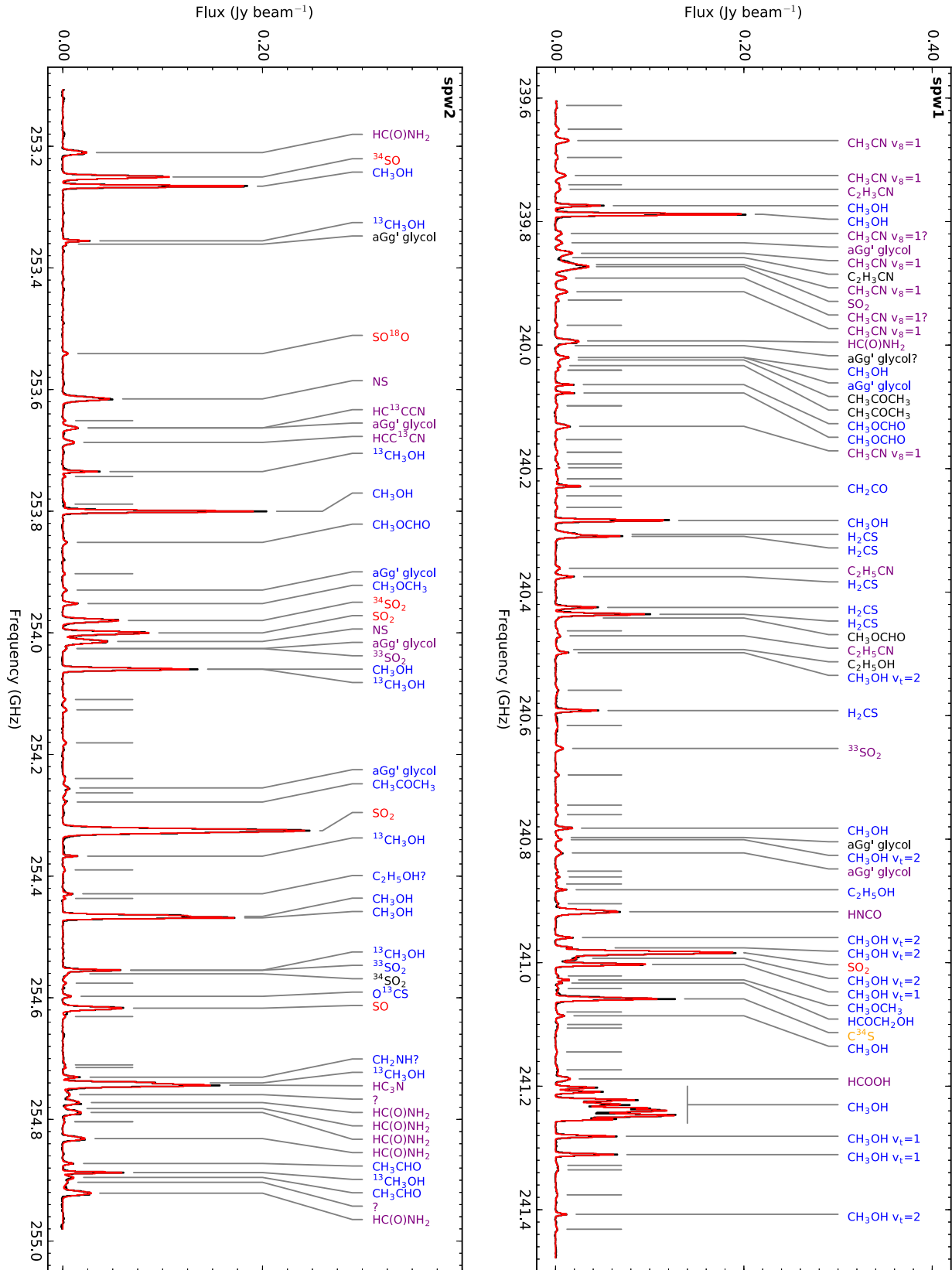
Figure A.2. Spectrum of the two ALMA wide spectral windows covering 239.6035 – 241.4785 and 253.1055 – 254.9805 GHz as well as the combined fit of all Gaussians to the lines shown in red. The different line label colors denote different types of line morphology: purple is disk-tracing, blue is blue-dominant, red is red-dominant, and orange is outflow-tracing. Line labels are black when no classification was possible.

Table A.1. Lines detected in the first narrow spectral window (spw0) covering 238.8376 to 239.3064 GHz

Species	Transition $J(K_a,K_c)$	Rest Freq. (GHz)	E_{up} (K)	Flux (mJy beam^{-1})	v (km s^{-1})	v_{FWHM} (km s^{-1})	Line Morph.[a]
CH$_3$CN	$13(8) \rightarrow 12(8)$	238.843926	537.04	12.28	-52.9	6.7	D
CH$_3$COCH$_3$	$23(1,22) \rightarrow 22(2,21)$ EE	238.868953	144.37	4.50	-52.8	6.7	U
CH$_3$COCH$_3$	$23(2,22) \rightarrow 22(2,21)$ EE	238.868953	144.37	–	–	–	U
CH$_3$COCH$_3$	$23(1,22) \rightarrow 22(1,21)$ EE	238.868953	144.37	–	–	–	U
CH$_3$COCH$_3$	$23(2,22) \rightarrow 22(1,21)$ EE	238.868953	144.37	–	–	–	U
CH$_3$OH	$29(3) \rightarrow 29(2)$ A^{-+}	238.890424	1058.72	5.63	-53.9	6.3	B
CH$_3$COCH$_3$	$23(2,22) \rightarrow 22(2,21)$ AA	238.890805	144.29	–	-53.4	–	B
CH$_3$COCH$_3$	$23(1,22) \rightarrow 22(1,21)$ AA	238.890805	144.29	–	-53.4	–	B
CH$_3$CN	$13(7) \rightarrow 12(7)$	238.912715	430.10	22.72	-52.1	6.7	D
CH$_3$^{13}CN	$13(4) \rightarrow 12(4)$	238.946305	194.58	5.45	-54.3	6.7	B
CH$_3$OCHO	$19(3,16) \rightarrow 18(3,15)$ E v$_t$=1	238.947229	308.63	–	-53.1	–	B
CH$_3$CN	$13(6) \rightarrow 12(6)$	238.972389	337.37	65.57	-52.1	6.7	D
CH$_3$^{13}CN	$13(3) \rightarrow 12(3)$	238.978371	144.59	8.34	-51.9	6.7	U
SO$_2$	$21(7,15) \rightarrow 22(6,16)$	238.992534	332.51	56.85	-51.4	6.7	R
CH$_3$^{13}CN	$13(2) \rightarrow 12(2)$	239.001283	108.88	8.46	-51.6	6.7	U
CH$_3$^{13}CN	$13(1) \rightarrow 12(1)$	239.015035	87.45	8.27	-52.3	6.7	U
CH$_3$^{13}CN	$13(0) \rightarrow 12(0)$	239.019619	80.30	–	-46.6	–	U
CH$_3$CN	$13(5) \rightarrow 12(5)$	239.022924	258.87	67.35	-51.9	6.7	D
CH$_3$CN	$13(4) \rightarrow 12(4)$	239.064299	194.62	84.97	-52.3	6.3	D
?	–	239.123400	–	5.01	–	6.7	D
CH$_3$CN[b]	**$13(3) \rightarrow 12(3)$**	**239.096497**	**144.63**	**153.81**	**-52.3**	**5.9**	**D**
CH$_3$CN	$13(2) \rightarrow 12(2)$	239.119504	108.92	131.93	-52.3	5.9	D
CH$_3$CN	$13(1) \rightarrow 12(1)$	239.133313	87.49	169.74	-53.7	6.7	D
CH$_3$CN	$13(0) \rightarrow 12(0)$	239.137916	80.34	122.78	-53.3	3.9	D
CH$_3$CCH	$14(3) \rightarrow 13(3)$	239.211216	150.92	13.91	-53.0	3.3	O
CH$_3$CCH	$14(2) \rightarrow 13(2)$	239.234011	114.92	13.21	-53.0	2.6	O
CH$_3$CCH	$14(1) \rightarrow 13(1)$	239.247727	93.32	13.97	-53.2	2.6	O
CH$_3$CCH	$14(0) \rightarrow 13(0)$	239.252297	86.12	14.92	-53.0	2.5	O

NOTE—When a line is unidentified, indicated by a ? in the Species column, the measured line frequency is given instead of the rest frequency. An em-dash (–) shown in the flux, velocity and linewidth columns indicates that the line identification and measured properties are shared with the last line where the properties are stated. If the transition quantum numbers are not known, a reference is given instead.

[a] The morphology column sorts the lines into five different morphologies. These are, B: blue-dominant, D: disk-tracing, O: Outflow-tracing, R: red-dominant, and U: unknown.

[b] Lines whose moment maps are shown in Fig. 10 are shown in bold

Table A.2. Lines detected in the second ALMA narrow spectral window (spw3) covering 256.1146 to 256.5834 GHz

Species	Transition $J(K_a,K_c)$	Rest Freq. (GHz)	E_{up} (K)	Flux (mJy beam^{-1})	v (km s^{-1})	v_{FWHM} (km s^{-1})	Line Morph.[a]
CH$_3$OCHO	21(15,7) → 20(15,6) E v$_t$=1	256.071907	473.45	3.06	-53.2	5.4	D
HCOCH$_2$OH?	33(3,30) → 33(3,31) v=2	256.123418	686.70	0.37	-52.3	7.8	U
CH$_3$OCH$_3$	19(5,14) → 19(4,15) EE	256.137423	208.33	14.24	-52.9	6.2	B
^{13}CH$_3$OH	6(1,5) → 5(2,3) E	256.171587	68.63	17.95	-53.6	2.6	B
CH$_3$OCH$_3$	29(4,25) → 29(3,26) EE	256.193781	419.59	4.55	-53.1	4.6	B
C$_2$H$_5$OH	15(2,14) → 14(2,13) g$^+$	256.206340	160.74	9.40	-53.8	3.7	B
aGg'-(CH$_2$OH)$_2$	25(6,19) v=0 → 24(6,18) v=1	256.216551	178.92	3.83	-51.2	7.7	B
CH$_3$COCH$_3$	23(4,20) → 22(4,19) EA	256.213507	161.92	–	-54.7	–	B
CH$_3$COCH$_3$	23(3,20) → 22(3,19) EA	256.213507	161.92	–	-54.7	–	B
CH$_3$OH	17(3,15) → 17(2,16) A^{+-}	256.228714	404.80	123.62	-52.8	4.4	B
SO$_2$	5(3,3) → 5(2,4)	256.246945	35.89	182.00	-51.7	6.2	R
CH$_3$CCH	15(4) → 14(4)	256.258435	213.61	23.53	-52.4	7.8	D
CH$_3$COCH$_3$	23(3,20) → 22(4,19) EE	256.259007	161.87	–	-51.7	–	D
CH$_3$COCH$_3$	23(3,20) → 22(3,19) EE	256.259007	161.87	–	-51.7	–	D
CH$_3$COCH$_3$	23(4,20) → 22(4,19) EE	256.259007	161.87	–	-51.7	–	D
CH$_3$COCH$_3$	23(4,20) → 22(3,19) EE	256.259007	161.87	–	-51.7	–	D
HC$_3$N	28 → 27 l=0 v$_7$=2	256.259616	820.06	–	-51.0	–	D
CH$_3$CCH	15(3) → 14(3)	256.292638	163.22	12.80	-53.1	3.1	O
C$_2$H$_5$OH	15(2,14) → 14(2,13) g$^-$	256.307331	165.41	21.71	-54.7	7.7	D
CH$_3$OCHO?	McMillan et al. (2016)	256.309575	–	–	-52.1	–	D
HC$_3$N	28 → 27 l=2e v$_7$=2	256.311440	823.35	–	-49.9	–	D
CH$_3$CCH	15(2) → 14(2)	256.317078	127.22	9.92	-52.5	4.7	O
CH$_3$CCH	15(1) → 14(1)	256.331746	105.62	12.75	-53.1	2.6	O
CH$_3$CCH	15(0) → 14(0)	256.336636	105.62	13.76	-53.0	2.4	O
^{13}CH$_3$OH	13(3,11) → 13(2,12) A^{+-}	256.351482	256.14	28.11	-53.5	3.3	B
HC$_3$N	28 → 27 l=2f v$_7$=2	256.365922	823.37	15.81	-51.4	7.8	D
aGg'-(CH$_2$OH)$_2$?	26(1,25) v=1 → 25(1,24) v=0	256.379254	167.28	3.41	-51.0	7.8	U
C$_2$H$_3$CN[b]	**27(7,20) → 26(7,19)**	**256.397408**	**278.02**	**7.17**	**-50.8**	**6.7**	**D**
CH$_3$OCHO	21(13,8) → 20(13,7) A v$_t$=1	256.403576	435.82	3.22	-56.3	7.8	U
CH$_3$OCHO	21(13,9) → 20(13,8) A v$_t$=1	256.403576	435.82	–	–	–	U
C$_2$H$_3$CN	27(8,19) → 26(8,18)	256.409287	310.30	–	-49.6	–	U
C$_2$H$_3$CN	27(8,20) → 26(8,19)	256.409287	310.30	–	-49.6	–	U
C$_2$H$_3$CN	27(6,21) → 26(6,20)	256.426112	250.01	4.40	-51.9	7.8	D
C$_2$H$_3$CN	27(9,18) → 26(9,17)	256.448018	326.82	5.02	-52.6	6.0	D
C$_2$H$_3$CN	27(9,19) → 26(9,18)	256.448018	326.82	–	–	–	D
CH$_3$OCHO	21(10,11) → 20(10,10) E v$_t$=1	256.501348	390.07	3.24	-54.6	5.7	U
CH$_3$OCHO	21(12,9) → 20(12,8) A v$_t$=1	256.506751	419.12	3.72	-53.7	3.0	U
CH$_3$OCHO	21(12,10) → 20(12,9) A v$_t$=1	256.506751	419.12	–	–	–	U
C$_2$H$_3$CN	27(5,23) → 26(5,22)	256.523007	226.30	3.99	-54.5	7.7	D

Table A.2 *continued*

Table A.2 *(continued)*

Species	Transition	Rest Freq.	E_{up}	Flux	v	v_{FWHM}	Line
	$J(K_a,K_c)$	(GHz)	(K)	(mJy beam^{-1})	(km s^{-1})	(km s^{-1})	Morph.[a]
C_2H_3CN	$27(5,22) \rightarrow 26(5,21)$	256.527505	226.30	–	-49.2	–	D

Note—When a line is unidentified, indicated by a ? in the Species column, the measured line frequency is given instead of the rest frequency. An em-dash (–) shown in the flux, velocity and linewidth columns indicates that the line identification and measured properties are shared with the last line where the properties are stated. If the transition quantum numbers are not known, a reference is given instead.

[a]The morphology column sorts the lines into five different morphologies. These are, B: blue-dominant, D: disk-tracing, O: Outflow-tracing, R: red-dominant, and U: unknown.

[b]Lines whose moment maps are shown in Fig. 10 are shown in bold

Table A.3. Lines detected in the first wide spectral window (spw1) covering 239.6035 to 241.4785 GHz

Species	Transition	Rest Freq.	E_{up}	Flux	v	v_{FWHM}	Line
	$J(K_a,K_c)$	(GHz)	(K)	(mJy beam^{-1})	(km s^{-1})	(km s^{-1})	Morph.[a]
$H^{13}CCCN$	$27 \rightarrow 26$ l=2f v_7=2	239.571308	800.34	1.40	-51.6	12.5	U
aGg'-$(CH_2OH)_2$	$24(11,13)$ v=0 $\rightarrow$ $23(11,12)$ v=1	239.605334	206.93	3.56	-56.5	8.7	B
CH_3OCHO	$19(5,14) \rightarrow 18(5,13)$ A v_t=1	239.610154	317.09	–	-50.5	–	B
CH_3CN	$13(1) \rightarrow 12(1)$ l=+1 v_8=1	239.627369	599.52	14.38	-51.8	8.7	D
$HC(O)NH_2$	$11(1,10) \rightarrow 10(1,9)$ v_{12}=1	239.653472	487.98	2.57	-53.2	9.1	D
CH_3CN	$13(5) \rightarrow 12(5)$ l=-1 v_8=1	239.684649	850.61	10.87	-50.9	9.3	D
CH_3CN	$13(7) \rightarrow 12(7)$ l=+1 v_8=1	239.699313	862.28	4.27	-52.7	9.3	D
C_2H_3CN	$26(0,26) \rightarrow 25(0,25)$	239.708394	157.04	4.78	-50.3	7.4	D
CH_3OH	$16(7,10) \rightarrow 17(6,12)$ A$^-$	239.731363	560.07	47.59	-53.6	4.5	B
CH_3OH	$5(1,5) \rightarrow 4(1,4)$ A$^+$	239.746219	49.06	208.53	-52.5	4.5	B
CH_3CN	$13(3) \rightarrow 12(3)$ l=-1 v_8=1	239.777130	709.90	6.81	-52.6	8.8	D
aGg'-$(CH_2OH)_2$	$25(3,23)$ v=0 $\rightarrow$ $24(3,22)$ v=1	239.792798	161.62	7.20	-51.8	8.6	D
CH_3CN	$13(2) \rightarrow 12(2)$ l=-1 v_8=1	239.808835	660.92	17.25	-52.4	8.3	D
C_2H_3CN	$25(1,24) \rightarrow 24(1,23)$	239.816142	152.76	5.07	-54.1	13.3	U
CH_3CN	$13(4) \rightarrow 12(4)$ l=+1 v_8=1	239.824766	666.76	15.34	-57.6	11.6	D
SO_2	$15(3,13) \rightarrow 16(0,16)$	239.832754	132.54	23.40	-51.6	10.6	D
CH_3CN	$13(3) \rightarrow 12(3)$ l=+1 v_8=1	239.850003	630.10	11.71	-51.9	8.0	D
CH_3CN[b]	**$13(2) \rightarrow 12(2)$ l=+1 v_8=1**	**239.871650**	**607.71**	**12.57**	**-52.4**	**8.3**	**D**
aGg'-$(CH_2OH)_2$	$24(10,15)$ v=0 $\rightarrow$ $23(10,14)$ v=1	239.883541	196.68	3.40	-54.3	6.6	B
aGg'-$(CH_2OH)_2$	$24(10,14)$ v=0 $\rightarrow$ $23(10,13)$ v=1	239.883585	196.68	–	-54.3	–	B
CH_3OCHO?	$44(8,36) \rightarrow 44(7,37)$ E	239.927523	644.58	2.41	-50.5	6.3	U
$HC(O)NH_2$	$11(1,10) \rightarrow 10(1,9)$	239.951800	72.33	24.63	-52.7	8.0	D
aGg'-$(CH_2OH)_2$?	$25(2,23)$ v=0 $\rightarrow$ $24(2,22)$ v=1	239.957158	161.61	1.99	-53.2	8.7	U
CH_3OH	$27(3,24) \rightarrow 27(2,25)$ A^{-+}	239.977050	926.58	10.56	-53.3	5.0	B
aGg'-$(CH_2OH)_2$	$23(4,20)$ v=1 $\rightarrow$ $22(4,19)$ v=0	239.980039	144.08	–	-49.6	–	B
CH_3COCH_3	$24(1,24) \rightarrow 23(1,23)$ EA	239.984779	146.60	4.78	-47.7	13.3	U

Table A.3 *continued*

Table A.3 *(continued)*

Species	Transition J(K$_a$,K$_c$)	Rest Freq. (GHz)	E$_{up}$ (K)	Flux (mJy beam^{-1})	v (km s^{-1})	v$_{FWHM}$ (km s^{-1})	Line Morph.[a]
CH$_3$COCH$_3$	24(0,24) → 23(0,23) EA	239.984779	146.60	–	–	–	U
CH$_3$COCH$_3$	24(0,24) → 23(1,23) EE	239.991110	146.50	4.75	-54.0	7.5	U
CH$_3$COCH$_3$	24(1,24) → 23(1,23) EE	239.991110	146.50	–	–	–	U
CH$_3$COCH$_3$	24(0,24) → 23(0,23) EE	239.991110	146.50	–	–	–	U
CH$_3$COCH$_3$	24(1,24) → 23(0,23) EE	239.991110	146.50	–	–	–	U
CH$_3$COCH$_3$	24(0,24) → 23(1,23) AA	239.997383	146.40	3.10	-53.8	3.7	U
CH$_3$COCH$_3$	24(1,24) → 23(0,23) AA	239.997383	146.40	–	–	–	U
CH$_3$OCHO	19(3,16) → 18(3,15) E	240.021140	122.26	18.89	-53.5	3.3	B
CH$_3$OCHO	19(3,16) → 18(3,15) A	240.034673	122.25	19.63	-53.5	3.4	B
SO$_2$	11(5,7) → 12(4,8) v$_2$=1	240.057521	868.48	2.23	-50.8	9.3	U
CH$_3$CHO	23(8,16) → 24(7,18) E	240.057567	399.46	–	-50.7	–	U
CH$_3$CN	13(1) → 12(1) l=-1 v$_8$=1	240.089530	599.67	14.75	-52.5	7.8	D
C$_2$H$_5$OH	27(2,25) → 27(1,26) a	240.110242	327.24	1.78	-53.4	3.9	U
NH$_2$CN	12(3,10) → 11(3,9)	240.130645	205.25	2.33	-53.5	9.5	D
NH$_2$CN[b]	**12(3,9) → 11(3,8)**	**240.132690**	**205.25**	**–**	**-51.0**	**–**	**D**
aGg'-(CH$_2$OH)$_2$	24(3,21) v=0 → 23(3,20) v=1	240.147963	155.15	2.58	-56.9	10.0	U
OC^{33}S	20 → 19	240.155961	121.03	3.31	-53.5	3.3	B
H$_2$CS?	7(6,1) → 6(6,0)	240.179077	518.82	2.84	-48.2	13.3	U
H$_2$CS?	7(6,2) → 6(6,1)	240.179077	518.82	–	–	–	U
CH$_2$CO	12(1,12) → 11(1,11)	240.187257	88.01	28.21	-51.5	3.6	B
HNCO?	48(0,48) → 47(1,47)	240.201778	1239.46	1.45	-51.6	12.2	U
HCOCH$_2$OH	14(10,5) → 14(9,6)	240.219091	119.02	2.01	-54.4	7.7	U
CH$_3$OH	5(3,2) → 6(2,4) E	240.241490	82.53	122.85	-52.9	4.3	B
H$_2$CS	7(5,2) → 6(5,1)	240.261988	374.70	23.57	-56.8	10.2	B
H$_2$CS	7(5,3) → 6(5,2)	240.261988	374.70	–	–	–	B
H$_2$CS	7(0,7) → 6(0,6)	240.266872	46.14	49.90	-53.4	3.3	B
C$_2$H$_5$CN[b]	**28(1,28) → 27(1,27)**	**240.319337**	**169.27**	**4.80**	**-52.5**	**7.2**	**D**
H$_2$CS	7(4,4) → 6(4,3)	240.332190	256.59	18.70	-53.5	5.1	B
H$_2$CS	7(4,3) → 6(4,2)	240.332190	256.59	–	–	–	B
H$_2$CS	7(2,6) → 6(2,5)	240.382051	98.82	44.19	-53.4	4.5	B
H$_2$CS	7(3,4) → 6(3,3)	240.393762	164.60	93.89	-52.5	4.7	B
CH$_3$OCHO	41(9,33) → 41(8,34) A	240.400935	568.58	3.75	-49.7	8.4	U
CH$_3$OCHO?	36(10,27) → 36(9,28) E	240.417922	462.48	2.39	-57.2	12.3	D
C$_2$H$_5$CN	28(0,28) → 27(0,27)	240.429184	169.24	4.53	-52.7	6.9	D
C$_2$H$_5$OH	26(3,24) → 26(2,25) a	240.450946	305.41	2.34	-53.8	13.3	U
CH$_3$OH	5(1,5) → 4(1,4) A$^+$ v$_t$ = 2	240.454848	717.41	11.31	-54.0	4.7	B
H$_2$CS?	21(1,20) → 21(1,21)	240.518081	399.25	2.65	-52.3	13.3	U
H$_2$CS	7(2,5) → 6(2,4)	240.549066	98.83	44.16	-53.3	4.3	B
HCOCH$_2$OH?	11(10,1) → 11(9,2)	240.572978	97.38	2.65	-54.7	13.2	U
^{33}SO$_2$	10(3,7) → 10(2,8)	240.611132	72.27	8.12	-52.2	7.9	D

Table A.3 *continued*

Table A.3 *(continued)*

Species	Transition $J(K_a, K_c)$	Rest Freq. (GHz)	E_{up} (K)	Flux (mJy beam^{-1})	v (km s^{-1})	v_{FWHM} (km s^{-1})	Line Morph.[a]
CH$_3$CHO	12(2,11) → 11(2,10) E v$_t$=2	240.652038	462.31	3.65	-54.8	6.6	B
C$_2$H$_5$OH	4(2,2) g$^-$ → 3(1,2) g$^+$	240.653983	74.79	–	-52.4	–	B
?	–	240.744900	–	2.88	–	4.5	B
HC(O)NH$_2$	9(3,6) → 10(1,9) v$_{12}$=1	240.718643	488.03	2.58	-51.9	8.7	U
CH$_3$OH	26(3,23) → 26(2,24) A^{-+}	240.738926	863.98	18.13	-53.9	5.2	B
aGg'-(CH$_2$OH)$_2$	50(13,38) v=1 → 50(12,38) v=0	240.753385	711.82	2.60	-56.1	11.1	U
CH$_3$OH	5(2,3) → 4(2,2) A$^-$ v$_t$ = 2	240.757920	911.34	4.66	-53.5	4.0	B
aGg'-(CH$_2$OH)$_2$	25(1,25) v=1 → 24(1,24) v=0	240.778125	148.00	6.51	-54.9	10.3	D
aGg'-(CH$_2$OH)$_2$	24(8,17) v=0 → 23(8,16) v=1	240.807880	179.25	2.24	-56.1	9.2	B
CH$_3$OH	5(1,4) → 4(1,3) E v$_t$ = 2	240.817972	833.64	4.41	-53.8	4.1	B
aGg'-(CH$_2$OH)$_2$	24(8,16) v=0 → 23(8,15) v=1	240.828886	179.25	1.29	-55.8	13.2	B
C$_2$H$_5$OH	14(1,13) g$^+$ → 13(0,13) g$^-$	240.838747	147.10	11.00	-53.7	3.8	B
CH$_3$OH	5(-4,2) → 4(-4,1) E v$_t$ = 2	240.861406	779.22	2.39	-55.2	13.2	B
HNCO[b]	**11(1,11) → 10(1,10)**	**240.875777**	**112.64**	**66.54**	**-51.9**	**8.0**	**D**
CH$_3$OH	5(3,3) → 4(3,2) A$^-$ v$_t$ = 2	240.916172	692.78	17.85	-53.7	4.5	B
CH$_3$OH	5(3,2) → 4(3,1) A$^+$ v$_t$ = 2	240.916173	692.78	–	-53.7	–	B
CH$_3$OH	5(4,1) → 4(4,0) A$^+$ v$_t$ = 2	240.932051	649.19	17.10	-53.8	4.2	B
CH$_3$OH	5(4,2) → 4(4,1) A$^-$ v$_t$ = 2	240.932051	649.19	–	–	–	B
SO$_2$	18(1,17) → 18(0,18)	240.942792	163.07	191.50	-51.0	7.0	R
CH$_3$OH	5(2,4) → 4(2,3) E v$_t$ = 2	240.952056	620.93	22.12	-50.9	10.3	B
CH$_3$OH	5(1,5) → 4(1,4) A$^+$ v$_t$ = 1	240.960557	359.95	97.83	-52.7	4.8	B
C$_2$H$_3$CN	35(7,29) → 36(6,30)	240.978552	392.88	2.55	-54.8	10.2	U
CH$_3$OCH$_3$	5(3,3) → 4(2,2) EE	240.985078	26.31	15.03	-53.4	3.6	B
HCOCH$_2$OH	28(6,22) → 27(7,21) v=2	240.989945	626.66	6.48	-53.4	3.3	B
CH$_3$COCH$_3$	12(12,1) → 11(11,1) EE	240.998755	74.49	2.94	-55.1	13.2	B
C^{34}S	5 → 4	241.016194	34.70	109.64	-52.7	5.8	O
CH$_3$OCHO	33(10,23) → 33(9,24) E	241.036087	399.46	1.49	-55.8	13.2	U
CH$_3$OH	22(-6,16) → 23(-5,18) E	241.042589	775.57	8.41	-54.2	5.1	B
CH$_3$OH	9(3,7) → 10(0,10) E	241.057109	152.17	1.96	-54.9	13.2	B
CH$_3$COCH$_3$	12(12,0) → 11(11,0) EE	241.062732	74.61	1.33	-54.0	13.2	B
?	–	241.144500	–	1.69	–	9.9	B
HCOCH$_2$OH	22(2,20) → 21(3,19)	241.131839	142.80	2.98	-53.2	13.2	U
HCOOH[b]	**11(0,11) → 10(0,10)**	**241.146330**	**70.19**	**15.88**	**-52.1**	**8.2**	**D**
CH$_3$OH	5(4,2) → 4(4,1) E v$_t$ = 1	241.159199	398.11	41.13	-53.5	4.5	B
CH$_3$OH	5(3,2) → 4(3,1) E v$_t$ = 1	241.166580	452.14	48.24	-53.3	4.2	B
CH$_3$OH	5(-3,3) → 4(-3,2) E v$_t$ = 1	241.179886	357.36	84.30	-52.7	4.8	B
CH$_3$OH	5(-2,4) → 4(-2,3) E v$_t$ = 1	241.187428	399.34	69.80	-52.7	7.5	B
CH$_3$OH	5(2,4) → 4(2,3) A$^+$ v$_t$ = 1	241.192856	333.40	77.20	-52.9	2.9	B
CH$_3$OH	5(2,3) → 4(2,2) A$^-$ v$_t$ = 1	241.196430	333.40	117.60	-53.5	6.5	B
CH$_3$OH	5(1,5) → 4(1,4) E v$_t$ = 1	241.203706	326.20	126.20	-54.2	6.9	B

Table A.3 *continued*

Table A.3 *(continued)*

Species	Transition J(K_a,K_c)	Rest Freq. (GHz)	E_{up} (K)	Flux (mJy beam^{-1})	v (km s^{-1})	v_{FWHM} (km s^{-1})	Line Morph.[a]
CH$_3$OH	5(0,5) → 4(0,4) E v_t = 1	241.206035	335.31	–	-51.3	–	B
CH$_3$OH	5(2,3) → 4(2,2) E v_t = 1	241.210764	434.63	63.20	-53.5	3.7	B
CH$_3$OH	5(-1,4) → 4(-1,3) E v_t = 1	241.238144	448.11	63.72	-53.4	4.2	B
CH$_3$OH	5(0,5) → 4(0,4) A$^+$ v_t = 1	241.267862	458.39	61.57	-53.3	4.1	B
CH$_3$COCH$_3$	12(12,1) → 11(11,0) AA	241.286250	74.53	1.19	-53.5	13.2	U
aGg'-(CH$_2$OH)$_2$	24(5,20) v=0 → 23(5,19) v=1	241.291269	160.66	2.22	-53.6	13.2	U
H$_2$CCN	12(0,12) → 11(0,11) J=25/2 → 23/2	241.333542	75.30	1.98	-51.8	13.2	U
CH$_3$OH	5(1,4) → 4(1,3) A$^-$ v_t = 2	241.364143	717.54	12.09	-53.7	4.3	B
H$_2$CCN	12(2,11) → 11(2,10) J=25/2 → 23/2	241.391395	128.09	1.91	-49.5	8.2	U

Note—When a line is unidentified, indicated by a ? in the Species column, the measured line frequency is given instead of the rest frequency. An em-dash (–) shown in the flux, velocity and linewidth columns indicates that the line identification and measured properties are shared with the last line where the properties are stated. If the transition quantum numbers are not known, a reference is given instead.

[a] The morphology column sorts the lines into five different morphologies. These are, B: blue-dominant, D: disk-tracing, O: Outflow-tracing, R: red-dominant, and U: unknown.

[b] Lines whose moment maps are shown in Fig. 10 are shown in bold

Table A.4. Lines detected in the second wide spectral window (spw2) covering 253.1055 to 254.9805 GHz

Species	Transition J(K_a,K_c)	Rest Freq. (GHz)	E_{up} (K)	Flux (mJy beam^{-1})	v (km s^{-1})	v_{FWHM} (km s^{-1})	Line Morph.[a]
HC(O)NH$_2$	12(2,11) → 11(2,10)	253.165793	91.10	24.18	-52.8	7.7	D
^{34}SO	$^3\Sigma$ N,J = 6,6 → 5,5	253.207017	55.69	106.61	-51.5	6.2	R
CH$_3$OH	13(3,11) → 13(2,12) A^{+-}	253.221376	260.99	192.46	-52.5	4.3	B
^{13}CH$_3$OH	14(3,11) → 14(2,12) A^{-+}	253.310162	287.84	25.93	-53.6	3.3	B
aGg'-(CH$_2$OH)$_2$	24(9,16) v=1 → 23(9,15) v=0	253.314615	187.76	3.61	-54.9	6.0	U
aGg'-(CH$_2$OH)$_2$	24(9,15) v=1 → 23(9,14) v=0	253.315874	187.76	–	-53.4	–	U
SO^{18}O	14(1,14) → 13(0,13)	253.497415	89.36	5.25	-51.4	5.5	R
NS[b]	$^2\Pi_{1/2}$ N,J,F,P = 6,5.5,6.5,-1 → 5,4.5,5.5,1	**253.570476**	**38.70**	**46.77**	**-53.1**	**8.0**	**D**
NS[b]	$^2\Pi_{1/2}$ N,J,F,P = 6,5.5,5.5,-1 → 5,4.5,4.5,1	**253.570476**	**38.70**	–	–	–	**D**
CH$_3$OCHO	17(4,14) → 16(3,13) E	253.606166	101.43	2.71	-53.1	3.6	B
aGg'-(CH$_2$OH)$_2$	25(3,23) v=1 → 24(3,22) v=0	253.616767	161.96	15.22	-52.0	7.2	D
HC^{13}CCN	28 → 27	253.619052	176.51	–	-49.3	–	D
HCC^{13}CN	28 → 27	253.643519	176.52	11.75	-51.2	7.8	D
^{13}CH$_3$OH	13(3,10) → 13(2,11) A^{-+}	253.689530	256.15	34.52	-53.6	3.2	B
C$_2$H$_5$OH	15(2,13) g$^-$ → 14(3,11) g$^+$	253.697863	167.90	2.77	-53.3	3.8	B
CH$_3$OCHO	20(5,15) → 19(5,14) A v_t=1	253.743207	329.27	2.49	-54.7	12.6	B
CH$_3$OH	14(3,12) → 14(2,13) A^{+-}	253.755809	293.47	190.72	-52.5	4.4	B
CH$_3$OCHO	21(4,18) → 20(4,17) A v_t=1	253.807849	333.90	4.00	-51.3	7.3	B

Table A.4 *continued*

Table A.4 (continued)

Species	Transition J(K$_a$,K$_c$)	Rest Freq. (GHz)	E$_{up}$ (K)	Flux (mJy beam^{-1})	v (km s^{-1})	v$_{FWHM}$ (km s^{-1})	Line Morph.[a]
aGg'-(CH$_2$OH)$_2$	24(8,16) v=1 → 23(8,15) v=0	253.856295	179.56	2.26	-54.9	5.1	B
aGg'-(CH$_2$OH)$_2$	24(3,21) v=1 → 23(3,20) v=0	253.883009	155.53	3.85	-55.2	6.5	B
CH$_3$OCH$_3$	20(5,15) → 20(4,16) EE	253.906820	226.60	14.81	-53.2	5.3	B
^{34}SO$_2$	11(3,9) → 11(2,10)	253.936317	81.93	55.87	-51.3	6.9	R
SO$_2$	15(6,10) → 16(5,11)	253.956570	198.60	86.01	-51.4	6.6	R
NS	$^2\Pi_{1/2}$ N,J,F,P = 6,5.5,5.5,1 → 5,4.5,4.5,-1	253.970581	38.82	44.72	-51.5	8.7	D
NS	$^2\Pi_{1/2}$ N,J,F,P = 6,5.5,4.5,1 → 5,4.5,3.5,-1	253.970581	38.82	–	–	–	D
aGg'-(CH$_2$OH)$_2$	24(6,18) → 23(6,18)	253.981324	166.26	4.00	-52.6	6.0	D
^{33}SO$_2$	30(4,26) → 30(3,27)	253.982600	470.68	–	-51.1	–	D
CH$_3$OH	2(0,2) → 1(-1,1) E	254.015377	20.09	126.43	-52.5	5.1	B
^{13}CH$_3$OH	12(3,9) → 12(2,10) A^{-+}	254.012582	226.71	–	-55.8	–	B
SO^{18}O	10(3,8) → 10(2,9)	254.066539	69.37	2.65	-50.9	6.0	U
CH$_3$COCH$_3$	21(6,16) → 20(5,15) EE	254.082229	151.84	3.99	-52.3	6.9	D
C$_2$H$_3$CN	27(2,26) → 26(2,25)	254.137460	180.05	3.41	-51.2	7.3	D
SO$_2$?	41(11,31) → 42(10,32)	254.194875	1087.68	2.26	-54.0	12.1	R
aGg'-(CH$_2$OH)$_2$	28(1,28) v=0 → 27(1,27) v=1	254.208718	183.96	5.83	-55.9	8.9	B
aGg'-(CH$_2$OH)$_2$?	29(13,17) v=1 → 29(12,18) v=1	254.217765	297.15	2.58	-54.8	6.9	U
CH$_3$COCH$_3$	37(8,29) → 37(7,30) AE	254.233997	448.79	3.33	-52.0	7.9	B
CH$_3$COCH$_3$	37(9,29) → 37(8,30) AE	254.233997	448.79	–	–	–	B
SO$_2$	6(3,3) → 6(2,4)	254.280536	41.40	242.40	-52.9	9.0	R
^{13}CH$_3$OH	4(2,2) → 5(1,5) A$^+$	254.321721	60.46	14.57	-53.6	3.1	B
?	–	254.389800	–	2.10	–	8.5	B
C$_2$H$_5$OH?	7(3,4) → 6(2,5) a	254.384085	34.84	9.37	-53.4	4.6	B
CH$_3$OCHO	21(4,18) → 20(4,17) E v$_t$=1	254.391288	333.63	2.82	-53.4	3.1	B
CH$_3$OH	11(5,7) → 12(4,8) E	254.419419	289.23	119.98	-53.8	4.9	B
CH$_3$OH	15(3,13) → 15(2,14) A^{+-}	254.423520	328.26	156.62	-53.1	3.6	B
^{13}CH$_3$OH	10(3,7) → 10(2,8) A^{-+}	254.509364	174.63	55.28	-53.4	3.6	B
^{33}SO$_2$	9(3,7) → 9(2,8)	254.509400	63.04	–	-53.4	–	B
^{34}SO$_2$	14(6,8) → 15(5,11)	254.516776	181.58	5.14	-50.3	12.5	U
CH$_3$OCHO	20(5,15) → 19(5,14) E v$_t$=1	254.530213	329.14	3.33	-53.9	5.0	B
O^{13}CS	21 → 20	254.552731	134.39	8.35	-52.8	5.0	B
SO	$^3\Sigma$ N,J = 8,9 → 8,8	254.573628	99.70	60.39	-51.3	6.7	R
^{13}CH$_3$OH?	19(3,17) → 18(4,14) A$^+$	254.586974	420.20	2.60	-51.7	6.0	U
?	–	254.710400	–	1.82	–	12.5	U
CH$_3$CCNC?	58(3) → 57(3)	254.670887	427.53	2.18	-51.7	3.1	B
CH$_2$NH?	4(0,4) → 3(0,3)	254.685200	30.62	14.90	-53.4	4.8	B
^{13}CH$_3$OH	9(3,6) → 9(2,7) A^{-+}	254.693481	151.98	69.60	-53.7	3.5	B
HC$_3$N[b]	**28 → 27**	**254.699500**	**177.26**	**149.40**	**-52.1**	**6.3**	**D**
?	–	254.759300	–	7.35	–	12.5	D
HC(O)NH$_2$	12(9,3) → 11(9,2)	254.727017	320.46	16.68	-53.4	8.2	D

Table A.4 continued

Table A.4 *(continued)*

Species	Transition J(K$_a$,K$_c$)	Rest Freq. (GHz)	E$_{up}$ (K)	Flux (mJy beam^{-1})	v (km s^{-1})	v$_{\mathrm{FWHM}}$ (km s^{-1})	Line Morph.[a]
HC(O)NH$_2$	12(9,4) → 11(9,3)	254.727017	320.46	–	–	–	D
HC(O)NH$_2$	12(10,2) → 11(10,1)	254.737874	376.87	2.23	-53.4	6.3	D
HC(O)NH$_2$	12(10,3) → 11(10,2)	254.737874	376.87	–	–	–	D
HC(O)NH$_2$	12(7,5) → 11(7,4)	254.743840	225.35	18.48	-53.0	8.3	D
HC(O)NH$_2$	12(7,6) → 11(7,5)	254.743840	225.35	–	–	–	D
HC(O)NH$_2$	12(11,1) → 11(11,0)	254.757032	439.17	1.79	-55.0	8.3	U
HC(O)NH$_2$	12(11,2) → 11(11,1)	254.757032	439.17	–	–	–	U
HC(O)NH$_2$	12(6,7) → 11(6,6)	254.786445	186.68	22.28	-53.0	7.8	D
HC(O)NH$_2$	12(6,6) → 11(6,5)	254.786445	186.68	–	–	–	D
CH$_3$CHO	13(2,11) → 12(2,10) E	254.827152	94.09	10.14	-53.3	4.3	B
^{13}CH$_3$OH	8(3,5) → 8(2,6) A^{-+}	254.841818	131.59	59.55	-53.6	3.2	B
CH$_3$CHO	13(2,11) → 12(2,10) A	254.850487	94.07	10.10	-53.2	6.7	B
?	–	254.903400	–	4.30	–	12.5	B
HC(O)NH$_2$[b]	**12(5,8) → 11(5,7)**	**254.876330**	**153.95**	**28.62**	**-52.8**	**8.3**	**D**
HC(O)NH$_2$	12(5,7) → 11(5,6)	254.876647	153.95	–	-52.4	–	D

Note—When a line is unidentified, indicated by a ? in the Species column, the measured line frequency is given instead of the rest frequency. An em-dash (–) shown in the flux, velocity and linewidth columns indicates that the line identification and measured properties are shared with the last line where the properties are stated. If the transition quantum numbers are not known, a reference is given instead.

[a]The morphology column sorts the lines into five different morphologies. These are, B: blue-dominant, D: disk-tracing, O: Outflow-tracing, R: red-dominant, and U: unknown.

[b]Lines whose moment maps are shown in Fig. 10 are shown in bold

Table A.5. Line databases used for line identification and summary of identified lines.

Species	Line Database	Molecule Tag	Number of Lines Identified					
			B	D	R	O	U	Total
HCOOH	JPL	46005	$\cdots$	1(0)	$\cdots$	$\cdots$	$\cdots$	1(0)
CH$_2$CO	JPL	42002	1(0)	$\cdots$	$\cdots$	$\cdots$	$\cdots$	1(0)
CH$_3$OH v$_t$ = 0,1,2	JPL	32003	27(6)	$\cdots$	$\cdots$	$\cdots$	$\cdots$	27(6)
^{13}CH$_3$OH	CDMS	33502	7(2)	$\cdots$	$\cdots$	$\cdots$	1(0)	8(2)
CH$_3$CHO	JPL	44003	2(1)	$\cdots$	$\cdots$	$\cdots$	0(1)	2(2)
CH$_3$OCHO	JPL	60003	7(2)	2(1)	$\cdots$	$\cdots$	4(2)	13(5)
HCOCH$_2$OH	JPL	60006	1(0)	$\cdots$	$\cdots$	$\cdots$	4(0)	5(0)
C$_2$H$_5$OH	CDMS	46524	4(1)	0(1)	$\cdots$	$\cdots$	2(0)	6(2)
CH$_3$OCH$_3$	JPL	46008	4(0)	$\cdots$	$\cdots$	$\cdots$	$\cdots$	4(0)
CH$_3$COCH$_3$	JPL	58003	2(3)	1(1)	$\cdots$	$\cdots$	1(4)	4(8)
aGg'(CH$_2$OH)$_2$	CDMS	62503	5(4)	2(2)	$\cdots$	$\cdots$	6(1)	13(7)
HC$_3$N	CDMS	51501	$\cdots$	1(0)	$\cdots$	$\cdots$	$\cdots$	1(0)

Table A.5 *continued*

Table A.5 *(continued)*

Species	Line Database	Molecule Tag	Number of Lines Identified					
			B	D	R	O	U	Total
HC_3N $v_7 = 2$	CDMS	51503	$\cdots$	1(2)	$\cdots$	$\cdots$	$\cdots$	1(2)
$H^{13}CCCN$ $v_7 = 2$	CDMS	52518	$\cdots$	$\cdots$	$\cdots$	$\cdots$	1(0)	1(0)
$HC^{13}CCN$	CDMS	52510	$\cdots$	0(1)	$\cdots$	$\cdots$	$\cdots$	0(1)
$HCC^{13}CN$	CDMS	52511	$\cdots$	1(0)	$\cdots$	$\cdots$	$\cdots$	1(0)
H_2CCN	CDMS	40505	$\cdots$	$\cdots$	$\cdots$	$\cdots$	2(0)	2(0)
NH_2CN	JPL	42003	$\cdots$	0(1)	$\cdots$	$\cdots$	$\cdots$	0(1)
CH_3CN	JPL	41001	$\cdots$	9(0)	$\cdots$	$\cdots$	$\cdots$	9(0)
$CH_3^{13}CN$	JPL	42007	0(1)	$\cdots$	$\cdots$	$\cdots$	2(1)	2(2)
CH_3CN $v_8 = 1$	CDMS	41509	$\cdots$	9(0)	$\cdots$	$\cdots$	$\cdots$	9(0)
C_2H_3CN	CDMS	53515	$\cdots$	4(2)	$\cdots$	$\cdots$	2(1)	6(3)
C_2H_5CN	CDMS	55502	$\cdots$	2(0)	$\cdots$	$\cdots$	$\cdots$	2(0)
CH_3CCNC^a	CDMS	65505	1(0)	$\cdots$	$\cdots$	$\cdots$	$\cdots$	1(0)
NS	CDMS	46515	$\cdots$	0(2)	$\cdots$	$\cdots$	$\cdots$	0(2)
HNCO	JPL	43002	$\cdots$	1(0)	$\cdots$	$\cdots$	1(0)	2(0)
$HC(O)NH_2$	CDMS	45512	$\cdots$	2(5)	$\cdots$	$\cdots$	0(1)	2(6)
$HC(O)NH_2$ $v_{12} = 1$	CDMS	45516	$\cdots$	1(0)	$\cdots$	$\cdots$	1(0)	2(0)
$C^{34}S$	JPL	46001	$\cdots$	$\cdots$	$\cdots$	1(0)	$\cdots$	1(0)
H_2CS	CDMS	46509	4(2)	$\cdots$	$\cdots$	$\cdots$	1(1)	5(3)
SO	JPL	48501	$\cdots$	$\cdots$	1(0)	$\cdots$	$\cdots$	1(0)
^{34}SO	JPL	50001	$\cdots$	$\cdots$	1(0)	$\cdots$	$\cdots$	1(0)
SO_2	CDMS	64502	$\cdots$	1(0)	6(0)	$\cdots$	$\cdots$	7(0)
$^{33}SO_2$	CDMS	65501	0(1)	1(1)	$\cdots$	$\cdots$	$\cdots$	1(2)
$^{34}SO_2$	JPL	66002	$\cdots$	$\cdots$	1(0)	$\cdots$	1(0)	2(0)
SO_2 $v_2 = 1$	CDMS	64503	$\cdots$	$\cdots$	$\cdots$	$\cdots$	0(1)	0(1)
$SO^{18}O_2$	CDMS	66502	$\cdots$	$\cdots$	1(0)	$\cdots$	1(0)	2(0)
$O^{13}CS$	CDMS	61502	1(0)	$\cdots$	$\cdots$	$\cdots$	$\cdots$	1(0)
$OC^{33}S$	CDMS	61503	1(0)	$\cdots$	$\cdots$	$\cdots$	$\cdots$	1(0)
CH_3CCH	JPL	40001	$\cdots$	0(1)	$\cdots$	8(0)	$\cdots$	8(1)
CH_2NH^a	JPL	29003	1(0)	$\cdots$	$\cdots$	$\cdots$	$\cdots$	1(0)
?	$\cdots$	$\cdots$	4(0)	2(0)	$\cdots$	$\cdots$	1(0)	7(0)

NOTE—The number of lines identified for each species and morphology type (Blue-dominant, Disk-tracing, Red-dominant, Outflow-tracing, and Unknown) are given in the penultimate five columns, along with the total number of lines for that species in the final column. The numbers in parentheses give the number of ambiguous line identifications. The final row lists unidentified lines, which are indicated by a question mark in the first column of Tables A.1 to A.4.

^{a}These species have only tentative identifications.
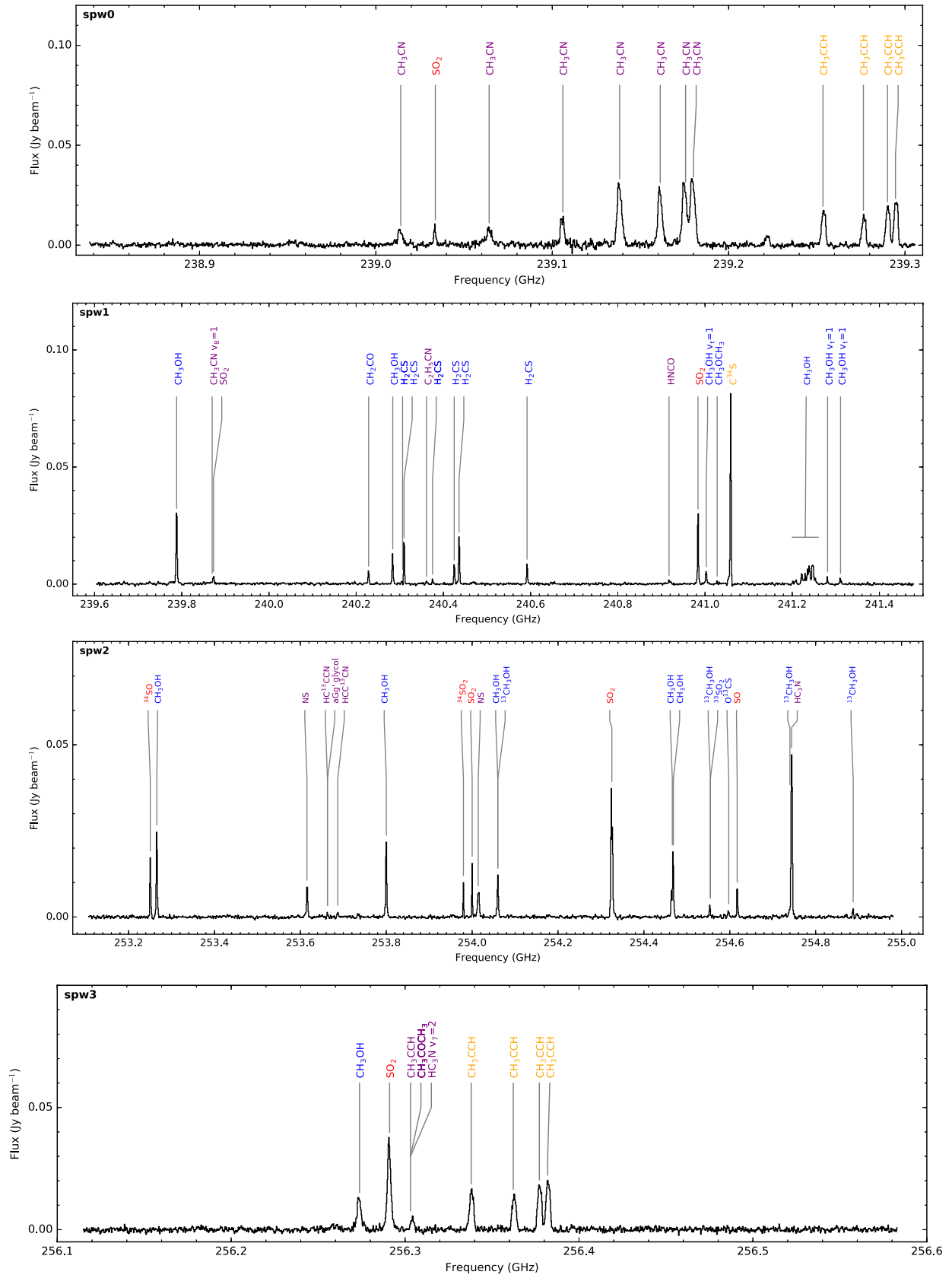
Figure A.3. Spectrum of the four spectral windows toward mm2. The different line label colors denote different types of line morphology toward mm1: purple is disk-tracing, blue is blue-dominant, red is red-dominant, and orange is outflow-tracing.

REFERENCES

Ahmadi, A., Beuther, H., Mottram, J. C., et al. 2018, A&A, 618, A46

Allen, V., van der Tak, F. F. S., Sánchez-Monge, Á., Cesaroni, R., & Beltrán, M. T. 2017, A&A, 603, A133

Andrews, S. M., Huang, J., Pérez, L. M., et al. 2018, ApJL, 869, L41

Ansdell, M., Williams, J. P., van der Marel, N., et al. 2016, ApJ, 828, 46

Ansdell, M., Williams, J. P., Trapman, L., et al. 2018, ApJ, 859, 21

Arce, H. G., Shepherd, D., Gueth, F., et al. 2007, in Protostars and Planets V, ed. B. Reipurth, D. Jewitt, & K. Keil, 245

Aso, Y., Ohashi, N., Saigo, K., et al. 2015, ApJ, 812, 27

Astropy Collaboration, Robitaille, T. P., Tollerud, E. J., et al. 2013, A&A, 558, A33

Astropy Collaboration, Price-Whelan, A. M., Sipőcz, B. M., et al. 2018, AJ, 156, 123

Bailer-Jones, C. A. L., Rybizki, J., Fouesneau, M., Mantelet, G., & Andrae, R. 2018, AJ, 156, 58

Bate, M. R. 2018, MNRAS, 475, 5618

Beckwith, S., Zuckerman, B., Skrutskie, M. F., & Dyck, H. M. 1984, ApJ, 287, 793

Beltrán, M. T., Brand, J., Cesaroni, R., et al. 2006, A&A, 447, 221

Beltrán, M. T., & de Wit, W. J. 2016, A&A Rv, 24, 6

Beltrán, M. T., Sánchez-Monge, Á., Cesaroni, R., et al. 2014, A&A, 571, A52

Beltrán, M. T., Cesaroni, R., Rivilla, V. M., et al. 2018, A&A, 615, A141

Beltrán, M. T., Padovani, M., Girart, J. M., et al. 2019, A&A, 630, A54

Beuther, H., Linz, H., Henning, T., Feng, S., & Teague, R. 2017, A&A, 605, A61

Beuther, H., Ahmadi, A., Mottram, J. C., et al. 2019, A&A, 621, A122

Blake, G. A., Sutton, E. C., Masson, C. R., & Phillips, T. G. 1987, ApJ, 315, 621

Bøgelund, E. G., Barr, A. G., Taquet, V., et al. 2019, A&A, 628, A2

Boley, P. A., Linz, H., van Boekel, R., et al. 2012, A&A, 547, A88

—. 2013, A&A, 557, C1

Bonnell, I. A., Bate, M. R., & Vine, S. G. 2003, MNRAS, 343, 413

Busquet, G., Girart, J. M., Estalella, R., et al. 2019, A&A, 623, L8

Caswell, J. L. 1998, MNRAS, 297, 215

Caswell, J. L., Kesteven, M. J., Stewart, R. T., Milne, D. K., & Haynes, R. F. 1992, ApJL, 399, L151

Cesaroni, R., Neri, R., Olmi, L., et al. 2005, A&A, 434, 1039

Cesaroni, R., Sánchez-Monge, Á., Beltrán, M. T., et al. 2017, A&A, 602, A59

Choi, M., Tatematsu, K., & Kang, M. 2010, ApJL, 723, L34

Codella, C., Cabrit, S., Gueth, F., et al. 2014, A&A, 568, L5

Collings, M. P., Anderson, M. A., Chen, R., et al. 2004, MNRAS, 354, 1133

Csengeri, T., Bontemps, S., Wyrowski, F., et al. 2018, A&A, 617, A89

Cummins, S. E., Linke, R. A., & Thaddeus, P. 1986, ApJS, 60, 819

Davies, B., Hoare, M. G., Lumsden, S. L., et al. 2011, MNRAS, 416, 972

De Buizer, J. M. 2006, ApJL, 642, L57

De Buizer, J. M., Redman, R. O., Longmore, S. N., Caswell, J., & Feldman, P. A. 2009, A&A, 493, 127

de Wit, W. J., Hoare, M. G., Oudmaijer, R. D., & Lumsden, S. L. 2010, A&A, 515, A45

de Wit, W. J., Testi, L., Palla, F., & Zinnecker, H. 2005, A&A, 437, 247

Draine, B. T. 2003a, ARA&A, 41, 241

—. 2003b, ApJ, 598, 1017

—. 2011, Physics of the Interstellar and Intergalactic Medium (Princeton University Press, 2011. ISBN: 978-0-691-12214-4)

Dutrey, A., Semenov, D., Chapillon, E., et al. 2014, Protostars and Planets VI, University of Arizona Press, Tucson, 317

Eisner, J. A., Arce, H. G., Ballering, N. P., et al. 2018, ApJ, 860, 77

Ellingsen, S. P., Shabala, S. S., & Kurtz, S. E. 2005, MNRAS, 357, 1003

Enoch, M. L., Corder, S., Duchêne, G., et al. 2011, ApJS, 195, 21

Fayolle, E. C., Öberg, K. I., Garrod, R. T., van Dishoeck, E. F., & Bisschop, S. E. 2015, A&A, 576, A45

Feng, S., Beuther, H., Henning, T., et al. 2015, A&A, 581, A71

Garrod, R. T., Widicus Weaver, S. L., & Herbst, E. 2008, ApJ, 682, 283

Gerner, T., Beuther, H., Semenov, D., et al. 2014, A&A, 563, A97

Ginsburg, A., Bally, J., Goddi, C., Plambeck, R., & Wright, M. 2018, ApJ, 860, 119

Ginsburg, A., McGuire, B., Plambeck, R., et al. 2019, ApJ, 872, 54

Ginsburg, A., Robitaille, T., Koch, E., et al. 2016, spectral-cube: v0.4.0 release, v0.4.0, Zenodo, doi:10.5281/zenodo.61671. https://doi.org/10.5281/zenodo.61671

Ginsburg, A., Goddi, C., Kruijssen, J. M. D., et al. 2017, ApJ, 842, 92

Girart, J. M., Estalella, R., Fernández-López, M., et al. 2017, ApJ, 847, 58

Girart, J. M., Fernández-López, M., Li, Z.-Y., et al. 2018, ApJL, 856, L27

Green, J. A., & McClure-Griffiths, N. M. 2011, MNRAS, 417, 2500

Guzmán, A. E., Guzmán, V. V., Garay, G., Bronfman, L., & Hechenleitner, F. 2018, The Astrophysical Journal Supplement Series, 236, 45

Guzmán, A. E., Garay, G., Rodríguez, L. F., et al. 2014, ApJ, 796, 117

Harsono, D., Jørgensen, J. K., van Dishoeck, E. F., et al. 2014, A&A, 562, A77

Henning, T., & Semenov, D. 2013, Chemical Reviews, 113, 9016

Herbst, E., & van Dishoeck, E. F. 2009, ARA&A, 47, 427

Ho, P. T. P., Barrett, A. H., Myers, P. C., et al. 1979, ApJ, 234, 912

Hunter, J. D. 2007, Computing in science & engineering, 9, 90

Hunter, T. R., Brogan, C. L., Cyganowski, C. J., & Young, K. H. 2014, ApJ, 788, 187

Ilee, J. D., Cyganowski, C. J., Brogan, C. L., et al. 2018, ApJL, 869, L24

Ilee, J. D., Cyganowski, C. J., Nazari, P., et al. 2016, MNRAS, 462, 4386

Ilee, J. D., Wheelwright, H. E., Oudmaijer, R. D., et al. 2013, MNRAS, 429, 2960

Isokoski, K., Bottinelli, S., & van Dishoeck, E. F. 2013, A&A, 554, A100

Izquierdo, A. F., Galván-Madrid, R., Maud, L. T., et al. 2018, MNRAS, 478, 2505

Jaber Al-Edhari, A., Ceccarelli, C., Kahane, C., et al. 2017, A&A, 597, A40

Jiménez-Serra, I., Zhang, Q., Viti, S., Martín-Pintado, J., & de Wit, W.-J. 2012, ApJ, 753, 34

Johnston, K. G., Beuther, H., Linz, H., et al. 2014, Astrophysics and Space Science Proceedings, 36, 413

Johnston, K. G., Robitaille, T. P., Beuther, H., et al. 2015, ApJL, 813, L19

Jørgensen, J. K., van Dishoeck, E. F., Visser, R., et al. 2009, A&A, 507, 861

Jørgensen, J. K., van der Wiel, M. H. D., Coutens, A., et al. 2016, A&A, 595, A117

Joye, W. A., & Mandel, E. 2003, in Astronomical Society of the Pacific Conference Series, Vol. 295, Astronomical Data Analysis Software and Systems XII, ed. H. E. Payne, R. I. Jedrzejewski, & R. N. Hook, 489

Kahn, F. D. 1974, A&A, 37, 149

Keto, E., Zhang, Q., & Kurtz, S. 2008, ApJ, 672, 423

Koumpia, E., Ababakr, K. M., de Wit, W. J., et al. 2019, A&A, 623, L5

Kraus, S., Hofmann, K.-H., Menten, K. M., et al. 2010, Nature, 466, 339

Kraus, S., Kluska, J., Kreplin, A., et al. 2017, ApJL, 835, L5

Krumholz, M. R., & Bonnell, I. A. 2009, Models for the formation of massive stars, ed. G. Chabrier (Cambridge University Press), 288

Kuiper, R., & Hosokawa, T. 2018, A&A, 616, A101

Kuiper, R., Klahr, H., Beuther, H., & Henning, T. 2010, ApJ, 722, 1556

Kuiper, R., Turner, N. J., & Yorke, H. W. 2016, ApJ, 832, 40

Kuiper, R., Yorke, H. W., & Turner, N. J. 2015, ApJ, 800, 86

Kurtz, S., Cesaroni, R., Churchwell, E., Hofner, P., & Walmsley, C. M. 2000, Protostars and Planets IV, University of Arizona Press, Tucson, 299

Lada, C. J., & Lada, E. A. 2003, ARA&A, 41, 57

Larson, R. B., & Starrfield, S. 1971, A&A, 13, 190

Lee, C.-F., Hwang, H.-C., & Li, Z.-Y. 2016, ApJ, 826, 213

Lee, C.-F., Li, Z.-Y., Ho, P. T. P., et al. 2017, Science Advances, 3, e1602935

Looney, L. W., Mundy, L. G., & Welch, W. J. 2003, ApJ, 592, 255

Maret, S., Faure, A., Scifoni, E., & Wiesenfeld, L. 2009, MNRAS, 399, 425

Maud, L. T., Hoare, M. G., Galván-Madrid, R., et al. 2017, MNRAS, 467, L120

Maud, L. T., Cesaroni, R., Kumar, M. S. N., et al. 2018, A&A, 620, A31

—. 2019, A&A, 627, L6

McCaughrean, M. J., & O'Dell, C. R. 1996, AJ, 111, 1977

McKee, C. F., & Tan, J. C. 2003, ApJ, 585, 850

McMillan, J. P., Fortman, S. M., Neese, C. F., & De Lucia, F. C. 2016, ApJ, 823, 1

McMullin, J. P., Waters, B., Schiebel, D., Young, W., & Golap, K. 2007, in Astronomical Society of the Pacific Conference Series, Vol. 376, Astronomical Data Analysis Software and Systems XVI, ed. R. A. Shaw, F. Hill, & D. J. Bell, 127

Mezger, P. G., & Henderson, A. P. 1967, ApJ, 147, 471

Müller, H. S. P., Schlöder, F., Stutzki, J., & Winnewisser, G. 2005, Journal of Molecular Structure, 742, 215

Murillo, N. M., Lai, S.-P., Bruderer, S., Harsono, D., & van Dishoeck, E. F. 2013, A&A, 560, A103

Murillo, N. M., van Dishoeck, E. F., van der Wiel, M. H. D., et al. 2018, A&A, 617, A120

Nakano, T. 1989, ApJ, 345, 464

Öberg, K. I., Boamah, M. D., Fayolle, E. C., et al. 2013, ApJ, 771, 95

Ossenkopf, V., & Henning, T. 1994, A&A, 291, 943

Oya, Y., Sakai, N., López-Sepulcre, A., et al. 2016, ApJ, 824, 88

Patel, N. A., Curiel, S., Sridharan, T. K., et al. 2005, Nature, 437, 109

Perez, F., & Granger, B. E. 2007, Computing in Science Engineering, 9, 21

Phillips, C. J., Norris, R. P., Ellingsen, S. P., & McCulloch, P. M. 1998, MNRAS, 300, 1131

Pickett, H. M., Poynter, R. L., Cohen, E. A., et al. 1998, JQSRT, 60, 883

Plambeck, R. L., & Wright, M. C. H. 2016, ApJ, 833, 219

Quénard, D., Jiménez-Serra, I., Viti, S., Holdship, J., & Coutens, A. 2018, MNRAS, 474, 2796

Robitaille, T., & Bressert, E. 2012, APLpy: Astronomical Plotting Library in Python, v1.1.1, ASCL, ascl:1208.017

Robitaille, T. P. 2011, A&A, 536, A79. http://dx.doi.org/10.1051/0004-6361/201117150

Rosolowsky, E. W., Pineda, J. E., Foster, J. B., et al. 2008, ApJS, 175, 509

Sakai, N., Oya, Y., Sakai, T., et al. 2014, ApJL, 791, L38

Sakai, N., Oya, Y., Higuchi, A. E., et al. 2017, MNRAS, 467, L76

Sana, H., Le Bouquin, J. B., Lacour, S., et al. 2014, ApJS, 215, 15

Sánchez-Monge, Á., Beltrán, M. T., Cesaroni, R., et al. 2014, A&A, 569, A11

Sanna, A., Kölligan, A., Moscadelli, L., et al. 2019, A&A, 623, A77

Sargent, A. I., & Beckwith, S. 1987, ApJ, 323, 294

Segura-Cox, D. M., Harris, R. J., Tobin, J. J., et al. 2016, ApJL, 817, L14

Shabala, S. S., Ellingsen, S. P., Kurtz, S. E., & Forbes, L. K. 2006, MNRAS, 372, 457

Silva, A., Zhang, Q., Sanhueza, P., et al. 2017, ApJ, 847, 87

Smith, C. H., Wright, C. M., Aitken, D. K., Roche, P. F., & Hough, J. H. 2000, MNRAS, 312, 327

Sutton, E. C., Blake, G. A., Masson, C. R., & Phillips, T. G. 1985, ApJS, 58, 341

Suzuki, T., Ohishi, M., Saito, M., et al. 2018, ApJS, 237, 3

Swift, J. J., Welch, W. J., & Di Francesco, J. 2005, ApJ, 620, 823

Tanaka, K. E. I., Tan, J. C., & Zhang, Y. 2017, ApJ, 835, 32

Tobin, J. J., Hartmann, L., Chiang, H.-F., et al. 2012, Nature, 492, 83

Tobin, J. J., Looney, L. W., Wilner, D. J., et al. 2015, ApJ, 805, 125

Tobin, J. J., Megeath, S. T., van't Hoff, M., et al. 2019, ApJ, 886, 6

Tripathi, A., Andrews, S. M., Birnstiel, T., & Wilner, D. J. 2017, ApJ, 845, 44

Urquhart, J. S., Thompson, M. A., Moore, T. J. T., et al. 2013, MNRAS, 435, 400

Urquhart, J. S., Csengeri, T., Wyrowski, F., et al. 2014, A&A, 568, A41

Urquhart, J. S., Figura, C. C., Moore, T. J. T., et al. 2015, MNRAS, 452, 4029

van der Tak, F. F. S., van Dishoeck, E. F., & Caselli, P. 2000, A&A, 361, 327

Walmsley, C. M., & Ungerechts, H. 1983, A&A, 122, 164

Walsh, A. J., Purcell, C. R., Longmore, S. N., et al. 2014, MNRAS, 442, 2240

Wang, K.-S., van der Tak, F. F. S., & Hogerheijde, M. R. 2012, A&A, 543, A22

Williams, J. P., & Cieza, L. A. 2011, ARA&A, 49, 67

Yen, H.-W., Takakuwa, S., Koch, P. M., et al. 2015, ApJ, 812, 129

Zapata, L. A., Garay, G., Palau, A., et al. 2019, ApJ, 872, 176

Zhang, Y., Tan, J. C., Tanaka, K. E. I., et al. 2019a, Nature Astronomy, 3, 517

Zhang, Y., Tan, J. C., Sakai, N., et al. 2019b, ApJ, 873, 73